

**24 GHz Wearable Antenna
Design for Wireless Body Area
Networks: An Investigation of
On-Body Channel
Characterisation and Zigbee
Protocol at 24 GHz**

Mubasher Ali

School of Engineering
University of Kent

Thursday 10th August, 2023

Abstract

User-centric networks drive the evolution of wireless communication, demanding constant connectivity and services across various domains. MM-wave (24 GHz ISM band) frequencies emerge as a promising solution for WBAN, overcoming challenges posed by the on-body radio channel and achieving reliable communication in diverse environments. This thesis uses multiple antennas to characterise the mm-wave (24 GHz) radio propagation channel for body-centric communication. The aim is to design compact antennas insensitive to human skin and structural deformation, exploring system-level modelling of Zigbee's PHY and MAC layers in the context of mm-wave (24 GHz) Body Area Networks (BAN).

The first part introduces innovative on-body antenna designs, incorporating split square-ring electromagnetic bandgap (EBG) structures and bow-tie slot antennas, demonstrating high insensitivity to body proximity and bending. The study also proposes Koch fractal antennas backed by EBG structures for improved performance and stable radiation patterns suitable for on-skin mounting. The second part analyses 24 GHz on-body communication system performance and path loss modelling, considering various antenna types. Measurement campaigns confirm the significance of antenna diversity and position in mm-wave propagation on the human body, predicting potential performance for 24 GHz ISM band WBAN systems. The third part evaluates Zigbee protocol performance in body-centric wireless communication within the 24 GHz channel model. Results show good radio link quality for physiological sensor nodes, with lower performance observed in NLOS and PLOS scenarios due to body tissue obstruction. Throughput performance highlights the importance of sensor positioning and MAC layer optimisation.

This thesis advances 24 GHz ISM band WBANs through innovative antennas, introducing 24 GHz path loss modeling, and insights into Zigbee (physical layer and MAC) protocol. It drives future research in advanced designs, propagation modelling, and protocol enhancements, boosting on-body wireless communication capabilities.

Acknowledgements

I would like to express my deepest gratitude to my supervisors, Professor John Batchelor and Professor Nathan Gomes, for their unwavering support, vision, and invaluable guidance throughout my doctoral journey. Their patience, encouragement, and advice were instrumental in helping me successfully complete my thesis and grow as a junior member of academia. They have been remarkable role models, and I am truly grateful for their mentorship.

In concluding this doctoral journey, I extend heartfelt gratitude to my beloved mother, siblings—especially my elder sister Mehreen Fatima and sister Umbreen Fatima—and brother Dr. Nauman Ahmad. Special appreciation goes to my lovely wife, Quratulain, for her unwavering support and love. I am also grateful to friends who have been an integral part of this journey. Their encouragement and belief in my abilities have provided a constant source of strength and motivation. I am truly fortunate to have had such an incredible support system throughout this challenging and rewarding PhD experience. Their presence, particularly that of Mehreen Fatima and Dr Nauman Ahmad, has made every step of this academic endeavour more meaningful and fulfilling.

Furthermore, I extend my thanks to the Engineering and Physical Sciences Research Council for providing me with the opportunity and funding to pursue my Ph.D. degree. Their support has been instrumental in enabling me to conduct this research and achieve my academic goals.

Mubasher Ali, August 2023.

Contents

Abstract	i
Acknowledgements	ii
List of Figures	4
List of Tables	9
List of Acronyms	10
1 Introduction	12
1.1 Research Motivation	15
1.2 Research Aims and Objectives	16
1.3 Overview of Thesis	17
2 Background and Literature Review	22
2.1 Introduction	22
2.2 Fundamental Concepts and Principles	23
2.2.1 Microstrip Antennas	23
2.2.2 S parameters / Two-port network	24
2.2.3 Propagation Loss	26
2.3 Wearable Antenna design	27
2.3.1 Wearable antennas	27
2.4 Radio channel characterisation for WBANs	30
2.4.1 Measurements of communication channels and empirical mod- elling	32
2.4.1.1 Narrowband channel characterisation	33
2.4.1.2 UWB channel characterisation	33
2.4.1.3 60 GHz mm-wave channel characterisation	34
2.5 Millimeter wave communication and a MAC layer perspective	35
2.5.1 Medium Access Control (MAC):	36
2.5.2 Literature related to WBANs MAC	38
2.5.3 Taxonomy of MAC protocols	41

2.5.4	Evaluation and Comparison of Medium Access Scheduling Schemes	42
3	24 GHz Flexible antennas for On-body communication	59
3.1	introduction	59
3.2	EBG backed bow-tie antenna	61
3.2.1	Antenna Design and Integration with EBG	62
3.2.2	Free Space performance Evaluation	64
3.2.3	Structural bending analysis	65
3.2.4	SAR and body loading effects	68
3.3	Circular Patch antenna with radial stub	71
3.3.1	Return Loss evaluation	71
3.3.2	Structural bending	73
3.3.3	Radiation Pattern	73
3.3.4	On-body Performance evaluation	76
3.4	Planner Quasi-Yagi antenna array	76
3.4.1	Structure Design / Geometry	78
3.4.2	Performance analysis	79
3.4.3	On-body performance	80
3.4.4	Effect of bending	81
3.4.5	Radiation pattern	82
3.5	Microstrip-based Vivaldi antenna	83
3.5.1	On-body performance	84
3.5.2	Effect of bending	86
3.6	Conclusion	88
4	EBG backed Fractal geometry-based antenna for 24 GHz ISM band WBAN	93
4.1	Introduction	93
4.2	Electromagnetic band gap structure	95
4.3	First Iteration Koch Fractal based Antenna Design and Integration with EBG Surface	98
4.3.1	Results and Discussions	100
4.3.1.1	Reflection Coefficient Evaluation	100
4.3.1.2	Far-Field Radiation Properties	101
4.3.1.3	On-body Performance	103
4.3.1.4	Structural Conformability	105
4.3.1.5	Specific Absorption Rate Evaluation	106
4.4	2nd Iteration Koch Fractal based Antenna Design and Integration with EBG Surface	108
4.4.1	Results and Discussions	111
4.4.1.1	Reflection Coefficient Evaluation	111
4.4.1.2	Far-Field Radiation Properties	112
4.4.1.3	On-body Performance	113
4.4.1.4	Structural Conformability	114

4.4.1.5	Specific Absorption Rate Evaluation	116
4.5	Conclusion	118
5	Empirical propagation path loss model for on-body communication at 24 GHz ISM band	124
5.1	Introduction	124
5.2	Experimental Characterisation	128
5.2.1	Frequency Domain Measurement Configuration	128
5.2.2	Antennas	131
5.3	Path Loss Model and Data Analysis	133
5.3.1	Case 1	134
5.3.2	Case 2	139
5.3.3	Case 3	142
5.3.4	Case 4	146
5.4	Conclusion	151
6	A Case Study of CSMA (ZigBee) for WBANs at 24 GHz	157
6.1	Introduction	157
6.2	Topology and architecture of mm-Waves WBAN	160
6.3	Simulation of Zigbee (Physical layer) at 24 GHz: Sink with one sensor node	164
6.4	Simulation of Zigbee at 24 GHz: Sink with multiple sensor nodes	168
6.4.1	Configuration of NetSim simulator to depict the actual environment	169
6.4.2	Network simulation under case 2 environment	172
6.4.3	Network simulation under case 4 environment	176
6.5	Conclusion	179
7	Conclusion and Future work	185
7.1	Future work	189

List of Figures

1.1	Typical WBAN network	13
2.1	The basic structure of the microstrip patch antenna	23
2.2	Four common feeding methods of microstrip patch antenna	24
2.3	Illustration Involving a two-port network and S-parameters	25
2.4	MAC Super-frame structures of; a) IEEE 802.15.4, b) IEEE 802.15.6 and c) IEEE 802.15.3c	40
2.5	Classifies MAC Super-frame structures into IEEE 802.15.3c, IEEE 802.15.4 and IEEE 802.15.6	41
2.6	Taxonomy of MAC protocols in terms of directional and non-directional antenna-based architectures for WBANs and WPANs	43
3.1	EBG geometry	61
3.2	Phase reflection diagram	62
3.3	Bow-tie slot antenna geometry	62
3.4	Integration of EBG with antenna	63
3.5	Return loss of simulated EBG backed antenna (Fig. 3.4) with and without connector and measured S_{11}	64
3.6	Radiation polar plots of bow-tie slot antenna (Fig.3.4) with EBG/AMC measured (bold solid-line), with EBG/AMC simulated (green dash- line) and without EBG/AMC measured (dash-line) at 24 GHz . . .	65
3.7	Measured radiation polar plots of bow-tie slot antenna (Fig.3.4) with EBG/AMC (bold solid-line) and without EBG/AMC (dash- line) at 24.250 GHz	65
3.8	Measured reflection coefficients of the antenna (Fig.3.4) when bent along the X and Y-axis.	66
3.9	Measured radiation polar plots of EBG backed antenna (Fig.3.4) when bent on 15 mm radius cylinder along X-axis (black solid line), Y-axis (blue solid-line) and without bent (dash-line) at 24 GHz. . .	67
3.10	Measured radiation polar plots of EBG backed antenna (Fig.3.4) when bent on 15 mm radius cylinder along X-axis (black solid line), Y-axis (blue solid-line) and without bent (dash-line) at 24.250 GHz. . .	67
3.11	Measured reflection coefficients of the antenna (Fig.3.4) on the hu- man body without EBG.	69
3.12	Measured reflection coefficients of the antenna (Fig.3.4) on human body with EBG.	69

3.13	SAR distribution of prototype antenna (Fig.3.4) with EBG and without EBG	70
3.14	Geometry of the circular patch antenna	72
3.15	a) Prototype of the circular patch antenna. b) Measured reflection coefficients of the antenna.	73
3.16	a) Antenna bent onto the cylinder along the X and Y axis. b) Measured reflection coefficients of the antenna while bending along the X and Y axis on the 14mm cylinder.	74
3.17	Measured radiation patterns of the antenna with and without a bend in free space and on-body. (a) xz plane and (b) yz plane at 24 GHz.	75
3.18	Gain vs Frequency plot of the circular patch antenna Fig.3.14	76
3.19	a) Antenna Placement on the body and b) Measured reflection coefficients of the antenna on the human body.	77
3.20	Planar Yagi Uda antenna geometry and dimensions	78
3.21	a) Planar Yagi Uda Antenna Prototype. b) Free space Yagi Uda antenna S_{11} performance.	79
3.22	Return loss performance of Yagi Uda antenna when placed in different positions on the human body	80
3.23	a) Planar Yagi Uda Antenna bent along a 14 mm radial cylinder. b) Reflection coefficients of Yagi Uda antenna when bending along a 14 mm radial cylinder.	81
3.24	measured E-Plane radiation patterns of Yagi Uda antenna	82
3.25	measured H-Plane radiation patterns of Yagi Uda antenna	83
3.26	Geometry and dimensions of Vivaldi antenna	84
3.27	a) Vivaldi Antenna Prototype. b) Free space Vivaldi antenna S_{11} performance.	85
3.28	measured E-Plane radiation patterns of Vivaldi antenna	85
3.29	measured H-Plane radiation patterns of Vivaldi antenna	86
3.30	On-body return loss performance of Vivaldi antenna	86
3.31	a) Vivaldi Antenna bent along a 14 mm radial cylinder. b) Reflection coefficients of Vivaldi antenna when bending along a 14 mm radial cylinder.	87
4.1	Proposed EBG geometry	96
4.2	Phase reflection diagram	96
4.3	Dispersion diagram	97
4.4	EBG suspended transmission line S parameters	98
4.5	Koch fractal based Bow-tie slot antenna geometry, $a = 0.72$, $b = 0.67$ and $c = 0.75$ mm	99
4.6	Integration of EBG with antenna	100
4.7	S_{11} of EBG backed antenna shown in Fig. 4.6.	101
4.8	Measured and simulated E Plane radiation polar plots of EBG backed antenna shown in Fig. 4.6.	102

4.9	Measured and simulated H Plane radiation polar plots of EBG backed antenna shown in Fig. 4.6.	102
4.10	Measured reflection coefficients of the antenna on the human body without EBG shown in Fig. 4.5.	103
4.11	Measured reflection coefficients of the antenna on the human body with EBG shown in Fig. 4.6.	104
4.12	Reflection Coefficient of the EBG-backed antenna (Fig. 4.6.) when bent on 14 mm radial cylinder along "Y" and "X" axis.	105
4.13	Measured radiation polar plots of EBG backed antenna (Fig. 4.6) when bent on 14 mm radius cylinder along X-axis (Red dash-line), Y-axis (orange dash-line) and without bending (solid-line) at 24 GHz	107
4.14	SAR distribution of prototype antenna (a) without EBG (b) with EBG (c) placement setting of tissues. Note, different scales are used in (a) and (b) owing to large variations in peak values.	108
4.15	2nd Iteration Koch fractal based Bow-tie slot antenna geometry	109
4.16	Integration of EBG with antenna	110
4.17	S_{11} of EBG backed antenna shown Fig.4.16	112
4.18	Measured and simulated E Plane radiation polar plots of EBG backed antenna shown Fig.4.16	113
4.19	Measured and simulated H Plane radiation polar plots of EBG backed antenna shown Fig.4.16	114
4.20	Measured reflection coefficients of the antenna (Fig.4.15) on the human body without EBG	115
4.21	Measured reflection coefficients of the antenna (Fig.4.16) on the human body with EBG	115
4.22	Reflection Coefficient of the EBG-backed antenna when bent on 14 mm radial cylinder along "Y" and "X" axis.	116
4.23	Measured radiation polar plots of EBG backed antenna (Fig.4.16) when bent on 14 mm radius cylinder along X-axis (Red dash-line), Y-axis (orange dash-line) and without bending (solid-line) at 24 GHz	117
4.24	SAR distribution of prototype antenna (Fig.4.15)(a) without EBG (b) with EBG (c) placement setting of tissues. Note, different scales are used in (a) and (b) owing to large variations in peak values.	118
5.1	(a) Dimension of the body used in propagation measurements, (b) Locations of transmitter and receiver antennas for on-body channel characterisation campaign	127
5.2	Measurement setup including post-processing steps.	128
5.3	E-plane Radiation Pattern of antennas	129
5.4	H-Plane Radiation Pattern of antennas	130
5.5	Measurement setup on a human subject in case 1 with front and side view	135
5.6	Linear regression on measured path loss data (case 1) at 3 frequencies sector-wise data covering complete band	136
5.7	Linear regression on measured path loss data (case 1) at a 24 GHz on each sector	137

5.8	The cumulative distribution function of the shadowing factor for measured data (case 1)	138
5.9	Measurement setup on a human subject in case 2 with front and side view	139
5.10	Linear regression on measured path loss data (case 2) at 3 frequencies sector-wise data covering complete band	140
5.11	Linear regression on measured path loss data (case 2) at a 24 GHz on each sector	141
5.12	The cumulative distribution function of the shadowing factor for measured data (case 2)	142
5.13	Measurement setup on a human subject in case 3 with front and side view	143
5.14	Linear regression on measured path loss data (case 3) at 3 frequencies sector-wise data covering complete band	144
5.15	Linear regression on measured path loss data (case 3) at a 24 GHz on each sector	145
5.16	The cumulative distribution function of the shadowing factor for measured data (case 3)	146
5.17	Measurement setup on a human subject in case 4 with front and side view	147
5.18	Linear regression on measured path loss data (case 4) at 3 frequencies sector-wise data covering complete band	148
5.19	Linear regression on measured path loss data (case 4) at a 24 GHz on each sector	149
5.20	The cumulative distribution function of the shadowing factor for measured data (case 4)	150
6.1	Typical Star topology-based WBAN network	160
6.2	Simulated Received signal strength against distance (a) Case 2 (section 5.3.2) (b) Case 4 (section 5.3.4) using 24 GHz channel model	164
6.3	BER variations with the distance with reference to case 2 (section 5.3.2 explains all three sectors)	166
6.4	BER variations with the distance with reference to case 4 (section 5.3.4 explains all three sectors)	168
6.5	Sink and sensor nodes' actual location on the chest to torso link	169
6.6	Sink and sensor nodes location on the chest to torso link in the case 2 environment: Left one is actual locations and right one is simulations locations which are different	170
6.7	Sink and sensor nodes location on the chest to torso link in the case 4 environment: Left one is actual locations and right one is simulations locations which are different	171
6.8	Normalized throughput against the normalized offered load in case 2 environment of sector 1	174
6.9	Normalized throughput against the normalized offered load in case 2 environment of sector 2	174

6.10	Normalized throughput against the normalized offered load in case 2 environment of sector 3	175
6.11	Normalized throughput against the normalized offered load in case 4 environment of sector 1	177
6.12	Normalized throughput against the normalized offered load in case 4 environment of sector 2	177
6.13	Normalized throughput against the normalized offered load in case 4 environment of sector 3	178

List of Tables

2.1	Pros and cons for different types of antennas when integrated into textile substrates	30
2.2	Comparison of different features of WSN standards 802.15.4, 802.15.6, and 802.15.3c	42
2.3	Comparison between TDMA, CSMA/CA and FDMA	44
3.1	Comparison with previously published K band EBG antennas	70
4.1	Material properties of skin, fat, muscle tissues at 24 GHz	108
4.2	Comparison of proposed antenna (Fig. 4.15) with previously reported K-band EBG antennas	119
5.1	Free space path loss and Atmospheric absorption at 24 GHz Vapor density = $8g/m^3$, Air pressure = $102 \times 10^5 Kpa$, Temperature = $23^\circ C$	126
5.2	Transmit Receive antennas configuration for channel measurements	133
5.3	Path loss exponent and deviation values in case 1	138
5.4	Path loss exponent and deviation values in case 2	142
5.5	Path loss exponent and deviation values in case 3	146
5.6	Path loss exponent and deviation values in case 4	150
6.1	STANDARD SENSORS USED IN A TYPICAL WIRELESS BODY AREA NETWORK [17]	161
6.2	Trends of simulated and measured data in case 2 measured in the previous chapter	165
6.3	Trends of simulated and measured data in case 4 measured in the previous chapter	167
6.4	Trends of simulated and measured RSSI data between the sensor nodes after adjustments of locations	172
7.1	WBAN comparison at different frequencies	188

List of Acronyms

WBAN	Wireless body area network
SNR	Signal-to-noise ratio
EBG	Electromagnetic band gap
SAR	Specific absorption rate
MAC	Medium access control
CSMA	Carrier-sense multiple access
(UWB	Ultra-wideband
FSPL	Free-Space Path Loss
ECG	Electrocardiogram
RSSI	Received signal strength indicator
ISM	Industrial, Scientific, and Medical frequency bands
LOS	Line-of-sight
NLOS	Non-line-of-sight
PEC	Perfect electric conductor
FDMA	Frequency-division multiple access
TDMA	Time Division Multiple Access
BMS	Biomedical sensor
CAP	Contention Access Period
CFP	Contention Free Period
PBC	Periodic boundary conditions
AMC	Artificial magnetic conductor
CPW	Co-planar waveguide
VNA	Vector Network Analyzer

BCWN	Body-centric wireless network
FDTD	Finite-difference time-domain
CDF	Cumulative distribution function
PHY	Physical layer
BER	Bit Error Rate

Chapter 1

Introduction

The evolution of wireless communication is being driven by user-centric networks that require constant and reliable connectivity and services across a range of domains. One such network is the wireless body area network (WBAN), which significantly differs from conventional wireless systems due to its utilisation of the on-body radio channel for communication. Wireless body area networks (WBANs) refers to networking over the body and body-to-body with the use of wearable and implantable wireless sensor nodes [1]. Wireless body area networks (WBANs) has got numerous applications in everyday life including healthcare, entertainment, space exploration, military, and so forth [2].

Body-centric wireless networks are generally partitioned into three domains, off-body, on-body, and in-body communication. Fig.1.1 presents the typical diagram of the operational framework of the wireless body area network. WBANs are mainly categorised into 3 tiers, Tier 1 is the intra-BAN network in which sensors are placed on the body to monitor the physiological data of the patients and forward the monitored data to the coordinator node. Tier 2 is the inter-BAN network in which the coordinator node transmits the data to the off-body access point. Tier 3 is the beyond-BAN network, in which off-body access points forward these physiological data to healthcare professionals through dedicated internet communication links [3]. Each type of physiological data of the patient is entirely different from other categories of physiological data. So, each body sensor data

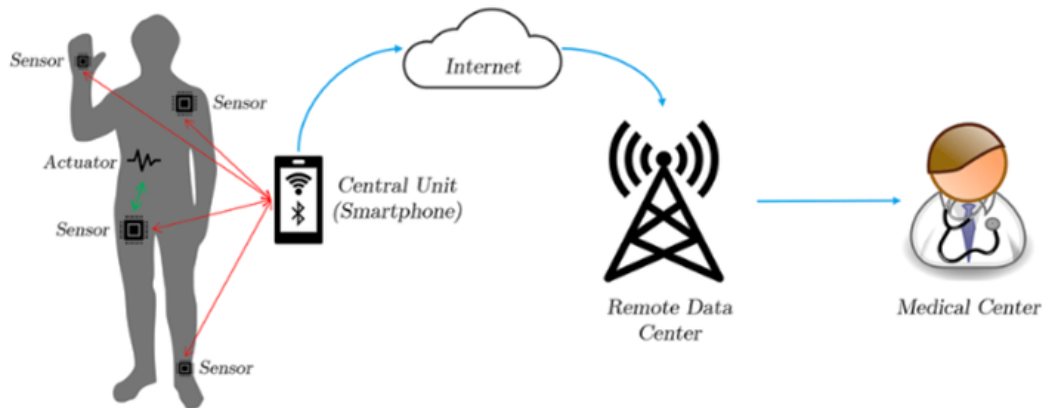


FIGURE 1.1: Typical WBAN network

requires different processing methods by the medical team. Therefore, body sensor data is considered heterogeneous [4].

However, the human body presents challenges for radio propagation, necessitating a thorough understanding of its impact on antenna elements, radio propagation channel parameters, and overall system performance. WBAN devices must also possess characteristics such as low power consumption, compactness, and the ability to maintain high data rates and robust performance in challenging environments, even at low signal-to-noise ratios (SNR). In this context, the mm-wave (24 GHz ISM band) frequencies emerge as a highly promising solution for meeting the unique requirements of WBAN.

Wireless body area networks (WBANs) using mm-wave (24 GHz) technology are relatively new, but they hold considerable potential for enhancing healthcare and various other applications. In the latter half of the 20th century, numerous communication and sensing applications began to draw attention to the usage of millimeter-wave frequencies, especially those in the 24 GHz range. In the context of body-centric applications, researchers started looking at the potential of mm-wave frequencies for short-range communication systems. In the early 2000s, mm-wave WBAN research and development picked up momentum. Researchers from academic institutions and businesses started looking into the viability, difficulties, and potential uses of employing mm-wave frequencies for WBANs. The

Institute of Electrical and Electronics Engineers (IEEE), among other standardisation organisations, began creating mm-wave WBAN-specific standards. There are various benefits to using mm-wave frequencies, like those in the 24 GHz range, in WBANs. WBANs at mmWave have the following challenges [5]:

1. Frequency: The mmWave band, with its high-frequency spectrum resources, facilitates faster data transfer rates in MMWave-based WBANs. This supports significantly higher data rates, enabling the real-time transfer of large data volumes, particularly advantageous for applications like high-resolution medical imaging. However, the short wavelength of mmWave signals results in a limited range, making them susceptible to signal attenuation and obstruction by objects like walls, furniture, and human bodies. As a result, mmWave-based WBANs are designed for short-range communication within a few meters.
2. Antenna design: In mmWave-based WBANs, antenna design is critical. Antennas must be more directed and smaller because of the reduced wavelength to focus the signal on the intended receiver. EBG structures can be employed to make the antenna highly insensitive to body proximity and shape conformity.
3. Power consumption: WBAN devices require effective power control. mmWave communication may use more power than lower frequency bands since it often involves higher data rates.

Overall, by offering high-speed, real-time wireless communication for monitoring and diagnostics, mmWave-based WBANs have the potential to revolutionise healthcare and related fields. However, they also present particular challenges which indicate the need for careful system design and technological improvements.

1.1 Research Motivation

Current WSN technologies used for WBAN have some major shortcomings and problems as BAN works in extremely volatile environments. Body tissue's absorption of Electromagnetic energy and cluttered working circumstances increases path loss. Intrinsic and stringent constraints of sensor design, placement of the sensor on the body, movement artifacts, pose of the human body, sensor malfunction, and interference could bring about inaccurate and incomplete reception of information. The rigorous requirement of size, flexibility, and regulations of SAR (specific absorption rate) and power radiation made antenna design quite challenging [6].

On the other hand, deficiency in the available frequency spectrum has been drastically increasing due to fast-growing new wireless technologies. Because of Congestion, Interference caused by coexisting multiple wireless systems drastically degraded performance and lower energy efficiency [7]. Therefore, Spectrum utilization efficiency is an important factor to be considered in the design process.

The human body's motion significantly affects the accuracy of estimated physiological parameters due to the large size and weight of the sensor device. Sensor devices obstruct the usual activity and movement of the human body [8]. Therefore the size, weight, and flexible material should be considered in the development of sensor devices. Steps should be taken to miniaturize the sensor devices and prevent any chemical and physical harm to the body in the pursuit of long-term use. As in E-Health real-time monitoring system, the sensor node is supposed to be attached to the human body for a long duration. There is still work remains related to motion and body posture challenges in body-centric wireless communication systems [9]. Especially for applications such as monitoring of daily human activities and sportsperson training as motion and body postures cause some serious problems in communication. Therefore, the routing protocol must consider these body movements and postures as these might introduce channel fading, interference with neighboring WBAN, and increases BER [10].

On the other hand, mm-waves frequencies offer many benefits such as large data rates for real-time transmission, low latency, reduction in interference due to the uncongested spectrum, miniaturization of devices, and unlicensed frequency bands. These advantages are now attracting researchers to explore the mm-wave frequencies as an alternative venue for WBAN [5]. Furthermore, because of the advancement in CMOS technology, low-cost power-efficient mm-wave transceivers (which occupy an area of a few mm) made it feasible for very short-distance high data rate applications such as WBAN.

Conventional MAC layer protocol design fundamentals may need a thorough reconsideration as mm-Wave systems have severe channel attenuation, stringent hardware constraints, directional communication, vulnerability to obstacles, reduced interference footprint, and potentially high signaling overhead. In the literature, up to now, PHY and propagation issues received far more attention as compared to the medium access control (MAC) layer. However, Differences between existing communication technologies and mm-Wave networks challenge conventional design approaches [11].

1.2 Research Aims and Objectives

The objective of this thesis research is to analyse and characterise on-body radio propagation in the 24 GHz ISM band using both single and multiple antennas. The choice of 24 GHz frequencies is motivated by their potential for high data rates, reduced interference in the uncongested spectrum, device miniaturization, and the availability of unlicensed frequency bands. A combination of measurement campaigns and simulations was conducted to analyse and investigate the performance of potential MAC (CSMA) protocol for WBAN at 24GHz.

The main objectives of the study include:

- Design and develop various types of antennas with specific radiation patterns, including directional (end-fire) and omnidirectional patterns. These

antennas should possess characteristics such as compactness, flexibility, and ease of wearability on the human body. Additionally, it is crucial for these antennas to exhibit high insensitivity to human skin and structural deformation.

- Characterise the on/off-body radio channel at 24 GHz and develop an empirical path loss model specifically for body-centric wireless communication. The research will particularly focus on analysing the waist-to-torso link in a typical indoor environment. Furthermore, the impact of the antenna radiation pattern will be incorporated into the modeling of the on-body channel.
- Investigate and analyse the performance of the Zigbee protocol, specifically its physical layer and MAC (Media Access Control) components, under the influence of the 24 GHz on-body propagation path-loss model in the ISM band.

1.3 Overview of Thesis

Aligned with the research objectives, the remaining sections of the thesis are structured as follows:

Chapter 2 provides an overview of the essential concepts related to wireless body area networks (WBANs). It includes a concise introduction to wearable antennas, electromagnetic band gap structures, mm-wave channel models, mm-wave multiple access transmission schemes (MAC), and the Zigbee architecture.

Chapter 3 provides an introductory overview of wearable antennas specifically designed for Wireless Body Area Networks (WBANs) operating at 24 GHz. This chapter showcases various types of antennas that are flexible, thin, and compact in nature. The first is a low profile thin layered bow-tie antenna integrated with a dual split square ring EBG structure. The second antenna highlighted in this chapter is a compact circular antenna featuring radial stubs and meandering slits. It is specifically designed for on-body WBAN applications within the 24 GHz

ISM band. Moreover, this chapter delves into the exploration and evaluation of planar end-fire array and tapered slot antenna configurations for their suitability in mm-wave wearable applications.

Chapter 4 introduces two iterations of Koch fractal geometry applied to the design of a bow-tie slot antenna backed by an Electromagnetic Band Gap(EBG) structure. The proposed antenna geometry incorporates Koch fractal-based bow-tie slots on a radiating monopole, complemented by a compact 5x5 cell EBG structure. This arrangement exhibits both bandgap characteristics and the necessary phase reflection required at the 24 GHz ISM band. As a result, surface waves and the back-lobe of the antenna are significantly reduced. The performance of the prototyped EBG-backed antenna is thoroughly analysed in Chapter 4, considering parameters such as the reflection coefficient (S11), radiation pattern, suitability for on-body operations, resistance to structural bending, and Specific Absorption Rate (SAR). It is worth noting that the proposed Koch fractal bow-tie slot antennas are the thinnest EBG-backed antennas reported in the K band.

Chapter 5 focuses on conducting an extensive examination of sectorized 24 GHz on-body radio propagation channels in indoor environments. The goal is to determine the propagation parameters, such as the path loss exponent and shadowing factor, for on-body communication systems. Additionally, this chapter investigates the influence of various antenna types on the performance of these systems. To explore the significant characteristics of antennas that should be incorporated for on-body channels, four antenna types are selected for this investigation: Bow-tie, EBG-backed Bow-tie, Yagi Uda, and Vivaldi antennas. The selection of these antennas aims to demonstrate their distinct radiation propagation characteristics and their impact on the performance of on-body communication systems.

Chapter 6 provides a comprehensive examination and analysis of the system-level modeling for the Zigbee protocol, specifically focusing on its physical layer and MAC components when applied to the mm-wave radio architecture for body-centric communications. This chapter builds upon the performance analysis of

the Carrier Sense Multiple Access (CSMA) protocol in the context of the 24 GHz channel model, which was previously presented in Chapter 5.

Chapter 7 offers a comprehensive summary of the primary contributions and findings derived from the study, effectively concluding the completed work. Additionally, this chapter presents potential avenues for future research activities.

References

- [1] Akbar, M. S., Yu, H., Cang, S. "Delay, reliability, and throughput based QoS profile: A MAC layer performance optimization mechanism for biomedical applications in wireless body area sensor networks." *Journal of Sensors*, 2016.
- [2] Ullah, F., Abdullah, A. H., Kaiwartya, O., Kumar, S., Arshad, M. M. "Medium Access Control (MAC) for Wireless Body Area Network (WBAN): Superframe structure, multiple access technique, taxonomy, and challenges." *Human-centric Computing and Information Sciences*, 7(1), 34, 2017.
- [3] Abbasi, Q. H. , Ur-Rehman, M. , Qaraqe, K. and Alomainy, A. (Eds.) "Advances in Body-Centric Wireless Communication: Applications and State-of-the-art. Series:" *IET telecommunications series. Institution of Engineering and Technology*: London 2016.
- [4] Barakah, D. M., Ammad-uddin, M. "A survey of challenges and applications of wireless body area network (WBAN) and role of a virtual doctor server in existing architecture." In *Third International Conference on Intelligent Systems Modelling and Simulation*, pp. 214-219), 2012.
- [5] Estevez, C. I., Wei, J., Kailas, A., Fuentealba, D., Chang, G. K. "Very-high-throughput millimeter-wave system oriented for health monitoring applications." *IEEE 13th International Conference on e-Health Networking, Applications and Services*, pp. 229-232, June 2011.
- [6] Ghamari, M., Janko, B., Sherratt, R. S., Harwin, W., Piechockic, R., Soltanpur, C. "A survey on wireless body area networks for healthcare systems in residential environments." *Sensors*, 16(6), 83 (2016).

- [7] Chakraborty, C., Gupta, B., Ghosh, S. K. "A review on telemedicine-based WBAN framework for patient monitoring." *Telemedicine and e-Health*, 19(8), 619-626, 2013.
- [8] Antonescu, B., Basagni, S. "Wireless body area networks: challenges, trends and emerging technologies." *In Proceedings of the 8th international conference on body area networks*, pp. 1-7, September 2013.
- [9] Reusens E, Joseph W, Latre B, Braem B, Vermeeren G, Tanghe E, et al. "Characterization of on-body communication channel and energy-efficient topology design for wireless body area networks." *IEEE Trans Inf Technol Biomed.*;13:933–45, 2009.
- [10] Yang, X., Matthaiou, M., Yang, J., Wen, C. K., Gao, F., Jin, S. "Hardware-constrained millimeter-wave systems for 5G: Challenges, opportunities, and solutions." *IEEE Communications Magazine*, 57(1), 44-50, 2019.
- [11] H. Shokri-Ghadikolaei et al., "Millimeter Wave Cellular Networks: A MAC Layer Perspective," *IEEE Trans. Commun.*, vol. 63, no. 10, pp. 3437–58, Oct. 2015.

Chapter 2

Background and Literature Review

2.1 Introduction

Research in wireless body area networks often focuses on unlicensed frequency bands, including the ISM bands at 434 MHz, 915 MHz, and 2.45 GHz, and the ultra-wideband (UWB) from 3.1 GHz to 10.6 GHz [[1]- [14], [15]- [27]]. The IEEE 802.15.6 standard encompasses these frequency bands. Each band has its advantages and disadvantages. Lower frequencies exhibit minimal attenuation and better penetration into the human body, but offer limited bandwidth and increased interference. Additionally, larger antennas are required due to the longer wavelength. Higher frequency bands reverse these characteristics. Hence, the selection of the operational frequency necessitates a careful equilibrium between considerations such as propagation losses, antenna dimensions, the potential for interference, and the demands of data transmission speed.

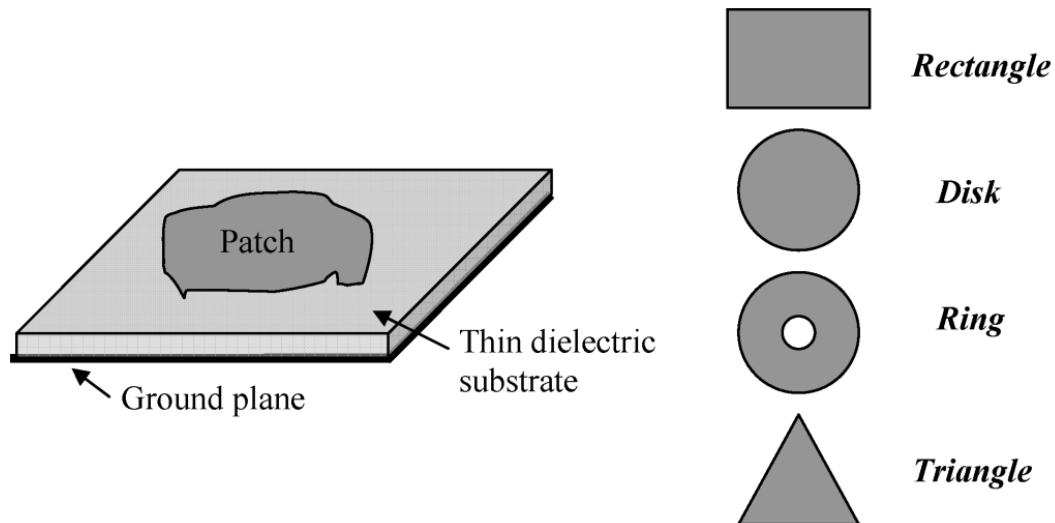


FIGURE 2.1: The basic structure of the microstrip patch antenna

2.2 Fundamental Concepts and Principles

Certain fundamental Concepts and theories are presented prior to delving into the topic of wireless body area networks, and these foundational Concepts are applied throughout the subsequent chapters.

2.2.1 Microstrip Antennas

The concept of microstrip patch antennas emerged from the use of printed circuit technology, where both the radiating components and circuit elements are integrated. The initial suggestion was made by Deschamps [28], but it received little attention until the 1970s. Since then, extensive research and development have been conducted on microstrip patch antennas, resulting in numerous books, papers, and review articles on the subject [[30]- [37]].

The fundamental structure of a microstrip patch antenna is illustrated in Fig. (2.1). It consists of a metalized area placed above a ground plane and supported by a thin dielectric substrate, with proper grounding. While the patch shape can be theoretically arbitrary, practical designs often take the form of a circle, rectangle, equilateral triangle, or annular ring. Fig. (2.2) illustrates four different feeding strategies for microstrip patch antennas: proximity feed, aperture-coupled

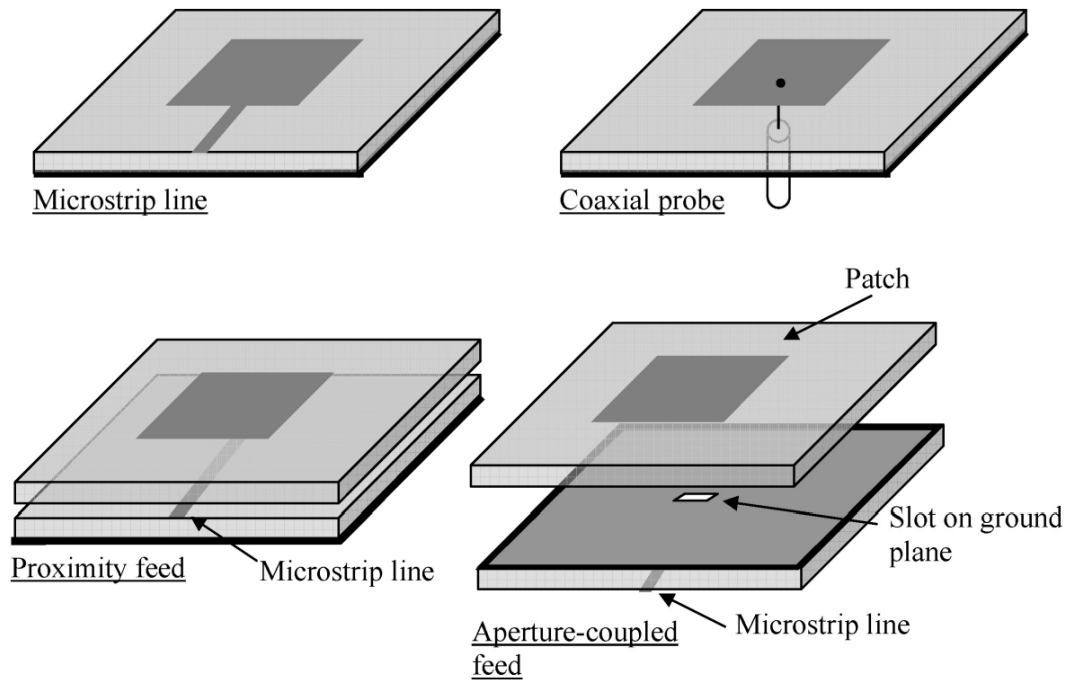


FIGURE 2.2: Four common feeding methods of microstrip patch antenna

feed, coaxial probe feed, and microstrip line feed. The use of microstrip line and co-planar waveguide-fed techniques are more suitable for Wireless Body Area Networks (WBANs). These feeding methods offer increased ease in the wearability of antennas on the body. The region beneath the patch acts as a resonant cavity with open circuits on the sides, initially receiving electromagnetic radiation. When a portion of the energy escapes the cavity, it radiates into space, thus forming the antenna structure.

2.2.2 S parameters / Two-port network

The term "two-port network" pertains to an electrical circuit or device equipped with two sets of terminals intended for connection to external circuits. A port is formed by two terminals when the currents flowing into one terminal are equal to the currents flowing out of the other terminal on the same port. This fundamental principle, known as the port condition, ensures the conservation of electric current within the two-port network [38].

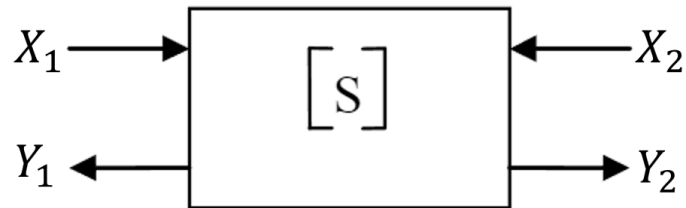


FIGURE 2.3: Illustration Involving a two-port network and S-parameters

In circuit analysis, the two-port network model is commonly employed to isolate specific sections of larger circuits. A "black box" representation is utilized, where a matrix of integers describes the properties of the two-port network. This approach eliminates the need to solve for internal voltages and currents within the network, simplifying the computation of its response to applied signals at the ports. The two-port networks considered in this thesis include a two-port travelling wave antenna and the radio channels.

$$\begin{bmatrix} Y_1 \\ Y_2 \end{bmatrix} = \begin{bmatrix} S_{11} & S_{21} \\ S_{12} & S_{22} \end{bmatrix} \begin{bmatrix} X_1 \\ X_2 \end{bmatrix} \quad (2.1)$$

The behavior of the two-port network is characterised using incident and reflected waves at the ports, which are defined by S-parameters. S-parameters are particularly useful at UHF and microwave frequencies, where it becomes challenging to directly measure voltages and currents. They provide an effective means of analysing the network's performance and understanding signal transmission and reflection within the system.

In the context of a two-port network, the symbols " X_i " represent the incident waves at port i , while the symbols " Y_i " denote the reflected waves at port i . This relationship between incident and reflected waves can be visualised in Fig. (2.3), which illustrates an example of a two-port network along with its corresponding S-parameters.

2.2.3 Propagation Loss

Path loss, also known as attenuation, refers to the reduction in power density experienced by an electromagnetic wave as it propagates through space. This concept is widely used in radio propagation and wireless communications. Several factors contribute to path loss, including free-space loss, refraction, diffraction, reflection, aperture-medium coupling loss, and medium absorption. In the context of Wireless Body Area Networks (WBANs), the attenuation of signal strength, known as path loss, is additionally impacted by factors such as the shape of the terrain, the characteristics of the environment, the medium through which signals propagate (specifically, the human body), fluctuations in the distance between the transmitter and receiver due to bodily motions, as well as the elevation and positioning of antennas across various body regions.

A direct line-of-sight trajectory across clear and unobstructed surroundings, devoid of objects that could reflect or diffract the signal, results in what is termed as free-space path loss (FSPL). This phenomenon denotes the decline in the strength of an electromagnetic wave as it propagates through space. The FSPL equation is:

$$FSPL = \left(\frac{4\pi d}{\lambda}\right)^2$$

In the given equation, λ represents the wavelength of the signal, f denotes the frequency of the signal, d represents the distance from the transmitter, and c represents the speed of light in a vacuum.

The Free-Space Path Loss (FSPL) acts as a reference point for estimating the anticipated signal strength between a transmitter and a receiver, disregarding the influence of obstacles, reflections, or diffractions. However, in the context of Wireless Body Area Networks (WBANs), the applicability of free-space path loss diminishes due to the unique challenges posed by the on-body environment. In WBAN scenarios, the presence of the human body and its dynamic movements introduces signal attenuation and reflection.

2.3 Wearable Antenna design

Wearable antennas must satisfy three key criteria. Initially, the antennas need to possess a sleek, lightweight design that seamlessly conforms to the body. Following that, the antennas must demonstrate a lack of sensitivity to the immediate presence of the human body. Additionally, they should showcase a radiation pattern that minimises signal loss and interference, all the while adhering to established guidelines for human safety in terms of radiation absorption, such as the specific absorption rate (SAR). In the design of wearable antennas, essential factors like antenna efficiency and proper impedance matching become critical due to the close proximity of the human body, which has the potential to significantly influence the antenna's operational performance.

In most wearable antenna designs, either a ground plane or an electromagnetic band-gap (EBG) backing layer is employed to provide shielding for the radiating components against the body, thus leading to an enhancement in antenna efficiency. However, for wireless body area networks, challenges arise concerning the antenna's emission pattern and its effect on perceived path gain. Measurements have shown that the link shape and antenna type significantly influence the path gain. Moreover, the positioning of antennas also plays a vital role in determining how electromagnetic waves propagate. For instance, The connection between the head and waist is primarily characterised by the propagation of surface waves or creeping waves, as mentioned in reference [53]. On the other hand, the link from the waist to the wrist primarily encounters the propagation of space waves when there are no obstacles between the transmitting and receiving points.

2.3.1 Wearable antennas

Research has explored various types of antennas suitable for applications worn on the body, such as planar dipoles, monopoles, planar inverted-F antennas (PI-FAs), and microstrip patches. [[54], [21], [22]]. The effectiveness of monopole antennas in reducing path loss and fading in on-body communication channels,

when compared to other antenna types, can be attributed to their advantageous characteristics such as a simple design, vertical orientation, and resistance to fading. Planar inverted-F antennas ranked second in on-body performance. However, other antennas like dipoles, loops, and printed-F antennas exhibited high losses near the body. Microstrip patch antennas, while low profile and conformal, typically provide off-body radiation patterns.

To address size constraints, miniaturization techniques were employed, such as multiple folded arms, inductive and capacitive loading, and the use of high permittivity or permeability materials [[55]- [57]]. However, these techniques sometimes compromise antenna efficiency and directional radiation patterns. Antenna arrays were explored for on-body applications, but their large size and limited beam control posed challenges in achieving high angular resolution of the radiation pattern at these frequencies [[58], [59]]. Despite these difficulties, researchers have proposed innovative solutions, such as a high-mode microstrip patch antenna launching creeping waves and a surface wave antenna applying Yagi-Uda principles [2]. These advancements continue to improve on-body antenna design and address the unique challenges of wearable communication systems.

Recent efforts have also been dedicated to exploring UWB wearable antenna designs, considering the need for good impedance matching, radiation characteristics, and preservation of pulse shape [[22]– [25]]. Additional parameters, such as impulse response, frequency domain transfer function, and time spread, are crucial in UWB antenna design. The majority of UWB antennas suggested for Wireless Body Area Network (WBAN) communications are adaptations of monopole/dipole antennas and slot antennas, as noted in reference [60]. Additionally, researchers delve into the examination of antenna effectiveness when situated near the human body, with a specific emphasis on aspects like signal integrity, specific absorption rate (SAR), and radiation efficiency [61]. UWB antennas offer advantages, including smaller size with increasing frequency and the potential for achieving high gain, with some UWB Vivaldi antennas reaching up to 10 dBi gain. While beamforming techniques have been reported in the literature, Antenna arrays equipped

with beamforming capabilities are still too bulky for use in wearable applications on the body [62].

Antennas based on textile materials have gained significant attention worldwide due to their comparable performance to conventional antennas, along with being lightweight, flexible, and easy to integrate into clothing [[63]- [66]]. These attributes render them as potential contenders for integration into wireless body area networks. Diverse traditional antenna models, spanning microstrip patch antennas, slot antennas, dipole antennas, PIFA, loop antennas, and spirals, have effectively been incorporated into textile substrates to cater to both narrowband and ultra-wideband (UWB) applications. [[67]- [71]]. Table 2.1 provides the pros and cons of The above-mentioned antennas. They are not very popular and have a lot of challenges as textiles, owing to their flexibility, can undergo deformation, impacting the performance of integrated antennas, as these antennas typically require the maintenance of specific shapes and dimensions for optimal functioning. Additionally, the presence of conductive textiles or body tissues can lead to detuning, altering the resonant frequency of the antenna.

Challenges also arise in seamlessly integrating textile antennas with electronic components while preserving flexibility and wearability. The proximity of multiple antennas may result in mutual coupling, influencing the performance of individual antennas. Furthermore, textile antennas must exhibit durability for withstanding washing and typical wear associated with clothing. Finally, the absorption of RF energy by the human body can impact the on-body antennas' overall performance. Nevertheless, incorporating an electromagnetic band-gap (EBG) ground plane can alleviate these impacts and reduce the specific absorption rate (SAR) associated with the antenna [72].

TABLE 2.1: Pros and cons for different types of antennas when integrated into textile substrates

Antenna Type	Pros	Cons
Patch Antenna	Lightweight, low-profile, and conformable to textile substrates.	Limited bandwidth, sensitivity to bending, potential for detuning due to textile properties, and mutual coupling.
Slot Antenna	Simple design, low profile, and can be integrated directly into the fabric.	Limited bandwidth, sensitivity to bending, and potential for mutual coupling.
Dipole Antenna	Simple structure, easy integration into textiles, and relatively wide bandwidth.	Limited compactness, sensitivity to bending, and potential for radiation pattern distortion.
PIFA (Planar Inverted F Antenna)	Compact design, low profile, and can be easily integrated into textile substrates.	Limited bandwidth, sensitivity to bending, and potential for detuning due to the presence of nearby conductive materials.
Loop Antenna	Low profile, compact design, and can be integrated into clothing or accessories.	Limited bandwidth, sensitivity to bending, and potential for mutual coupling.
Spiral Antenna	Compact and planar structure, suitable for wideband applications.	Limited efficiency, sensitivity to bending, and potential for detuning.

2.4 Radio channel characterisation for WBANs

In order to develop future communication standards and design efficient transceivers for Wireless Body Area Network (WBAN) systems, it is essential to have a comprehensive understanding of the characteristics of the propagation channels used. In WBAN applications, the optimal utilisation of propagation channels is of utmost importance due to the compact size and limited battery power of the devices. The

positioning of antennas on or within the body, user movements, and environmental factors all play a significant role in determining the behavior of propagation channels.

Considering the diverse range of WBAN applications, different methods of communication may be required. Generally, three distinct types of transmission channels can be identified [[5]– [16]]:

Off-body channel: This involves communication between an external device located on a body-worn device and another body-worn device attached to an item or another person. Examples include communication between a smartwatch and a smartphone, or between a wearable fitness tracker and a wireless headset.

On-body channel: This refers to the interaction between two gadgets mounted on the same person’s body. For instance, communication between a chest-worn electrocardiogram (ECG) monitor and a wrist-worn activity tracker falls under the category of on-body channels.

In-body channel: This type of channel involves communication between a device located on the surface of the body and an implanted device within the human body. Examples include wireless communication between a wearable insulin pump and a glucose monitoring implant.

In practice, body area network channels are often categorised based on the locations of the transmit and receive antennas on the body, commonly referred to as ”on-body channels.” Examples of these on-body channels include abdomen-to-head or abdomen-to-chest channels, which offer valuable insights into the specific placement of devices for achieving optimal signal propagation. Considerable research efforts have been directed towards studying the characteristics of on-body channels connecting a communication hub located on the abdomen with positions on the head, wrist, chest, back, and ankle, as documented in references [3] and [4].

2.4.1 Measurements of communication channels and empirical modelling

Many propagation investigations outlined in existing literature have predominantly adopted an empirical methodology. [[1]– [20], [23], [24]– [27]]. These investigations are commonly conducted in indoor environments [[3], [4], [6], [10], [11]], although certain studies have explored anechoic chambers [[11], [16]] and outdoor settings [[11], [39]].

In most cases, researchers have employed network analysers to measure transmission loss [[3], [10], [11], [16]]. This approach provides a combination of high precision and an extensive dynamic range made available by network analysers. However, it has the drawback of requiring the connection of antennas to the network analyser through coaxial cables, which can introduce measurement distortions [[10], [40]– [43]]. To address this issue, a few research groups have implemented fiber optic cables to link the antennas with the network analyser [[42], [44]].

Others have utilised small wearable transmitters and receivers to record received signal strength indicator (RSSI) and measure propagation path loss [[27], [30], [45]]. This method also has some issues as well like ensuring synchronised data acquisition between wearable transmitters and receivers is crucial for accurate RSSI measurements. Asynchronous data collection may introduce errors in path loss calculations. Achieving accurate and consistent RSSI measurements across different devices and scenarios requires proper calibration and standardisation procedures. The lack of standardized methods can lead to inconsistencies in path loss models.

Significant efforts have been dedicated to investigating Ultra-Wideband (UWB) propagation channels [[23], [25]– [26]], as UWB technology is considered a promising candidate for future Body Area Network (BAN) standards, Offering high data rates for communication links within both on-body and in-body contexts, however, current Body Area Network (BAN) standards function within limited frequency

ranges, notably around 400 MHz and 2.45 GHz. As a result, research into propagation channels at these frequencies, as well as other license-free bands, has been undertaken. Various research groups in the UK, Belgium, Japan, and Australia have extensively explored measurement studies across diverse Industrial, Scientific, and Medical (ISM) frequency bands. [[1]– [22]].

2.4.1.1 Narrowband channel characterisation

Propagation near the human body experiences a blend of space waves, surface waves, and diffracted waves. The prevalence of each kind hinges on antenna positions and bodily motions. In scenarios with an unobstructed view between antennas, space wave propagation takes place. Conversely, when antennas encounter blockages or shadows, propagation entails surface wave and diffracted wave mechanisms. A research endeavor conducted at 2.45 GHz illustrated the relationship between on-body path gain and the distance between antennas, revealing that direct line-of-sight (LOS) connections followed a power law attenuation trend as distance increased, while non-line-of-sight (NLOS) links displayed exponential attenuation. [[20]]. Another study derived a model to describe the variation of path loss with frequency and distance [13]. Measurements of path loss around the torso were performed and showed an exponential increase in the shadow region [[10], [16]]. Furthermore, a model was put forth to encompass the fluctuation in path loss encircling the torso, taking into account the waves that are reflected by the surroundings. [10].

2.4.1.2 UWB channel characterisation

Extensive investigations of Ultra-Wideband (UWB) propagation channels have been carried out by numerous research teams worldwide [[23], [46]– [52]]. Most of these studies utilised a network analyser for measurements, except for a few exceptions [[46]]. Numerous studies have calculated the average path loss spanning the complete UWB spectrum, and they have investigated how the average path loss

changes as the distance between antennas is altered in various locations encircling the torso [[46]- [52]]. The typical approach to representing the change in path loss with distance involved using linear or logarithmic fitting to logarithmic path loss data [[46], [47], [52]].

2.4.1.3 60 GHz mm-wave channel characterisation

Several groups have focused their efforts on different aspects of 60 GHz indoor communications to ensure their inclusion in the IEEE 802.11ad standard [113]. One such endeavor in [114] involves characterising human mobility using a random walk model combined with knife-edge diffraction. This approach has resulted in the development of a cluster blockage probability that is easy to implement within the standard.

Additionally, [115] presents measurements conducted in an indoor environment with the aim of determining the most significant attenuation caused by human occlusion. Furthermore, [116] evaluates the likelihood of connection blockage for a transmitter positioned on the ceiling. More recently, cylindrical models of the human body have been proposed and examined in [117] as part of ongoing research efforts in this domain. Studies have shown that a perfect electric conductor (PEC) cylinder can effectively approximate the human anatomy, with no significant differences observed between circular and elliptic cylinders. Utilising such simplified body geometry, researchers have developed analytical models for 60 GHz body area networks [118].

Investigations into the influence of clothing on signal propagation have been carried out in [119], revealing the minimal impact on path loss caused by various garment layers and styles. Moreover, the same group of researchers has developed an electro-textile with unique electric characteristics, exhibiting high conductivity, which resulted in a notable reduction in route loss [120]. Due to recent advancements in numerical phantoms of the human body [121], it is now possible to create a model with a sub-millimeter mesh.

2.5 Millimeter wave communication and a MAC layer perspective

Wireless communication at centimeter-wave or mm-wave frequencies is considered the best option to achieve high data rates in upcoming future wireless networks. However, these very high-frequency waves undergo huge attenuation, deafness, and blockage, and may require microwave or sub-GHz networks for synchronisation and fallback support.

mm-Wave communication systems have special hardware constraints and propagation characteristics that introduce new challenges for efficient MAC and physical layer design. The hardware structure of a millimeter-wave transceiver based on an antenna array is intricate and encompasses numerous RF analog elements. Of particular significance, these analog components are often subject to imperfections stemming from manufacturing anomalies. Consequently, various hardware flaws such as phase noise, non-linear behavior in power amplifiers, IQ imbalance, and similar issues, tend to arise, particularly in millimeter-wave frequencies [73].

While the traditional hardware limitations are present in sub-6 GHz wireless systems, their effects become more pronounced in millimeter-wave (mm-Wave) systems. Additionally, in mm-Wave systems, the challenges of extensive real-time baseband signal processing become more prominent due to the utilisation of large bandwidths. These factors compound the issues associated with hardware imperfections like phase noise, non-linearities in power amplifiers, IQ imbalances, and more. Consequently, the performance of mm-Wave systems is considerably susceptible to these hardware limitations and imperfections. Hence, conducting a comprehensive analysis and design, along with the exploration of potential solutions, becomes crucial in mitigating these challenges [74].

mm-Waves experience high path loss, and high penetration loss, and possess large available bandwidth. Due to very small wavelengths, large numbers of antenna elements can be implemented in the given size of radio chips. This increases the attainable antenna gain at the expense of extra signal processing. The high gain

antenna array can completely compensate for the large path loss of mm-Wave systems without any increase in transmission power. Deafness and blockage are the main issues in mm-Wave networks due to vulnerability to obstacles and directional communications [76]. Deafness is the non-line of sight position of antennas of the transmitter and the receiver preventing the initiation of a directional communication link. Blockage refers to enormous attenuation due to obstacles (e.g., the human body attenuates signals up to 35 dB [76]) that cannot be compensated by extra transmission power or using the high-gain antennas.

Numerous operations within a network, including tasks like establishing communication links, discovering neighboring devices, sharing routing details, and coordinating access to channels, heavily rely on the exchange of signaling messages over a designated control channel. The unique attributes of millimeter-wave (mm-Wave) communication introduce certain dilemmas related to fallback and directionality. Specifically, the fallback trade-off refers to the decision-making process between transmitting control messages via either an mm-Wave or microwave channel. The challenge arises due to the potential blockage issue faced by mm-Wave channels, leading to reduced reliability of the control channel. As a result, the deployment of a dedicated microwave control channel emerges as a solution for enhancing network synchronization and broadcast capabilities. However, this solution comes with an increased hardware complexity and power consumption, as it entails the addition of an extra microwave transceiver for managing the control channel [77].

2.5.1 Medium Access Control (MAC):

A set of rules and processes used in the MAC layer to control how devices access the common communication medium are referred to as MAC protocols, also known as Media Access Control protocols. These protocols specify how devices compete for the right to send data, how they handle collisions when several devices try to transmit at the same time, and how they make sure network resources are used fairly and effectively. For example, CSMA/CD - Carrier Sense Multiple Access with Collision Detection - and CSMA/CA - Carrier Sense Multiple Access with

Collision Avoidance - are MAC protocols that are specifically made for Ethernet and Wi-Fi, respectively. To ensure efficient and reliable communication between networked devices, each MAC protocol has its own processes and techniques for restricting access to the shared medium and managing the flow of data.

The MAC protocol maximizes power efficiency and enhances performance and network reliability by reducing the effects of collisions. Several researchers proposed many energy-efficient MAC protocols for WBANs. The proposed MAC protocol [78] displays fundamental techniques (such as low-power listening, scheduled channel polling, and periodically turn on/off radio) for generic wireless sensor networks to attain small delay and low throughput.

In reference [79], collision, overhearing, and idle listening were identified as challenges to Energy efficiency in wireless sensor network MAC protocol. Medium access control protocols are generally classified as contention-based and contention-free. Contention takes place when two or more sensor nodes of the network seek to access the same communication channel simultaneously. It is very likely to happen when traffic is frequent and correlated, and it reduces the lifespan of WSN [80]. The contention-free MAC protocol does not allow any data collisions. In literature, almost all proposed contention-free MAC protocols considered the scenario of time-synchronized sensor nodes. However, this is not possible for large sensor networks. Contention-based MAC protocols are typically based on random access principles; however, these protocols often incorporate certain refinements when compared to purely random access schemes like Aloha. In contention-based MAC, sensor nodes access the channel without any coordination with each other. After the collision of data, both nodes have to wait for some random duration and attempt again [80].

In the literature, many researchers presented examples of contention-based and contention-free MAC protocols [79]. FDMA based MAC is not suitable for wireless sensor networks, although it provides collision-free communication. That's

because of challenging front-end hardware design, especially filters. CSMA/CA-based MAC has a simple structure, better reliability, and quite high energy consumption. Conversely, TDMA-based MAC is energy efficient. However, TDMA is not scalable and requires node synchronization. The auxiliary radio channel is used to wake the scheduled node for transmission. This alternate method involves out-of-band communication channels to minimize idle listening and power consumption [80].

Conventional MAC layer protocol design fundamentals may need a thorough reconsideration as mm-Wave systems have severe channel attenuation, stringent hardware constraints, directional communication, vulnerability to obstacles, reduced interference footprint, and potentially high signaling overhead [75]. In the literature, up to now, PHY and propagation issues received far more attention as compared to the medium access control (MAC) layer. However, Differences between existing communication technologies and mm-Wave networks challenge conventional design approaches.

The properties of mm-wave signals cause a lot of challenges like misalignment of transceivers due to the deafness problem, which further complicates the control channel selection technique in node position identification and link establishing with node. Therefore control channel selection mechanism necessitates deciding the adoption of either mm-wave or microwave and the antenna type (Omni, semi, or directional) for the control channel. Line of sight blockage and node movements can disrupt the connection and pose challenges to link robustness.

2.5.2 Literature related to WBANs MAC

In the E-health monitoring system, Each distinct vital sign category is associated with a specific type of medical data, setting it apart from other vital signs. In the context of body sensor networks, several resource limitations come into play, including inadequate energy, processing capabilities, and limited memory. Consequently, devising an effective medium access protocol presents a significant

challenge within Wireless Body Area Networks (WBANs). [83]. In the literature, various MAC protocols have been presented related to slot allocation issues in WBANs. In MAC protocols, time is divided into discrete periods or frames known as MAC superframes. These superframes serve to organise data transmission and manage information within the network, comprising various smaller frames. Typically, data frames, acknowledgment frames, and beacon frames are included as components of the superframe. Generally, the super-frame structure and multiple access (MA) schemes are the two main design decisions that have been made in MAC protocols.

The important factors while designing of MAC super-frame structure are frame format, classifications of data, and multiple access schemes. IEEE 802.15.4 and IEEE 802.15.6 both standards support super-frame structure. Multiple access schemes contain scheduling schemes and their combinations, which include Time Division Multiple Access (TDMA), Aloha, carrier sense multiple access with collision avoidance (CSMA/CA), Slotted Aloha, and Frequency Division Multiple Access (FDMA). The slot allocation approach is not a suitable solution for medical emergency data. It degrades the MAC protocol performance in terms of delay, the frequent demand of beacon interval (BI), limited slots for physiological data, retransmission of lost data packets, higher energy consumption, and small interval of Super-frame and slots.

A survey on scheduling access schemes, channel interferences, and energy consumption of IEEE 802.15.4 and IEEE 802.15.6 is performed in [84]. They investigate the challenges and issues related to the design and development of low-powered biomedical sensors (BMSs) for monitoring of physiological data of a person in several applications [85]. However, they did not recognise the limitations of the super-frame structure of IEEE 802.15.4. Fig.2.4 provides MAC Super-frame structures of IEEE standards 802.15.4, 802.15.6 and 802.15.3c

The Super-frame structure has been categorised into contention, TDMA, and low power listening device-based MAC protocols studies. The majority of MAC protocols have been formulated with a focus on wireless sensor networks (WSNs).

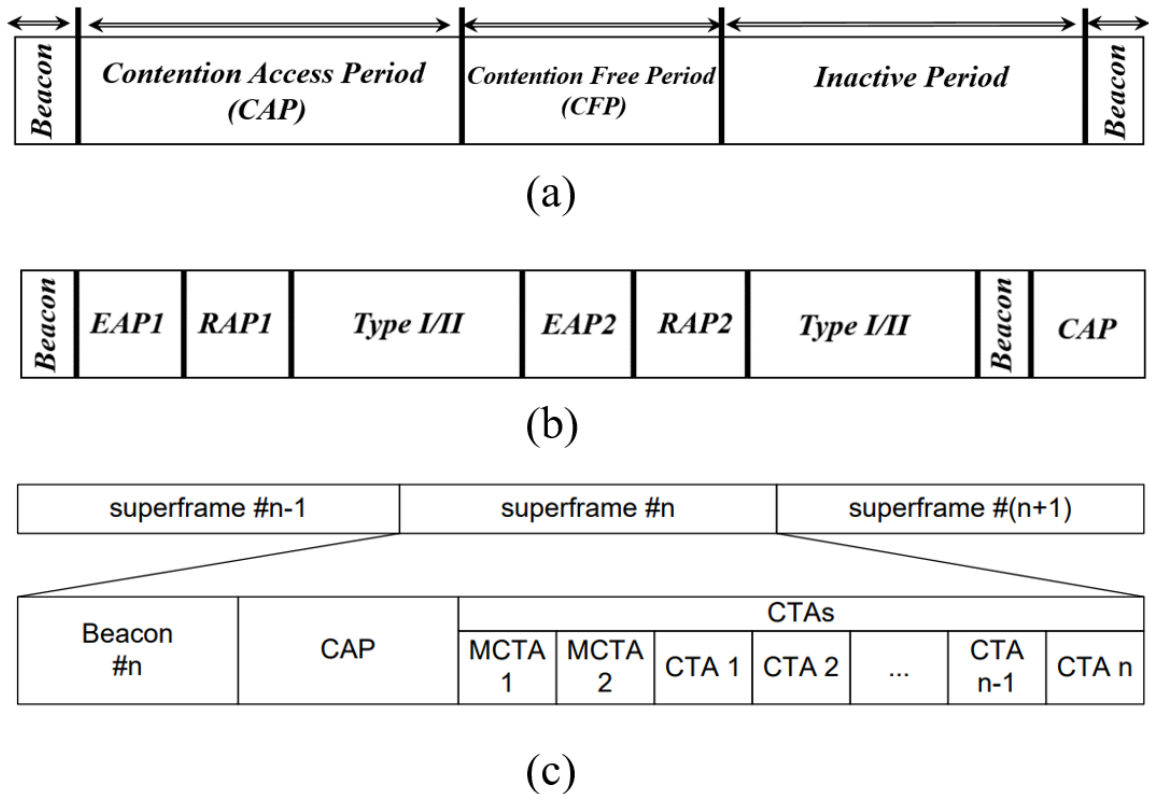


FIGURE 2.4: MAC Super-frame structures of; a) IEEE 802.15.4, b) IEEE 802.15.6 and c) IEEE 802.15.3c

Typically, wireless sensor networks exhibit a consistent type of data. However, the distinctive heterogeneity of physiological data in Wireless Body Area Networks (WBANs) results in disparate demands. This variation extends across the PHY, MAC, network, transport, and application layers, which have been scrutinized in the context of Super-frame structures within IEEE 802.15.4 and IEEE 802.15.6 standards for WBANs [86]. They examined the layers to establish an association between Super-frame structure using CSMA/CA, TDMA, and Slotted Aloha. This section classifies MAC Super-frame structures into IEEE 802.15.3c, IEEE 802.15.4 and IEEE 802.15.6 as shown in Fig.2.5.

Several IEEE standards like 802.11, 802.15, and 802.15.1 do not support the monitoring of abnormal conditions of patients. However, IEEE 802.15.4 can detect and monitor the abnormal conditions of patients and communicate physiological data with better data reliability [87]. Numerous researchers have tried to redesign the Super-frame structure of 802.15.4 MAC to use it for a body area network. Table

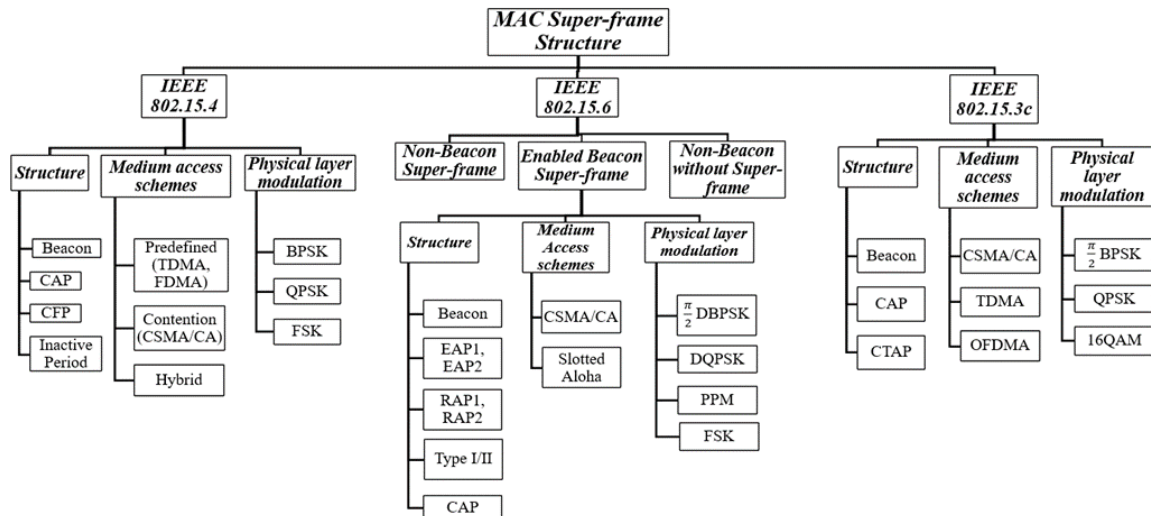


FIGURE 2.5: Classifies MAC Super-frame structures into IEEE 802.15.3c, IEEE 802.15.4 and IEEE 802.15.6

2.1 presents a comparison of WSN standards based on super-frames which include 802.15.4, 802.15.6, and 802.15.3c [88].

2.5.3 Taxonomy of MAC protocols

The challenges related to the design of an effective MAC protocol for mm-wave body-centric communications have attracted huge interest from researchers. In this section, we introduce a taxonomy of the potential MAC protocols for the mm-wave body area network as proposed in the literature, as illustrated in Fig. 2.6. These MAC protocols can be broadly classified into two architectures: directional and non-directional antenna-based.

The non-directional antenna-based protocols have been presented for WBAN at the microwave frequency range, and they can also be considered potential candidates for mm-wave WBAN. On the other hand, the directional antenna-based protocols have primarily been proposed for WPAN (Wireless Personal Area Network) in the mm-wave communication network. However, they too hold promise as potential candidates for mm-wave WBAN applications.

TABLE 2.2: Comparison of different features of WSN standards 802.15.4, 802.15.6, and 802.15.3c

Characteristics	802.15.4	802.15.6	802.15.3c
Domain	Sensors applications	WBAN applications	Personal Area Network
Data type	Homogenous	Heterogeneous	Heterogeneous
Range	10 to 100 meter	3 to 6 meter	-
Coverage	Extendable	Medium	Small
Max of sensors	10-65k	3-256	-
Power	15-30 mW	0.02-42 mW	400mW
Frequency	ISM(2.4 GHz)	UWB (3-10 GHz)	60 GHz
Data Rate	20-250 kb/s	0.05-10 Mb/s	7 Gb/s
MA scheme	CSMA/CA, TDMA, FDMA, Aloha	CSMA/CA, TDMA, FDMA, Aloha	CSMA/CA, TDMA, OFDMA
Channel allocation technique	Contention, polling-and alert based	Contention and post allocation	-

2.5.4 Evaluation and Comparison of Medium Access Scheduling Schemes

In the wireless body area network, multiple access schemes are responsible for scheduling the data transmission between body sensor nodes and coordinator [89]. In the literature, most researchers suggest a TDMA with a CSMA/CA scheduling access scheme for slot allocation in CFP and CAP periods. The low throughput, higher delay, data collision, and high power consumption deteriorates the performance of Multiple access scheme protocol during contention for sensor nodes

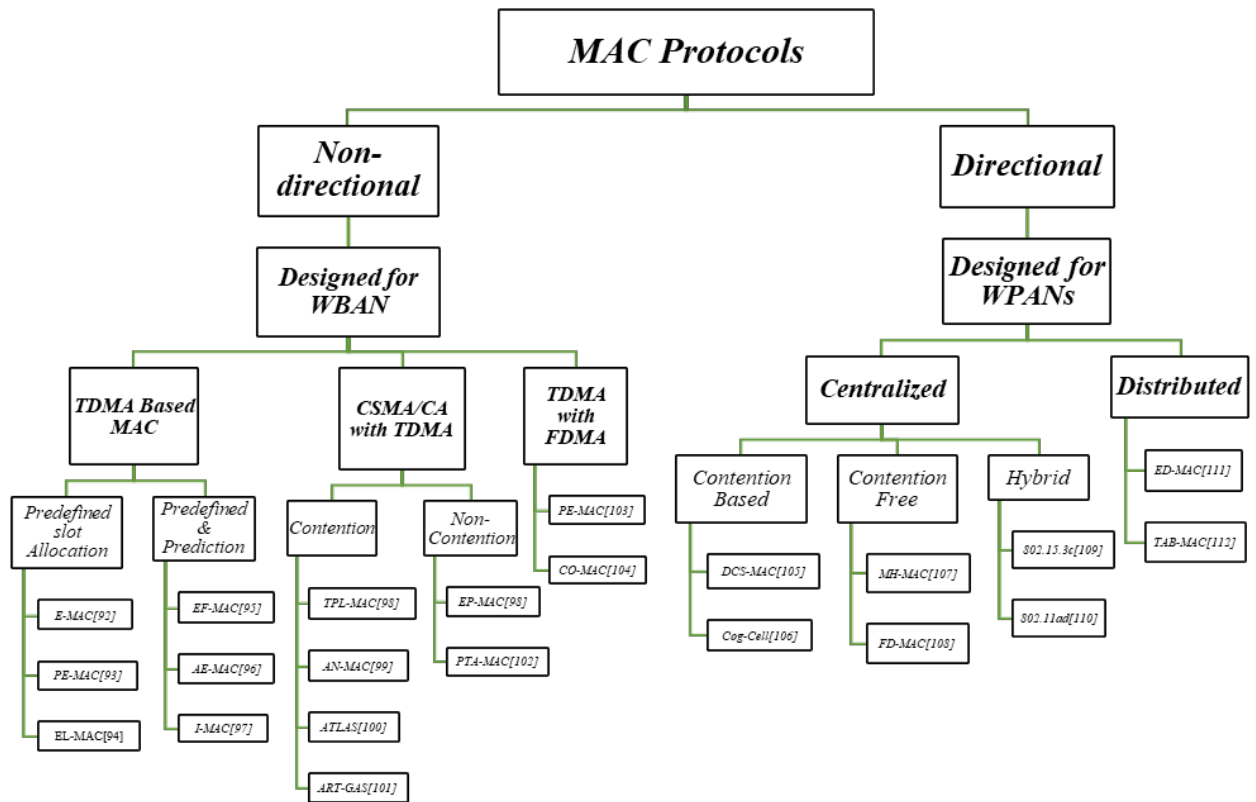


FIGURE 2.6: Taxonomy of MAC protocols in terms of directional and non-directional antenna-based architectures for WBANs and WPANs

for accessing the channel. In Time-division multiple access (TDMA), each body sensor node has allocated time slots, and nodes wait and transmit data in their predefined time slots. Therefore because of long waiting interval and contention, both TDMA and CSMA/CA schemes are not suitable for emergency scenarios. In table 2.2, Different characteristics of scheduling schemes such as Energy consumption, bandwidth, packet delivery, traffic, and synchronisation are compared [90]- [91]. However, the energy consumption of the TDMA access scheme is smaller as compared to CSMA/CA.

In summary, this chapter discusses different aspects of Wireless Body Area Network (WBAN) literature, covering things like wearable antenna designs, empirical channel characterization, and how devices communicate at microwave (2.4 GHz)

TABLE 2.3: Comparison between TDMA, CSMA/CA and FDMA

Function	TDMA	CSMA/CA	FDMA
Power consumption	Low	High	High
Preferred Traffic level	High	Low	High
Bandwidth utilisation	Maximum	Low	Maximum
Dynamic network	Average	Good	Good
Packet failure Effect	Latency	Low	-
Synchronisation	Mandatory	-	Not-Mandatory

and millimeter-wave (60 GHz) frequencies. It highlights the challenges addressed in the literature that still exist today. The authors noticed a lack of research on the 24 GHz ISM band in WBAN. This thesis aims to fill that gap by exploring how radio signals travel on the body at 24 GHz using both single and multiple antennas. The choice of 24 GHz is because it offers the potential for high data rates, less interference, smaller devices, and uses unlicensed frequency bands. The study uses measurements and simulations to analyse how well a communication protocol (CSMA) works for WBAN at 24 GHz.

References

- [1] L. Akhoondzadeh-asl, P.S. Hall, Y.I. Nechayev, and I. Khan. "Depolarization in onbody communication channels at 2.45 GHz." *IEEE Transactions on Antennas and Propagation*, 61(2):882–889, 2013.
- [2] L. Akhoondzadeh-asl, Y.I. Nechayev, P.S. Hall, and C.C. Constantinou. "Parasitic array antenna with enhanced surface wave launching for on-body communications." *IEEE Transactions on Antennas and Propagation*, 61(4):1976–1985, 2013.
- [3] A. Alomainy, Y. Hao, A. Owadally, C.G. Parini, Y.I. Nechayev, C.C. Constantinou, and P.S. Hall. "Statistical analysis and performance evaluation for on-body radio propagation with microstrip patch antennas." *IEEE Transactions on Antennas and Propagation*, 55(1):245–248, 2007.
- [4] S.L. Cotton, G.A. Conway, and W.G. Scanlon. "A time domain approach to the analysis and modeling of on-body propagation characteristics using synchronized measurements at 2.45 GHz." *IEEE Transactions on Antennas and Propagation*, 57(4):943–955, 2009.
- [5] S.L. Cotton and W.G. Scanlon. "Characterization and modelling of the indoor radio channel at 868 MHz for a mobile bodyworn wireless personal area network." *IEEE Antennas and Wireless Propagation Letters*, 6:51–55, 2007.
- [6] S.L. Cotton and W.G. Scanlon. "Channel characterization for single- and multiple antenna wearable systems used for indoor body-to-body communications." *IEEE Transactions on Antennas and Propagation*, 57(4):980–990, 2009.

-
- [7] S.L. Cotton, W.G. Scanlon, and G.A. Conway. "Conway. Autocorrelation of signal fading in wireless body area networks." In *2nd IET Seminar on Antennas and Propagation for Body-Centric Wireless Communications*, 2009, pages 1–5.
- [8] S.L. Cotton and W.G. Scanlon. "An experimental investigation into the influence of user state and environment on fading characteristics in wireless body area networks at 2.45 GHz." *IEEE Transactions on Wireless Communications*, 8(1):6–12, 2009.
- [9] S.L. Cotton, W.G. Scanlon, and J. Guy. "The μ distribution applied to the analysis of fading in body-to-body communication channels for fire and rescue personnel." *IEEE Antennas and Wireless Propagation Letters*, 7:66–69, 2008.
- [10] A. Fort, C. Desset, P. Wambacq, and L.V. Biesen. "Indoor body-area channel model for narrowband communications." *IET Microwaves, Antennas Propagation*, 1(6):1197–1203, 2007.
- [11] Z.H. Hu, Y.I. Nechayev, P.S. Hall, C.C. Constantinou, and Y. Hao. "Measurements and statistical analysis of on-body channel fading at 2.45 GHz." *IEEE Antennas and Wireless Propagation Letters*, 6:612–615, 2007.
- [12] J. Zhang, D.B. Smith, L.W. Hanlen, D. Miniutti, D. Rodda, and B. Gilbert. "Stability of narrowband dynamic body area channel." *IEEE Antennas and Wireless Propagation Letters*, 8:53–56, 2009.
- [13] N. Katayama, K. Takizawa, T. Aoyagi, J.-I. Takada, H.-B. Li, and R. Kohno. "Channel model on various frequency bands for wearable body area network." In *First International Symposium on Applied Sciences on Biomedical and Communication Technologies*, 2008, pages 1–5.
- [14] I. Khan, Y.I. Nechayev, and P.S. Hall. "On-body diversity channel characterization." *IEEE Transactions on Antennas and Propagation*, 58(2):573–580, 2010.

-
- [15] I. Khan, Y.I. Nechayev, and P.S. Hall. "Second-order statistics of measured on-body diversity channels." *Microwave and Optical Technology Letters*, 51(10):2335–2337, 2009.
- [16] Y.I. Nechayev, P.S. Hall, C. Constantinou, Y. Hao, A. Alomainy, R. Dubrovka, and C.G. Parini. "On-body path gain variations with changing body posture and antenna position." *IEEE Antennas and Propagation Society International Symposium*, volume 1B, pages 731–734 vol. 1B, 2005.
- [17] K. Tai, H. Harada, and R. Kohno. "Channel modelling and signalling of medical implanted communication systems and a step to medical ICT." In *16th IST Mobile and Wireless Communications Summit*, 2007, pages 1–5.
- [18] K. Takizawa, T. Aoyagi, K. Hamaguchi, and R. Kohno. "Performance evaluation of wireless communications through capsule endoscope." In *Annual International Conference of the IEEE Engineering in Medicine and Biology Society*, EMBC 2009, pages 6897–6900.
- [19] B. Zhen, M. Kim, J. i. Takada, and R. Kohno. "Characterization and modelling of dynamic on-body propagation at 4.5 GHz." *IEEE Antennas and Wireless Propagation Letters*, 8:1263–1267, 2009.
- [20] P.S. Hall, Y. Hao, Y.I. Nechayev, A. Alomainy, C.C. Constantinou, C. Parini, M.R. Kamarudin, T.Z. Salim, D.T.M. Hee, R. Dubrovka, A.S. Owadally, W. Song, A. Serra, P. Nepa, M. Gallo, and M. Bozzetti. "Antennas and propagation for on-body communication systems." *IEEE Antennas and Propagation Magazine*, 49(3):41–58, 2007.
- [21] A. Alomainy, Y. Hao, and D.M. Davenport. "Parametric study of wearable antennas with varying distances from the body and different on-body positions." In *IET Seminar on Antennas and Propagation for Body-Centric Wireless Communications*, 2007, pages 84–89.
- [22] M. Klemm, I.Z. Kovcs, G.F. Pedersen, and G. Troster. "Novel small-size directional antenna for UWB WBAN/WPAN applications." *IEEE Transactions on Antennas and Propagation*, 53(12):3884–3896, 2005.

-
- [23] T. See and Z.-N. Chen. "Experimental characterization of UWB antennas for on-body communications." *IEEE Transactions on Antennas and Propagation*, 57(4):866–874, 2009.
- [24] A. Alomainy, Y. Hao, C.G. Parini, and P.S. Hall. "Comparison between two different antennas for UWB on-body propagation measurements." *IEEE Antennas and Wireless Propagation Letters*, 4:31–34, 2005.
- [25] N. Chahat, M. Zhadobov, R. Sauleau, and K. Ito. "A compact UWB antenna for on-body applications." *IEEE Transactions on Antennas and Propagation*, 59(4):1123–1131, 2011.
- [26] A. Alomainy, A. Sani, A. Rahman, J.G. Santas, and Y. Hao. "Transient characteristics of wearable antennas and radio propagation channels for ultrawideband body-centric wireless communications." *IEEE Transactions on Antennas and Propagation*, 57(4):875–884, 2009.
- [27] Q.H. Abbasi, A. Sani, A. Alomainy, and Y. Hao. "Arm movements affect on ultra-wideband on-body propagation channels and radio systems." In *Loughborough Antennas Propagation Conference*, 2009, pages 261–264.
- [28] A. Alomainy, Y. Hao, X. Hu, C.G. Parini, and P.S. Hall. "UWB on-body radio propagation and system modelling for wireless body-centric networks." *IEEE Proceedings Communications*, 153(1):107–114, 2006.
- [29] G. A. Deschamps, "Microstrip microwave antennas", 3rd *USAF Symposium on Antennas*, 1953.
- [30] I. J. Bahl and P. Bhartia, *Microstrip Antennas*, Artech House, 1980.
- [31] J. R. James, P. S. Hall and C. Wood, *Microstrip antenna theory and Design*, Peter Peregrinus, 1981.
- [32] J. R. James and P. S. Hall (Editors), *Handbook of Microstrip Antennas*, Peter Peregrinus, 1989.
- [33] D. M. Pozar, "Microstrip Antennas," *Proceedings of the IEEE*, Vol. 80, No. 1, pp. 79–91, January 1992.

-
- [34] Jean-Francois Zurcher and F. E. Gardiol, *Broadband Patch Antennas*, Artech House, 1995.
- [35] K. F. Lee and W. Chen (Editors), *Advances in Microstrip and Printed Antennas*, Wiley Interscience, 1997.
- [36] K. L. Wong, *Design of Nonplanar Microstrip Antennas and Transmission Lines*, Wiley Interscience, 1999.
- [37] G. Garg, P. Bhartia, I. Bahl, A. Ittipiboon, *Microstrip Antenna Design Handbook*, Artech House, 2002.
- [38] Two-port Network. http://en.wikipedia.org/wiki/Two-port_network. [Online; accessed 20-December-2013].
- [39] S.L. Cotton, A. McKernan, and W.G. Scanlon. "Received signal characteristics of outdoor body-to-body communications channels at 2.45 GHz." In *Loughborough Antennas and Propagation Conference (LAPC)*, pages 1–4, 2011.
- [40] C. Icheln, J. Ollikainen, and P. Vainikainen. "Reducing the influence of feed cables on small antenna measurements." *Electronics Letters*, 35(15):1212–1214, 1999.
- [41] P.J. Massey and K.R. Boyle. "Controlling the effects of feed cable in small antenna measurements." In *Twelfth International Conference on Antennas and Propagation*, 2003, volume 2, pages 561–564.
- [42] I. Kovacs, G.F. Pedersen, P. Eggers, and K. Olesen. "Ultra-wideband radio propagation in body area network scenarios". *IEEE Eighth International Symposium on Spread Spectrum Techniques and Applications*, 2004, pages 102–106.
- [43] P.A. Catherwood and W.G. Scanlon. "Measurement errors introduced by the use of co-axial cabling in the assessment of wearable antenna performance in off-body channels". In *Proceedings of the 5th European Conference on Antennas and Propagation (EUCAP)*, 2011, pages 3787–3791.

-
- [44] S. Dusara. "Radio-over-fibre systems for body-centric communication measurements." PhD thesis, University of Birmingham, 2011.
- [45] N.E. Roberts, S. Oh, and D.D. Wentzloff. "Exploiting channel periodicity in body sensor networks". *IEEE Journal on Emerging and Selected Topics in Circuits and Systems*, 2(1):4–13, 2012.
- [46] A.A. Goulianos and S. Stavrou. "UWB path arrival times in body area networks". *IEEE Antennas and Wireless Propagation Letters*, 6:223–226, 2007.
- [47] A.F. Molisch, D. Cassioli, C.-C. Chong, S. Emami, A. Fort, B. Kannan, J. Karedal, J. Kunisch, H.G. Schantz, K. Siwiak, and M.Z. Win. "A comprehensive standardized model for ultrawideband propagation channels". *IEEE Transactions on Antennas and Propagation*, 54(11):3151–3166, 2006.
- [48] A. Sani, A. Alomainy, G. Palikaras, Y. Nechayev, Y. Hao, C. Parini, and P.S. Hall. "Experimental characterization of UWB on-body radio channel in indoor environment considering different antennas". *IEEE Transactions on Antennas and Propagation*, 58(1):238–241, 2010.
- [49] S. Van Roy, C. Oestges, F. Horlin, and P. De Doncker. "On-body propagation velocity estimation using ultra-wideband frequency-domain spatial correlation analyses". *Electronics Letters*, 43(25):1405–1406, 2007.
- [50] S. Van Roy, C. Oestges, F. Horlin, and P. De Doncker. "A comprehensive channel model for UWB multisensor multiantenna body area networks". *IEEE Transactions on Antennas and Propagation*, 58(1):163–170, 2010.
- [51] T. Zasowski, G. Meyer, F. Althaus, and A. Wittneben. "UWB signal propagation at the human head". *IEEE Transactions on Microwave Theory and Techniques*, 54(4):1836–1845, 2006.
- [52] T. Zasowski and A. Wittneben. "Performance of UWB receivers with partial CSI using a simple body area network channel model." *IEEE Journal on Selected Areas in Communications*, 27(1):17–26, 2009.

-
- [53] M.U. Rehman, Y. Gao, X. Chen, C.G. Parini, Z. Ying, T. Bolin, and J. W. Zweers. "On-body Bluetooth link budget: Effects of surrounding objects and role of surface waves." In *Loughborough Antennas and Propagation Conference*, 2008, pages 97–100.
- [54] Y.I. Nechayev, P.S. Hall, and Z.H. Hu. "Characterization of narrowband communication channels on the human body at 2.45 GHz". *IET Microwaves, Antennas Propagation*, 4(6):722–732, 2010.
- [55] G.A. Conway and W.G. Scanlon. "Antennas for over-body-surface communication at 2.45 GHz." *IEEE Transactions on Antennas and Propagation*, 57(4):844–855, 2009.
- [56] A.R. Chandran, G.A. Conway, and W.G. Scanlon. "Pattern switching compact patch antenna for on-body and off-body communications at 2.45 GHz". In *3rd European Conference on Antennas and Propagation*, 2009, pages 2055–2057, 2009.
- [57] D. Psychoudakis and J.L. Volakis. "Conformal asymmetric meandered flare (AMF) antenna for body-worn applications". *IEEE Antennas and Wireless Propagation Letters*, 8:931–934, 2009.
- [58] Y.-J. Ren, C.-P. Lai, P.-H. Chen, and R.M. Narayanan. "Compact ultra-wideband UHF array antenna for through-wall radar applications". *IEEE Antennas and Wireless Propagation Letters*, 8:1302–1305, 2009.
- [59] M.R. Kamarudin and P.S. Hall. "Switched beam antenna array with parasitic elements". *Progress In Electromagnetics Research B*, 13:187–201, 2009.
- [60] H.G. Schantz and L. Fullerton. "The diamond dipole: a Gaussian impulse antenna." In *IEEE Antennas and Propagation Society International Symposium*, 2001, pages 100–103 vol.4.
- [61] X. Han, L. Juan, C. Cui, and Y. Lin. "UWB dual-polarized Vivaldi antenna with high gain." *International Conference on Microwave and Millimeter Wave Technology (ICMMT)*, 2012, volume 3, pages 1–4.

-
- [62] L. Abdelghani, T.A. Denidni, and M. Nedit. "Design of a new ultra-wideband 4×4 Butler matrix for beamforming antenna applications." *IEEE Antennas and Propagation Society International Symposium (APSURSI)*, 2012, pages 1–2.
- [63] C. Hertleer, A. Tronquo, H. Rogier, L. Vallozzi, and L. Van Langenhove. "Aperture-coupled patch antenna for integration into wearable textile systems". *IEEE Antennas and Wireless Propagation Letters*, 6:392–395, 2007.
- [64] I. Locher, M. Klemm, T. Kirstein, and G. Troster. "Design and characterization of purely textile patch antennas". *IEEE Transactions on Advanced Packaging*, 29(4):777–788, 2006.
- [65] D.L. Paul, H. Giddens, M.G. Paterson, G.S. Hilton, and J.P. McGeehan. "Impact of body and clothing on a wearable textile dual-band antenna at digital television and wireless communications bands". *IEEE Transactions on Antennas and Propagation*, 61(4):2188–2194, 2013.
- [66] M.L. Scarpello, I. Kazani, C. Hertleer, H. Rogier, and D. Vande Ginste. "Stability and efficiency of screen-printed wearable and washable antennas". *IEEE Antennas and Wireless Propagation Letters*, 11:838–841, 2012.
- [67] R. Moro, S. Agneessens, H. Rogier, and M. Bozzi. "Wearable textile antenna in substrate integrated waveguide technology". *Electronics Letters*, 48(16):985–987, 2012.
- [68] A. Chauraya, W.G. Whittow, J.C. Vardaxoglou, Y. Li, R. Torah, K. Yang, S. Beeby, and J. Tudor. "Inkjet printed dipole antennas on textiles for wearable communications". *IET Microwaves, Antennas Propagation*, 7(9), 2013.
- [69] Q. Bai and R. Langley. "Crumpling of PIFA textile antenna". *IEEE Transactions on Antennas and Propagation*, 60(1):63–70, 2012.
- [70] T. Maleszka and P. Kabacik. "Bandwidth properties of an embroidered loop antenna for wearable applications". *European Wireless Technology Conference (EuWIT)*, 2010, pages 89–92.

-
- [71] J.A. Dobbins, A.W. Chu, P.W. Fink, T.F. Kennedy, G.Y. Lin, M.A. Khayat, and R.C. Scully. "Fabric equiangular spiral antenna". *IEEE Antennas and Propagation Society International Symposium*, 2006, pages 2113–2116.
- [72] S. Zhu and R. Langley. "Dual-band wearable textile antenna on an EBG substrate". *IEEE Transactions on Antennas and Propagation*, 57(4):926–935, 2009.
- [73] Yang, X., Matthaiou, M., Yang, J., Wen, C. K., Gao, F., Jin, S. "Hardware-constrained millimeter-wave systems for 5G: Challenges, opportunities, and solutions". *IEEE Communications Magazine*, 57(1), 44-50, 2019.
- [74] Larew, S. G., Thomas, T. A., Cudak, M., Ghosh, A. "Air interface design and ray tracing study for 5G millimeter wave communications". *IEEE Globecom Workshops (GC Wkshps)*, December 2013, pp. 117-122.
- [75] Li, Y., Luo, J., Castaneda, M. H., Vucic, N., Xu, W., Caire, G. "Analysis of Broadcast Signaling for Millimeter Wave Cell Discovery". *IEEE 86th Vehicular Technology Conference (VTC-Fall)*, 2017.
- [76] T. S. Rappaport et al., "Millimeter Wave Wireless Communications," Pearson Education, 2014.
- [77] T. Nitsche et al., "Steering with Eyes Closed: mm-Wave Beam Steering without In-Band Measurement," *Proc. IEEE INFOCOM*, 2015, pp. 2416–24.
- [78] Chen, M., Gonzalez, S., Vasilakos, A., Cao, H., Leung, V. C. "Body area networks: A survey." *Mobile networks and applications*, 16(2), 171-193, 2011.
- [79] Gopalan, S. A., Park, J. T. "Energy-efficient MAC protocols for wireless body area networks: Survey." In *International Congress on Ultra Modern Telecommunications and Control Systems*, October 2010, pp. 739-744.
- [80] Busch, C., Magdon-Ismail, M., Sivrikaya, F., Yener, B. "Contention-free MAC protocols for wireless sensor networks." In *International Symposium on Distributed Computing*. Springer, Berlin, Heidelberg, October 2004, pp. 245-259.

-
- [81] Barakah, D. M., Ammad-uddin, M. "A survey of challenges and applications of wireless body area network (WBAN) and role of a virtual doctor server in existing architecture." In *Third International Conference on Intelligent Systems Modelling and Simulation*, 2012, pp. 214-219.
- [82] Ghamari, M., Janko, B., Sherratt, R. S., Harwin, W., Piechockic, R., Soltanpur, C. "A survey on wireless body area networks for healthcare systems in residential environments." *Sensors*, 16(6), 831, 2016.
- [83] Chakraborty, C., Gupta, B., Ghosh, S. K. "A review on telemedicine-based WBAN framework for patient monitoring." *Telemedicine and e-Health*, 19(8), 619-626, 2013.
- [84] Antonescu, B., Basagni, S. "Wireless body area networks: challenges, trends and emerging technologies." In *Proceedings of the 8th international conference on body area networks*, September 2013, pp. 1-7.
- [85] Estevez, C. I., Wei, J., Kailas, A., Fuentealba, D., Chang, G. K. "Very-high-throughput millimeter-wave system oriented for health monitoring applications." In *IEEE 13th International Conference on e-Health Networking, Applications and Services*, 2011, pp. 229-232.
- [86] Cavallari R, Martelli F, Rosini R, Buratti C, Verdone R, "A survey on Wireless Body Area Networks: technologies and design challenges." *IEEE Commun Surv Tutor* 3:1–23, 2010.
- [87] Ullah S, Kwak KS, "An ultra low-power and traffic-Adaptive Medium Access Control protocol for wireless body area network." *J Med Syst* 36(3):1021–1030, 2012.
- [88] Isikman AO, Cazalon L, Chen F, Li P, "Body area networks." *J Mob Netw Appl* 16(2):171–193, 2011.
- [89] Wang S-L, Chen YL, Kuo AM-H, Chen H-M, Shiu YS "Design and evaluation of a cloud-based Mobile Health Information Recommendation system on wireless sensor networks." *Comput Electr Eng* 49:221–235, 2016.

-
- [90] Gopalan SA, Kim DH, Nah JW, Park JT, "A survey on power-efficient MAC protocols for wireless body area networks. In: Broadband network and multimedia technology (IC-BNMT)", 3rd *IEEE International Conference on*, Beijing, China, 2010, pp. 1230–1234.
- [91] Marinkovic S, Spagnol C, Popovici E "Energy-efficient TDMA-based MAC protocol for Wireless Body Area Networks." In 3rd *international conference on sensor technologies and applications*, 2009, pp 604–609.
- [92] Lin L, Kumar A, "An energy-efficient MAC protocol for mobile in vivo body sensor networks." In 3rd *International Conference on ubiquitous and future networks (ICUFN)*, 2011, pp 95–100.
- [93] Charf F, Bouyahi M, 1 Laboratoire, "Performance evaluation of beacon-enabled IEEE 802.15.4 under NS2." *Int J Distrib Parallel Syst (IJDPSS)* 3(2):67–79, 2012.
- [94] Al Ameen M, Ullah N, Chowdhury MS, Islam SMR, Kwak K, "A power efficient MAC protocol for Wireless Body Area Networks." *EURASIP J Wirel Commun Netw* (1):33, 2012.
- [95] Lin L, Yang C, Wong KJ, Yan H, Shen J, Phee SJ, "An energy efficient MAC protocol for multi-hop swallowable body sensor networks." *Sens (Basel, Switz)* 14(10):19457–19476, 2014.
- [96] Timmons NF, Scanlon WG, "An adaptive energy-efficient MAC protocol for the medical body area network." In 1st *international conference on wireless communication, vehicular technology, information theory and aerospace electronic systems technology*, 2009, pp 587–593.
- [97] Calhan A, "A Non-Preemptive priority scheduling algorithm for improving priority data transmission delay in wireless body area networks." *Adhoc Sens Wireless Netw* 34:59–75, 2016.
- [98] Wang R, Wang H, Roman HE, Wang Y, Xu D, "A cooperative Medium Access Control protocol for mobile clusters in Wireless Body Area Networks."

-
- In *1st international symposium on future information and communication technologies for ubiquitous healthcare (Ubi-HealthTech)*, 2013, pp 1–4.
- [99] Ullah S, Mohaisen M, Alnuem MA, "A review of IEEE 802.15.6 MAC, PHY, and security specifications." *Int J Distrib Sens Netw* 2013:1–12, 2013.
- [100] Rashwand S, Mišić J, "Effects of access phases lengths on the performance of IEEE 802.15.6 CSMA/CA." *Comput-Netw* 56(12):2832–2846, 2012.
- [101] Xia F, Hao R, Li J, Xiong N, Yang LT, Zhang Y, "Adaptive GTS allocation in IEEE 802.15.4 for real-time wireless sensor networks." *J Syst Archit* 59(10):1231–1242, 2013.
- [102] Ullah F, Abdullah AH, Kaiwartya O, Lloret J, Arshad MM, "EETP-MAC: energy efficient traffic prioritization for medium access control in wireless body area networks." *Telecommun Syst* 1–23, 2017.
- [103] Zhan Y, Xia Y, Anwar M, "GTS size adaptation algorithm for IEEE 802.15.4 wireless networks." *Ad Hoc Netw* 37:486–498, 2016.
- [104] Zhang Y, Dolmans G, "A new priority-guaranteed MAC protocol for emerging body area networks." In *5th international conference on wireless and mobile communications*, 2009, pp 140–145.
- [105] M.X. Gong, D. Akhmetov, R. Want, S. Mao, "Directional CSMA/CA protocol with spatial reuse for mmWave wireless networks", in *IEEE GLOBECOM*, 2010, pp.1–5.
- [106] K. Chandra, R.V. Prasad, B. Quang, I. Niemegeers, "CogCell: cognitive interplay between 60 GHz picocells and 2.4/5 GHz hotspots in the 5G era," *IEEE Commun. Mag.* 53 (7), 118–125, 2015.
- [107] S. Singh, F. Ziliotto, U. Madhow, E. Belding, M. Rodwell, "Blockage and directivity in 60 GHz wireless personal area networks: from cross-layer model to multihop mac design," *IEEE J. Sel. Areas Commun.* 27 (8), 1400–1413, 2012

-
- [108] I.K. Son, S. Mao, M.X. Gong, Y. Li, "On frame-based scheduling for directional mmWaveWPANs," in *Proceedings IEEE INFOCOM*, 2012, pp. 2149–2157.
- [109] Zhu, X., Doufexi, A., Kocak, T. "On the performance of IEEE 802.15.3c millimeter-wave WPANs: PHY and MAC." In *IEEE Wireless Advanced*, 2010, pp. 1-6.
- [110] Chen, Q., Tang, J., Wong, D. T. C., Peng, X., Zhang, Y. "Directional cooperative MAC protocol design and performance analysis for IEEE 802.11 ad WLANs." *IEEE Transactions on Vehicular Technology*, 62(6), 2667-2677, 2013.
- [111] Venkatachalam, I., Palaniappan, S., Ameer John, S. "Distributed directional cooperative MAC (DD-CoopMAC) protocol for improving VBR throughput in IEEE 802.11 ad WLAN." *Sādhanā*, 45(1), 245, 2020.
- [112] Yao, X. W., Jornet, J. M. "TAB-MAC: Assisted beamforming MAC protocol for Terahertz communication networks." *Nano Communication Networks*, 9, 36-42,(2016).
- [113] A. Maltsev et al, "Channel models for 60 GHz WLAN systems," *IEEE 802.11 TGad document: IEEE 802.11-09/0334r8*, 2010.
- [114] M. Jacob, S. Priebe, A. Maltsev, A. Lomayev, V. Erceg, and T. Kurner, "A ray tracing based stochastic human blockage model for the IEEE 802.11 ad 60 GHz channel model," in *Antennas and Propagation (EUCAP)*, Proceedings of the 5th European Conference, 2011, pp. 3084–3088.
- [115] M. Fakharzadeh, J. Ahmadi-Shokouh, B. Biglarbegian, M. NezhadAhmadi, and S. Safavi-Naeini, "The effect of human body on indoor radio wave propagation at 57–64 GHz," in *Antennas and Propagation Society International Symposium, APSURSI'09*, 2009, pp. 1–4.
- [116] K. Dong, X. Liao, and S. Zhu, "Link blockage analysis for indoor 60 GHz radio systems," *Electronics letters*, vol. 48, no. 23, pp. 1506–1508, 2012.

-
- [117] M. Jacob, S. Priebe, T. Kurner, M. Peter, M. Wisotzki, R. Felbecker, and W. Keusgen, “Fundamental analyses of 60 GHz human blockage,” in *Antennas and Propagation (EuCAP)*, 7th European Conference, 2013, pp. 117–121.
- [118] A. Pellegrini, A. Brizzi, L. Zhang, K. Ali, Y. Hao, X. Wu, C. Constantinou, Y. Nechayev, P. Hall, N. Chahat, M. Zhadobov, and R. Sauleau, “Antennas and propagation for body-centric wireless communications at millimeter-wave frequencies: A review,” *IEEE Antennas Propag. Mag.*, vol. 55, no. 4, pp. 262–287, August 2013.
- [119] A. Guraliuc, M. Zhadobov, G. Valerio, N. Chahat, and R. Sauleau, “Effect of textile on the propagation along the body at 60 GHz,” *IEEE Trans. Antennas Propag.*, vol. 62, no. 3, pp. 1489–1494, March 2014.
- [120] A. Guraliuc, M. Zhadobov, G. Valerio, and R. Sauleau, “Enhancement of on-body propagation at 60 GHz using electro textiles,” *IEEE Antennas Wireless Propag. Lett.*, vol. 13, pp. 603–606, 2014.
- [121] A. Sard, Y. Hao, Y. Zhao, S.-I. Lee, and G.-Z. Yang, “Subjectspecific analysis of the on-body radio propagation channel adopting a parallel FDTD code,” in *Antennas and Propagation (EuCAP)*, IEEE Proceedings of the Fourth European Conference. , 2010, pp. 1–3.

Chapter 3

24 GHz Flexible antennas for On-body communication

3.1 introduction

Lately, wireless communication networks have been driven towards the mm-wave frequencies due to a large amount of available bandwidth, and the capability to achieve high throughput. Therefore, mm-wave frequencies have attracted the wireless body area network community as it offers great potential to further improve health care and remote sensing application [1] - [3]. The mm-wave spectrum provides plenty of advantages like reduced interference due to uncongested bandwidth, compact devices, and large data rates [4]. Recently, A 24 GHz ISM band Yagi Uda antenna has been developed on a flexible substrate using inkjet printing [5]. Moreover, a 60 GHz wearable end-fire antenna has been proposed for on-body communication [6]. However, these wearable antennas have high backward radiation which causes a potential hazard to the human body. Millimeter waves have very short wavelengths, therefore penetration depth of mm-wave frequencies is restricted to 1 mm. Due to the very close proximity of human skin tissue with the antenna, the performance of the antenna is further reduced [7]. To overcome this challenge, good isolation is required between the human skin and the

antenna. Electromagnetic bandgap (EBG) structures are widely used to suppress the surface waves and back lobe radiations of the antenna [18]. A square-shaped EBG printed on textile material has been proposed for a 26 GHz antenna which enhances the gain by 19% [8] - [9].

The first part of this chapter reports a design published by the author [10]. A low profile antenna integrated with a dual split square ring EBG structure with the thickness of $0.02\lambda_0$ is presented. The presented antenna is a slotted bow-tie, backed by an array of 5×5 cell EBG structure demonstrating the required phase reflection at 24 GHz, which substantially reduces the backward radiation of the antenna.

The Second antenna introduced in this chapter is a compact circular antenna for on-body WBAN applications in the 24 GHz ISM band. The antenna is made from a vinyl polymer-based PTFE material called Rogers 5880 and uses radial stubs and meandering slits to increase its electrical length without increasing its size. This makes the antenna more compact than other antennas currently available. The dimensions of the proposed antenna are $16.612 \times 11.228 \times 0.127$ mm³. To test the antenna's conformability, it was tested under different curvature radii, resulting in only 0.8% frequency detuning. This is due to the use of meandering slits, which reduce the antenna's mechanical spring constant, making it more flexible. All simulated results were calculated using the CST Microwave Studio 3-D electromagnetic solver. The effects of bending on the antenna's performance were analyzed in detail to predict its on-body performance. Finally, an experimental evaluation was performed on a 29-year-old male volunteer to assess the antenna's on-body performance.

This chapter also focuses on exploring and evaluating planar end-fire array and tapered slot antenna configurations for use in mm-wave wearable applications, with the goal of identifying a design that offers good performance in terms of directional gain and radiation efficiency while being straightforward to fabricate and integrate. By using a simple planar structure, the presented end-fire array design

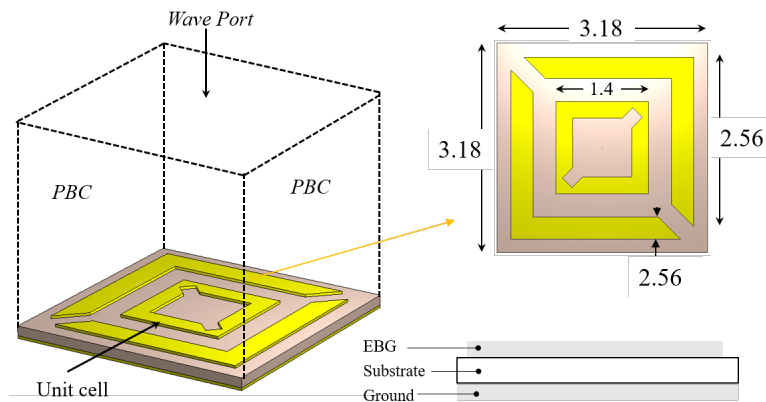


FIGURE 3.1: EBG geometry

could potentially pave the way for the development of practical and cost-effective wearable antennas for various wireless communication and sensing applications.

This chapter is organized as follows: In each section, the design and geometry of the antenna will be presented. Following that, in each subsection, the experimental and simulation results of the prototyped antenna. This will include information on radiation patterns, free space, and on-body reflection coefficient (S_{11}), as well as structural deformation analysis. Finally, the conclusions are in the last section.

3.2 EBG backed bow-tie antenna

A unit cell based on a dual split square ring resonator with an area of $3.18 \times 3.18 \text{ mm}^2$ was designed and fabricated on a Rogers 5880 dielectric substrate with a relative permittivity of 2.2 and a thickness of $127 \mu\text{m}$, with a ground plane beneath it. The proposed unit cell structure is derived from the basic rectangular split-ring resonator and is subsequently optimized for the best performance in the required frequency band. The unit cell was simulated using CST Microwave Studio, with periodic boundary conditions (PBCs) applied to accurately model its behavior. The design was optimized to achieve the desired phase reflection response at 24.125 GHz.

The proposed geometry of the outer and inner split square ring resonator, with coupling gaps on two corners, was found to provide a 0° phase shift from the

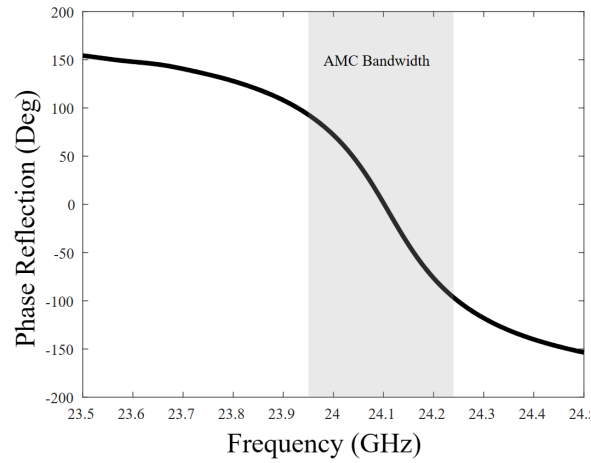


FIGURE 3.2: Phase reflection diagram

reflected wave, as shown in Fig.3.2. This behaviour allows the unit cell to function as an artificial magnetic conductor (AMC), which can reflect electromagnetic waves with high efficiency and low loss. The AMC effect arises due to the resonant coupling between the two split ring resonators, which causes a current distribution that mimics that of a magnetic conductor.

3.2.1 Antenna Design and Integration with EBG

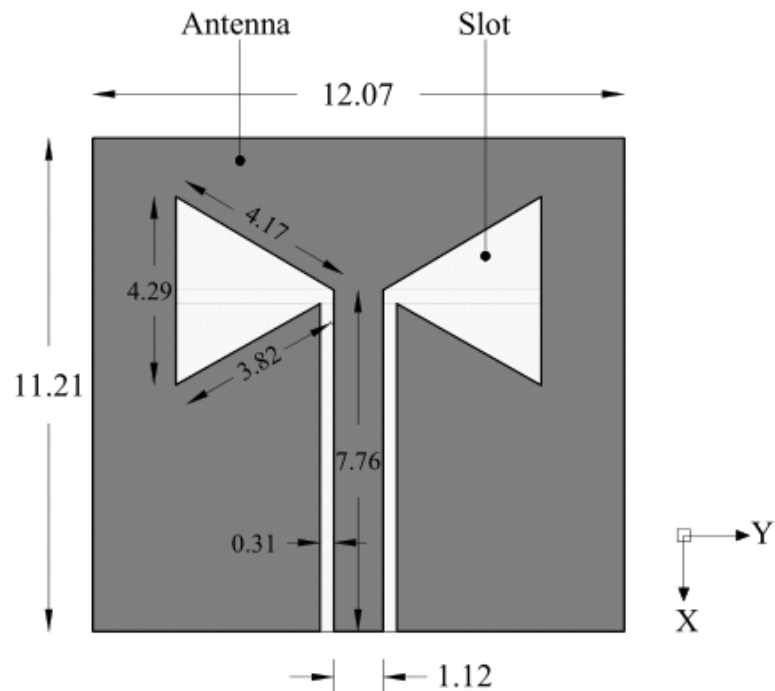


FIGURE 3.3: Bow-tie slot antenna geometry

The co-planar waveguide (CPW)-fed bow-tie slot antenna was fabricated with dimensions and geometry shown in Fig.3.3. The antenna is designed to have a single metallization layer, making its construction straightforward. For ungrounded CPW feeding, the antenna is fed directly without any ground plane. However, when the electromagnetic bandgap (EBG) array is attached underneath the antenna, grounded CPW feeding is used because the EBG has a ground plane. To accurately model and simulate the full EBG-backed antenna structure, the time-domain solver of CST studio was used with a 50Ω SMA connector included in the model. The inclusion of the SMA connector improves the comparison of simulation and measurement results. The chemical etching technique was employed in the prototyping and fabrication of the antenna. The resultant antenna has dimensions of $16.19 \times 16.19 \times 0.254 \text{ mm}^3$, and its configuration is shown in Fig.3.4. The

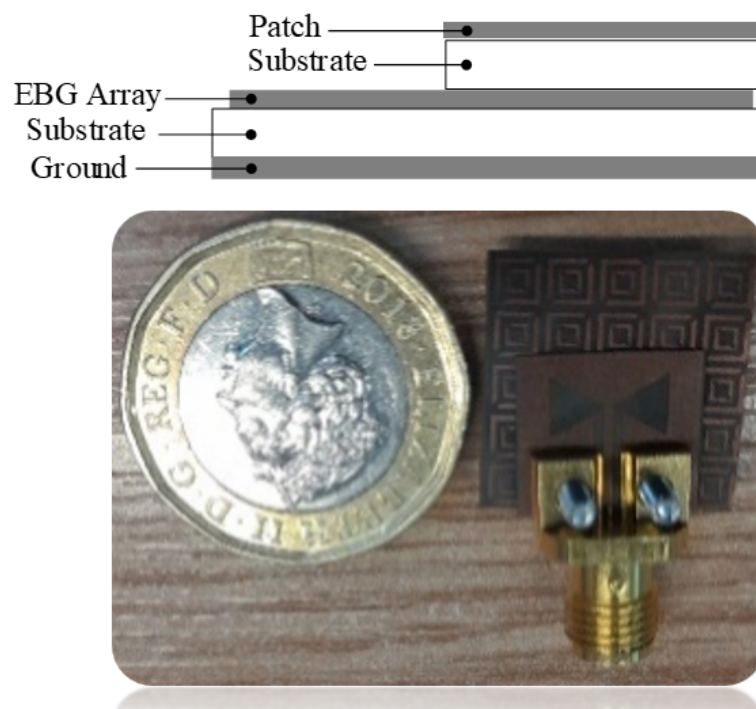


FIGURE 3.4: Integration of EBG with antenna

antenna has an edge mount integration with a connector and no air gap between the antenna and EBG. This configuration improves its suitability for wearing on the surface of the human body and facilitates integration with the connector.

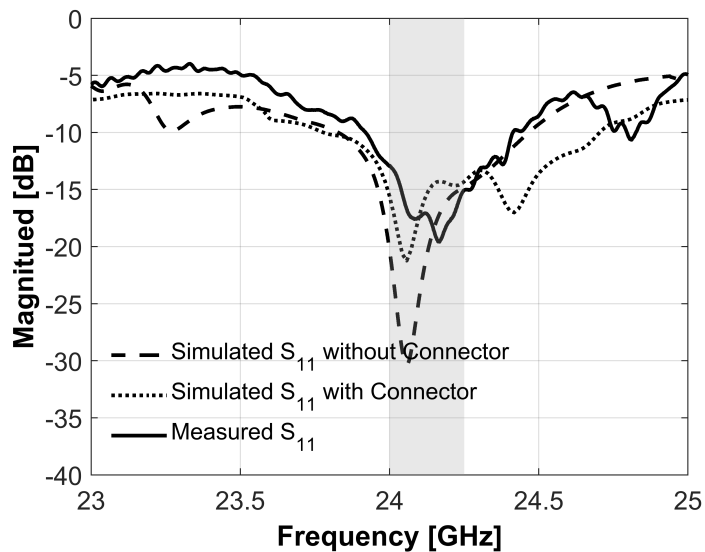


FIGURE 3.5: Return loss of simulated EBG backed antenna (Fig. 3.4) with and without connector and measured S_{11}

3.2.2 Free Space performance Evaluation

To evaluate the performance of the EBG-backed antenna, in-house testing was carried out, and the measured reflection parameters were compared with simulation results. The measurements were performed using a 40 GHz Vector Network Analyzer (VNA) (HP 8722ES), and the comparison is shown in Fig.3.5, which indicates the effect of the SMA connector. The S_{11} values of the EBG-backed antenna are less than -10 dB in the desired frequency band, and the measured S_{11} in the ISM band (24 - 24.250 GHz) is around -17 dB.

The measured E- and H-plane radiation patterns are shown in Figs.3.6 and 3.7, with the bold solid line representing the pattern with EBG and the dashed line representing the pattern without EBG. The integration of the EBG structure with the antenna significantly reduces backward radiation by 12.2 dB at 24 GHz and 10.5 dB at 24.250 GHz, while the realized gain increases by 2.6 dB to 5.5 dBi and 2.5 dB to 4.8 dBi at 24 GHz and 24.25 GHz, respectively.

The results demonstrate the effectiveness of the EBG structure in suppressing back lobe radiations that are directed toward the human body. This is particularly important for wearable devices, where the antenna is in close proximity to the

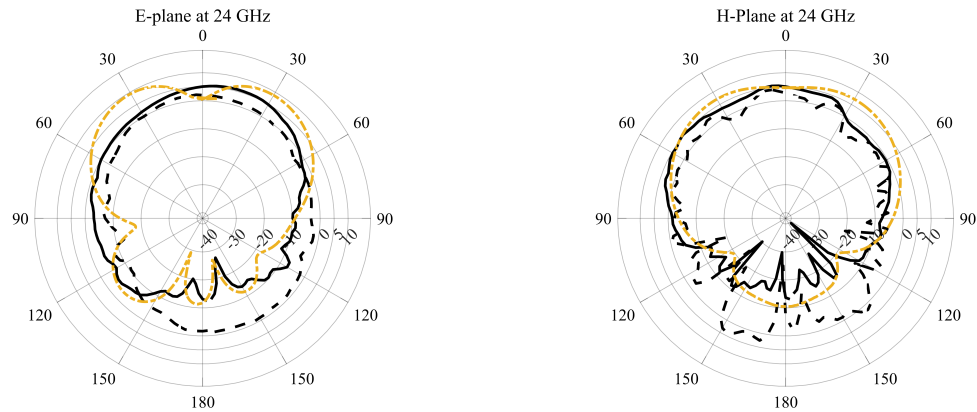


FIGURE 3.6: Radiation polar plots of bow-tie slot antenna (Fig.3.4) with EBG/AMC measured (bold solid-line), with EBG/AMC simulated (green dash-line) and without EBG/AMC measured (dash-line) at 24 GHz

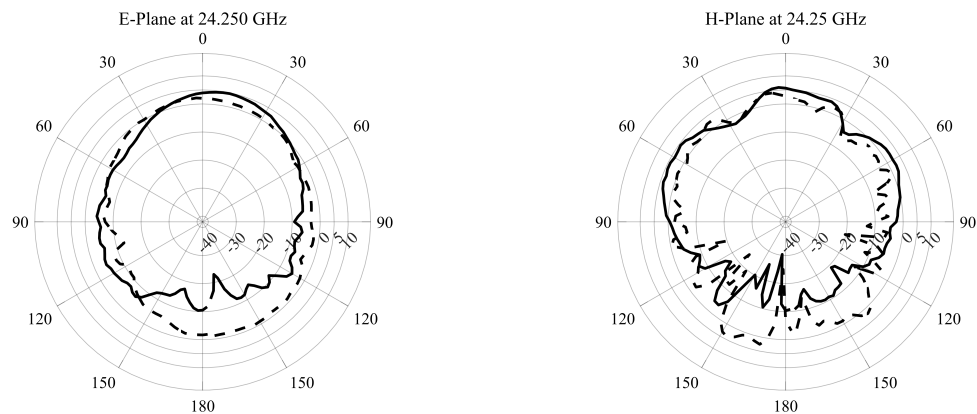


FIGURE 3.7: Measured radiation polar plots of bow-tie slot antenna (Fig.3.4) with EBG/AMC (bold solid-line) and without EBG/AMC (dash-line) at 24.250 GHz

body. The use of the EBG structure not only improves the radiation pattern and gain but also reduces interference from other devices operating in the same frequency band.

3.2.3 Structural bending analysis

Since the human body has many curved surfaces, the antenna may experience some structural deformation. Therefore, a further investigation was performed to determine the antenna's ability to withstand structural bending while retaining

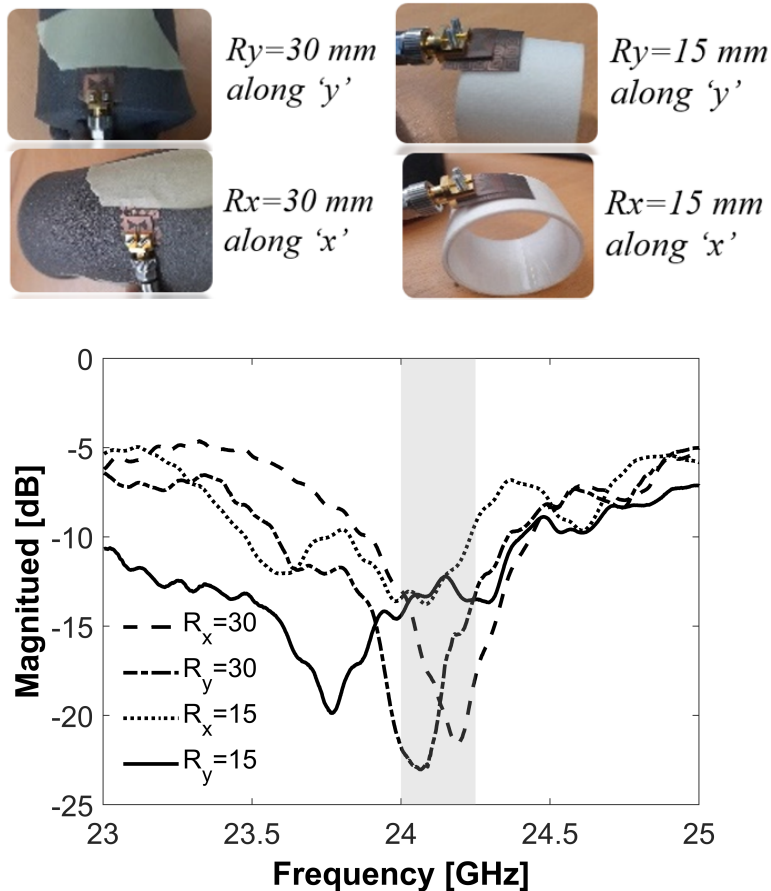


FIGURE 3.8: Measured reflection coefficients of the antenna (Fig.3.4) when bent along the X and Y-axis.

comparable reflection and radiation performance. To evaluate this, the S_{11} measurements of the antenna were taken while it was bent along the X- and Y-axis with radii of curvature of 15 and 30 mm, as shown in Fig.3.8. The antenna under consideration is bent along two different radii on a cylindrical structure, resulting in two distinct orientations. This configuration produces four distinct return loss curves. Notably, all four curves demonstrate satisfactory return loss within the desired ISM band. The results indicate a slight shift in center frequency when bent on a 30 mm radius cylinder along the X- and Y-axis. However, a larger shift is observed when bent on a 15 mm radius cylinder along the X- and Y-axis. Despite this, the S_{11} value remains better than -10 dB at 24.125 GHz.

Additionally, the radiation pattern of the EBG-backed antenna under bending scenarios (for $R_x, R_y = 15$ mm along the y-axis and x-axis) is reported in Fig.3.9, and 3.10. The results indicate that the directivity is maintained at around 1.5 dBi

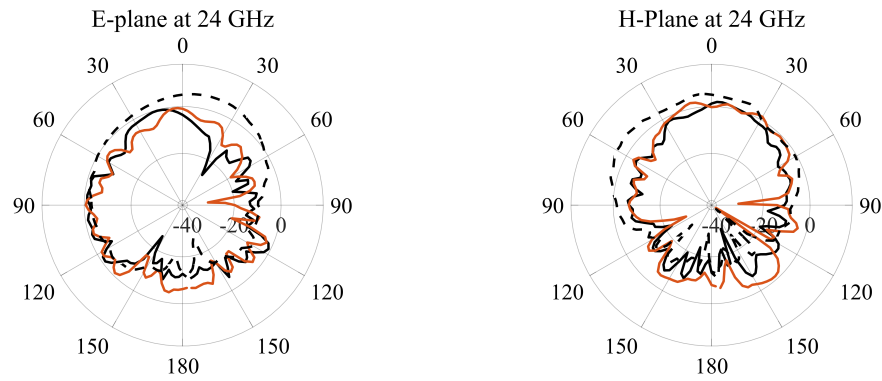


FIGURE 3.9: Measured radiation polar plots of EBG backed antenna (Fig.3.4) when bent on 15 mm radius cylinder along X-axis (black solid line), Y-axis (blue solid-line) and without bent (dash-line) at 24 GHz.

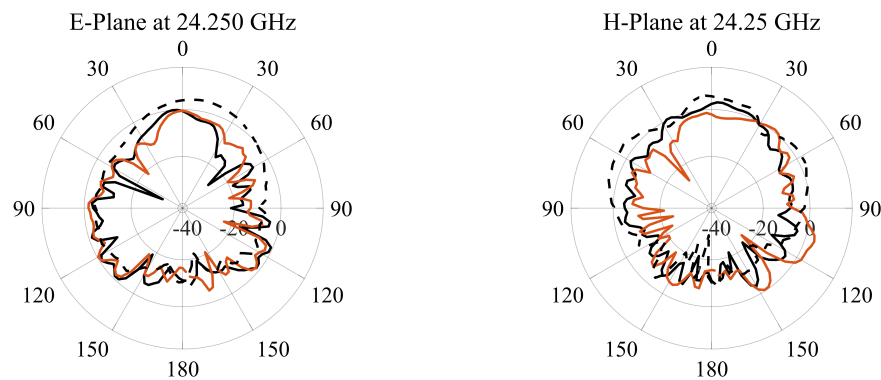


FIGURE 3.10: Measured radiation polar plots of EBG backed antenna (Fig.3.4) when bent on 15 mm radius cylinder along X-axis (black solid line), Y-axis (blue solid-line) and without bent (dash-line) at 24.250 GHz.

while separately bent at R_x and $R_y = 15$ mm, although the reflection coefficients at $R_y = 15$ mm are slightly detuned from the desired band. This suggests that the antenna can withstand some bending without significantly affecting its radiation performance. When the antenna is severely bent along a cylinder, it introduces perturbations to its radiation pattern, resulting in more ripples or distortions compared to its traditional, flat configuration. This occurs because the bending of the antenna can impact its resonant properties, leading to alterations in the distribution of electromagnetic fields around it.

3.2.4 SAR and body loading effects

To further investigate the body-loading performance of the prototype antenna, S_{11} measurements were performed on a male volunteer who was 178 cm tall and weighed 61 kg at various positions, such as chest, finger, forehead, hand, and wrist, as shown in Fig.3.11. Due to the varied dielectric constant values and capacitive behavior of different human tissues, there were differences in the S_{11} curves measured at different positions. Without an EBG, the structure was highly lossy, and significant energy was dissipated in the human tissues. All the reflection curves were detuned, even though the measured S_{11} was at < -10 dB over the desired 24 GHz ISM band, except for the wrist. The challenge of placing an antenna on the curved surface of the human body arises because, in most locations where the antenna is positioned, the entire antenna structure is not fully adhered to the skin. This is due to the connector, which is relatively large compared to the antenna structure, creating a slight gap between a small portion of the antenna and the skin. However, in the case of the wrist location, the connector is well-adjusted, and a significant portion of the antenna structure is in close contact with the skin. Consequently, the return loss is worse for the wrist skin location. After integrating the EBG structure with the antenna, as shown in Fig.3.12, the reflection response of the structure was tuned for the 24GHz ISM band for all mounting sites.

The proposed prototype covers only the 24GHz ISM band and reduces the unwanted absorption of EM energy in skin tissues outside the ISM band. The gap between the antenna aperture and the skin layers was 3 mm in both scenarios, with and without EBG. The dielectric properties of human tissue layers were obtained from the Italian National Research Council's website [11]. The ICNIRP Basic restrictions for electromagnetic field exposure from 100 kHz to 300 GHz, for averaging intervals 6 min Whole-body average SAR is 0.4 W/kg.

In CST MWS, the IEEE/IEC 62704-1 averaging method was used for SAR calculation for 1g of tissue volume, and Fig.3.13 presents the SAR distribution when the EBG was and was not attached to the antenna. The maximum SAR values were 1.93 W/kg and 28.1 W/kg at 100 mW input power, respectively. Hence,

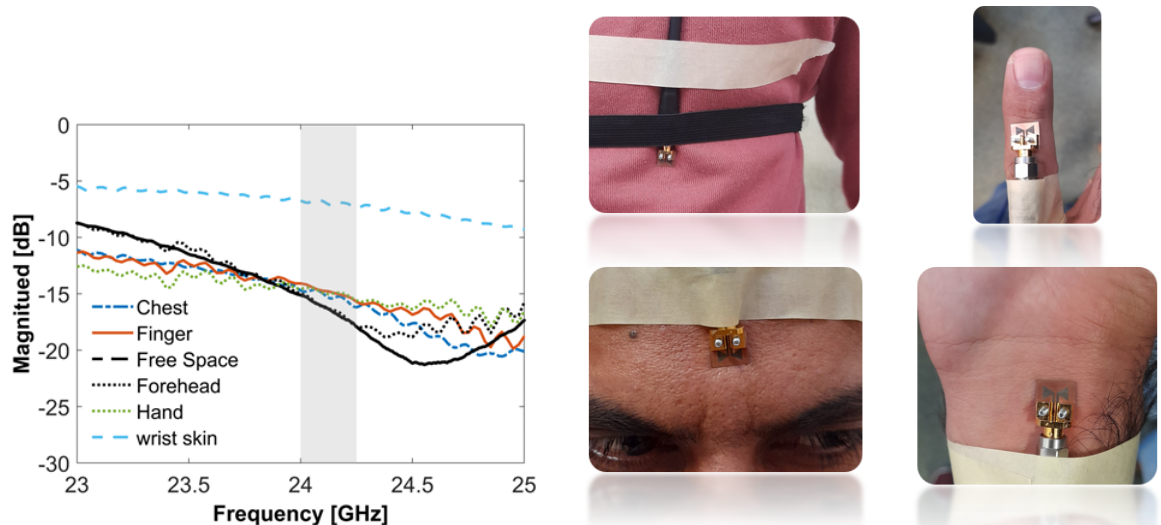


FIGURE 3.11: Measured reflection coefficients of the antenna (Fig.3.4) on the human body without EBG.

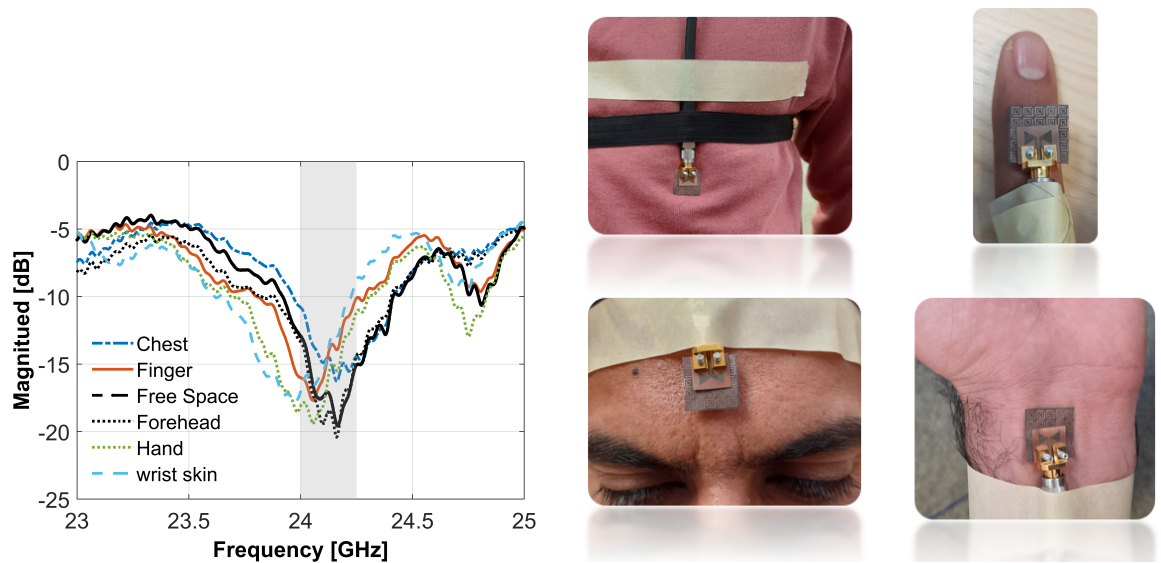


FIGURE 3.12: Measured reflection coefficients of the antenna (Fig.3.4) on human body with EBG.

the EBG shield reduced 93% of the radiation absorption rate compared to direct exposure from the antenna, which indicates that the proposed antenna structure is safe for human use.

Table 3.1 presents a comparison of different features of the proposed antenna with previously published K-band EBG-integrated antennas. The proposed antenna is the thinnest and smallest in size. This antenna covers a 24GHz ISM band when

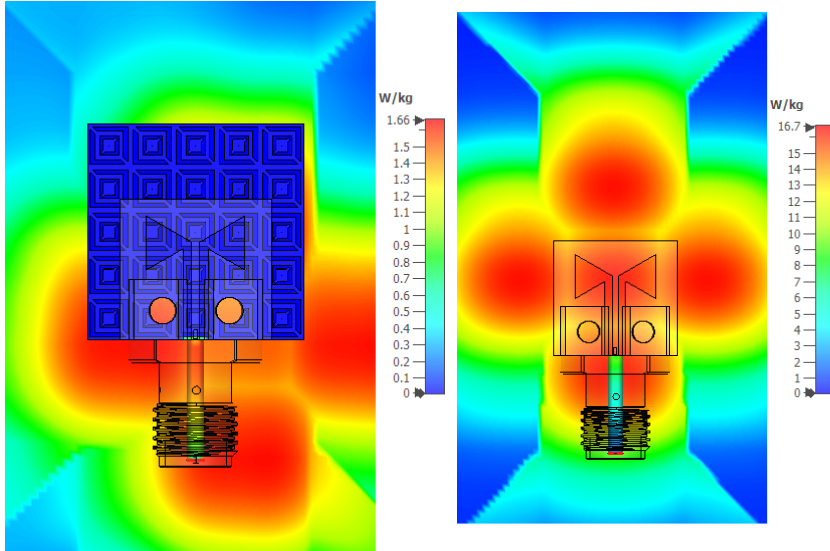


FIGURE 3.13: SAR distribution of prototype antenna (Fig.3.4) with EBG and without EBG

TABLE 3.1: Comparison with previously published K band EBG antennas

Ref	Frequ -ency GHz	Dimen - sion λ_0	Thick - ness λ_0	Gain dBi	On- body S_{11} BW%	S_{11} shift MHz/ mm	Gain dBi/ bend- ing	SAR Re- duc- tion %
This Work	24	(1.29×1.29)	0.02	5.5	2.58	80/30	1.5/15	93
[13]	26	(2.79×1.91)	0.032	8.65	2.3	400/30	NA	69.9
[14]	28	(2.67×3.14)	0.065	7.9	40	1500/30	NA	NA
[15]	24	(2.16×2.16)	0.05	6	3	400/60	*5.36/60	NA
[16]	28	(1.9×1.9)	0.14	5	**3.3	NA	NA	NA

attached directly to the skin, and shows a minimal shift in S_{11} while bending, and a significant decrease in SAR percentage.

3.3 Circular Patch antenna with radial stub

The antenna in Fig.3.14 comprised of a standard circular patch with a complete ground plane, but it was relatively larger than other antennas designed for the 24 GHz ISM band. To reduce its size, meandering slits were introduced to increase the electrical length of the antenna and lower its operating frequency, achieving the desired compactness. Meandering slits parallel to the patch feed were also added to increase the flexibility of the laminated metal and polymer stack. The final proposed design is a microstrip-based circular antenna with radial stubs on the feed, which exhibits the desired bandwidth (23.7-24.9 GHz) to operate in the 24 GHz ISM band. It has a good radiation pattern and satisfactory Front-back-ratio (FBR), making it suitable for flexible body-worn devices. The top metallic copper layer contains a modified circular patch with four meandering slits, fed using a 50Ω impedance inset feed line with radial stubs.

In order to assess the performance of the antenna, a connector (large size) is required to be attached to the antenna which is shorted with the radial stubs. As a result, the feed line was extended and optimized to achieve the necessary return loss. However, this extension of the feed line led to an increase in the size of the antenna. The final optimized antenna dimensions are $16.612 \times 11.228 \times 0.127 \text{ mm}^3$ (length, width, and thickness). The dimension and geometry of the antenna are presented in Fig.3.14. The antenna is fabricated using a polymer-based flexible substrate Roger RT/duroid 5880 with a thickness of 0.127 mm. The conductive parts are etched on copper cladding with an expected conductivity of $5.96 \times 10^7 \text{ S/m}$ and a thickness of 35 μm . The Rogers substrate has an estimated dielectric constant of 2.20 and a tangent loss of 0.0009 at the operational frequency band.

3.3.1 Return Loss evaluation

The antenna prototype was chemically fabricated and fed using a standard 50Ω SMA connector via an inset feed. To test the prototype, a two-port RF network analyzer (KEYSIGHT P9377B) was employed, and reasonable good agreement was

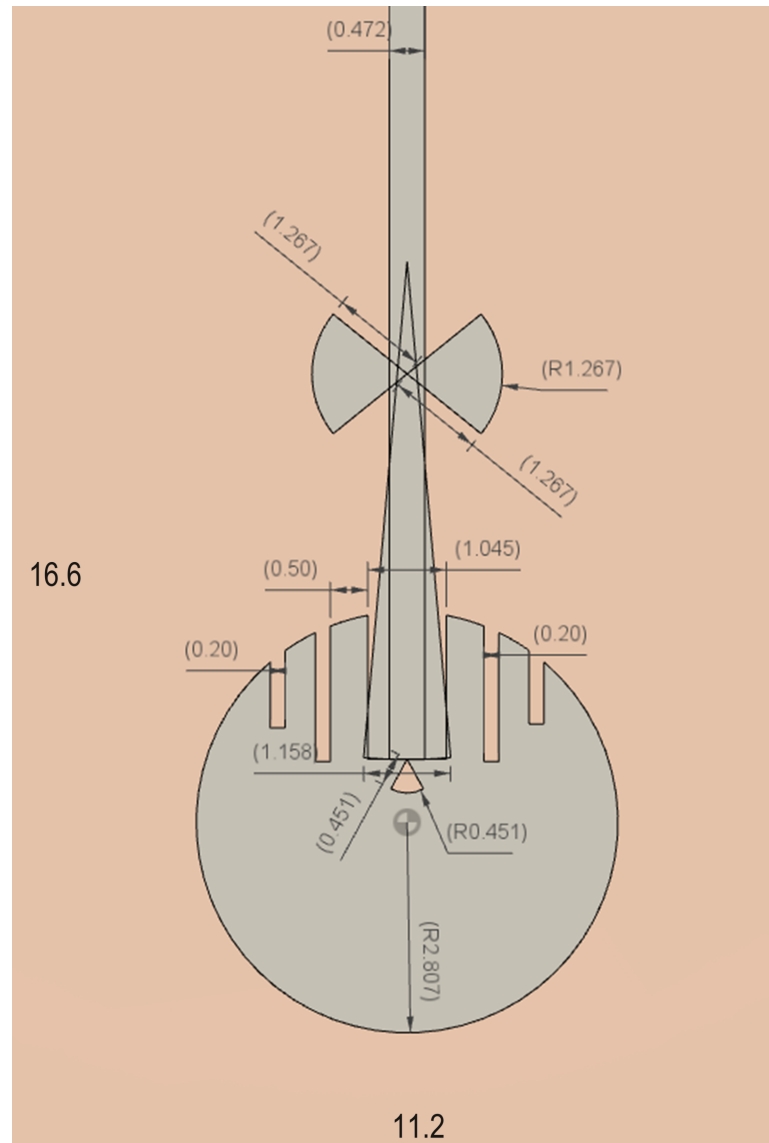


FIGURE 3.14: Geometry of the circular patch antenna

observed between the numerical and experimental return losses of the fabricated prototype, as demonstrated in Fig.3.15. However, there were slight variations in the measurements, which could be attributed to fabrication tolerances and numerical errors [12]. The large size of the connector, positioned very close to the radial structure at the feedline, contributes to the discrepancy between the simulation results (without the connector) and the measured results.

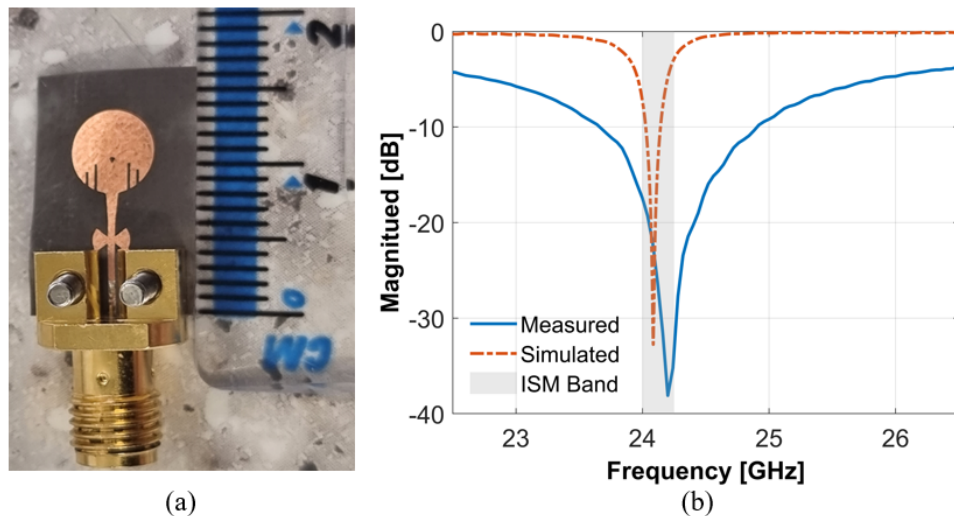


FIGURE 3.15: a) Prototype of the circular patch antenna. b) Measured reflection coefficients of the antenna.

3.3.2 Structural bending

In body-worn applications, it is crucial for an antenna to have structural conformability, meaning it should be able to withstand a certain degree of structural deformation and easily conform to the curved surface of the human body. To test the structural conformability of our antenna design, an experimental bending analysis was conducted with 14 mm curvature radii along the X-axis and Y-axis, as depicted in Fig.3.16. The results presented in Fig.3.16 demonstrate the matching of measured reflection coefficients of the antenna within the entire 24 GHz ISM band for the chosen curvature radii.

The maximum measured percentage of frequency shift was approximately 0.8%, indicating that the radial stubs were effective in minimizing frequency detuning caused by 14 mm bending radii. These findings demonstrate that our antenna design is highly conformal and a suitable choice for body-worn devices.

3.3.3 Radiation Pattern

To evaluate the performance of the designed antenna, we measured the far-field radiation patterns in the antenna lab of the School of Engineering, University

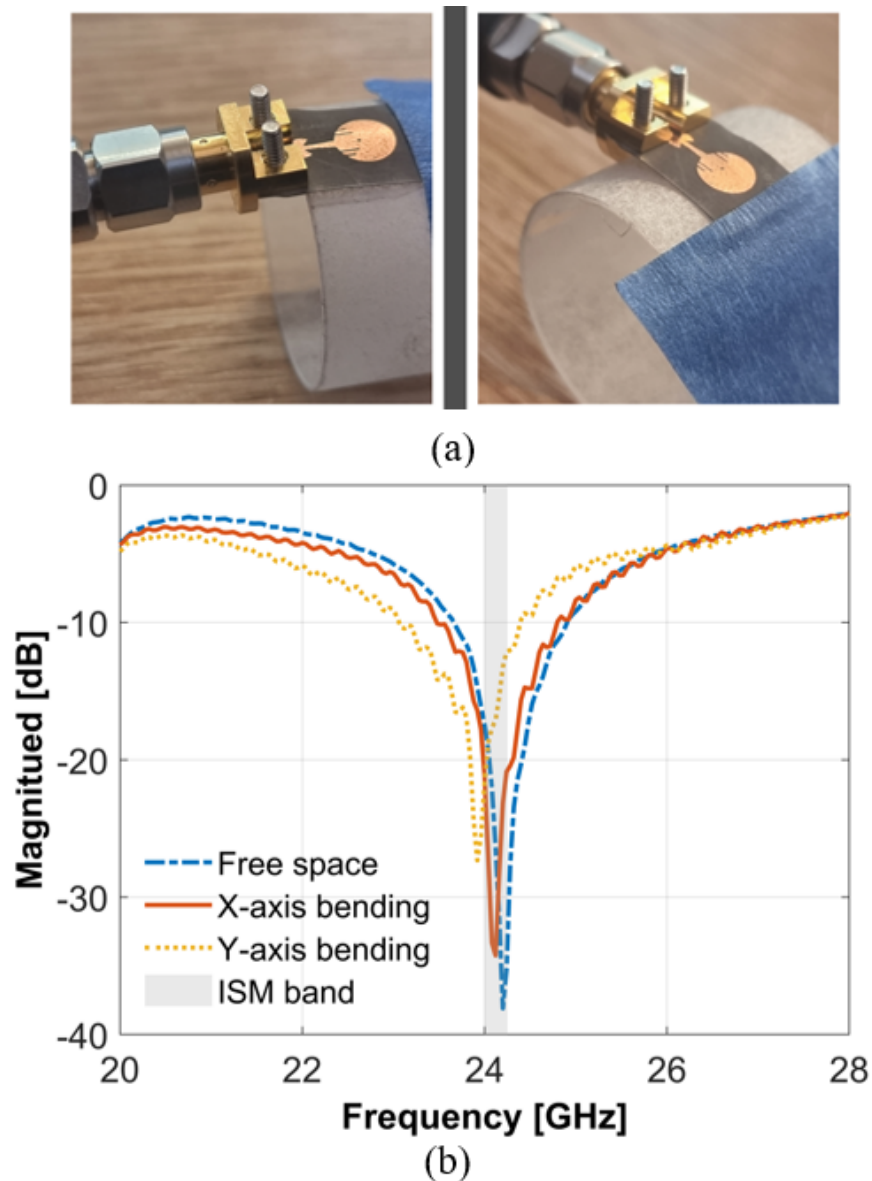


FIGURE 3.16: a) Antenna bent onto the cylinder along the X and Y axis. b) Measured reflection coefficients of the antenna while bending along the X and Y axis on the 14mm cylinder.

of Kent, using an anechoic chamber. The radiation patterns were measured at the center frequency of the ISM band, i.e., 24 GHz, with and without bending, as shown in Fig.3.17. The results indicate that the antenna has good radiation patterns, with a satisfactory front-to-back ratio (FBR) and a maximum gain of 4.067 and 2.06 dBi with and without bending, respectively. These results show that our designed antenna is a suitable choice for on-body Wireless Body Area Network (WBAN) communication.

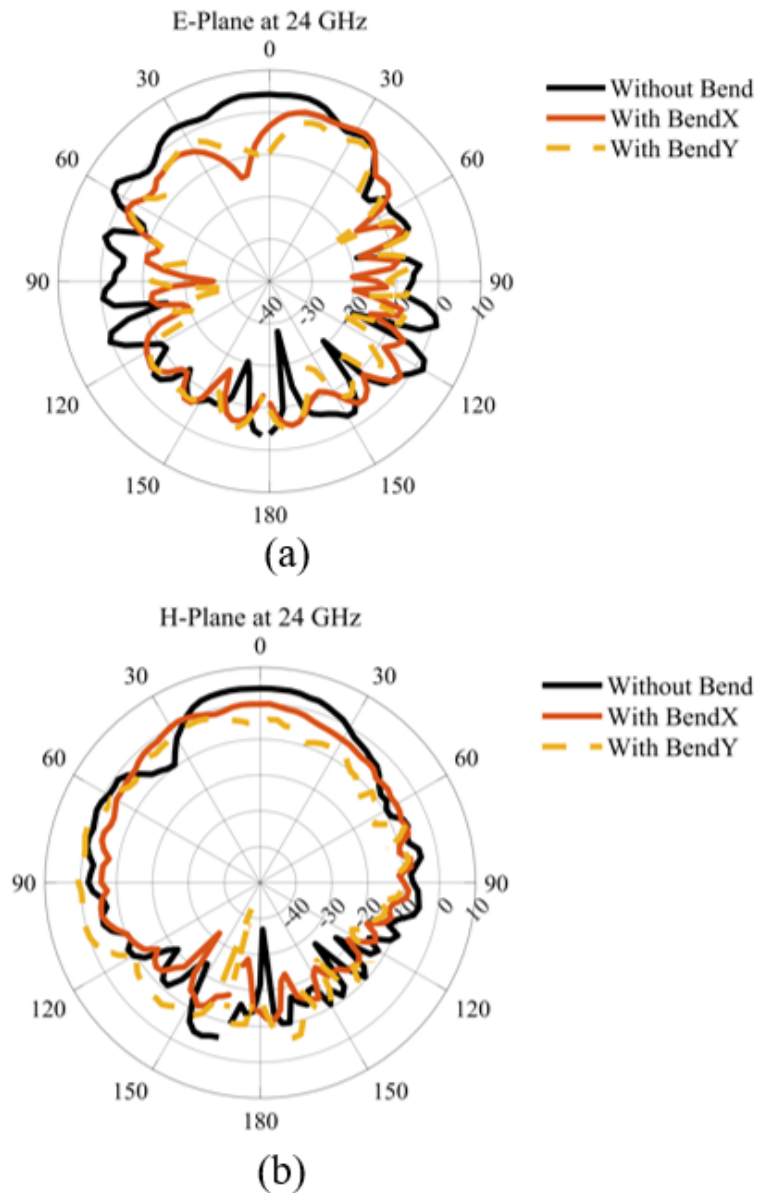


FIGURE 3.17: Measured radiation patterns of the antenna with and without a bend in free space and on-body. (a) xz plane and (b) yz plane at 24 GHz.

Additionally, we presented the free space gain against frequency in Fig.3.18, which provides further insight into the antenna's performance characteristics. Overall, our measured results demonstrate the suitability and effectiveness of the proposed antenna for on-body WBAN communication.

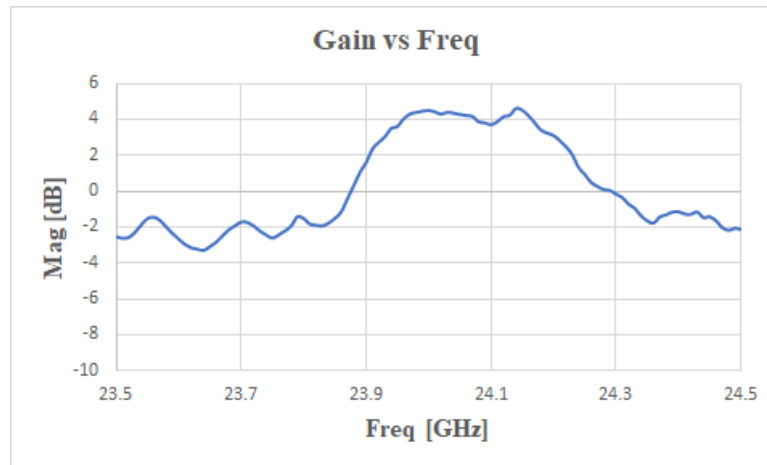


FIGURE 3.18: Gain vs Frequency plot of the circular patch antenna Fig.3.14

3.3.4 On-body Performance evaluation

To evaluate the performance of a flexible antenna when placed on the human body, a 28-year-old male volunteer was used. The volunteer's weight was measured to be 64 kg, and his overall height was 173 cm. The proposed antenna was tested on four different locations on the volunteer's body, as shown in Fig.3.19. The antenna was placed directly on the body without any separation. The measured reflection coefficients in free-space were compared for each location. The results show a slight shift in the resonant frequency, indicating that the human body has a small loading effect on the proposed antenna.

The antenna's impedance bandwidth covers the entire frequency spectrum at the 24 GHz ISM band. This slight variation in frequency is due to the high permittivity and lossy nature of the human body, which could be worsened without radial stubs. The radial stubs provide closely match the impedance of the antenna with the feedline even in the presence of human body biological tissues.

3.4 Planner Quasi-Yagi antenna array

The Yagi-Uda antenna is a type of directional antenna commonly used in wireless communications and remote sensing applications. It has a moderate gain and is

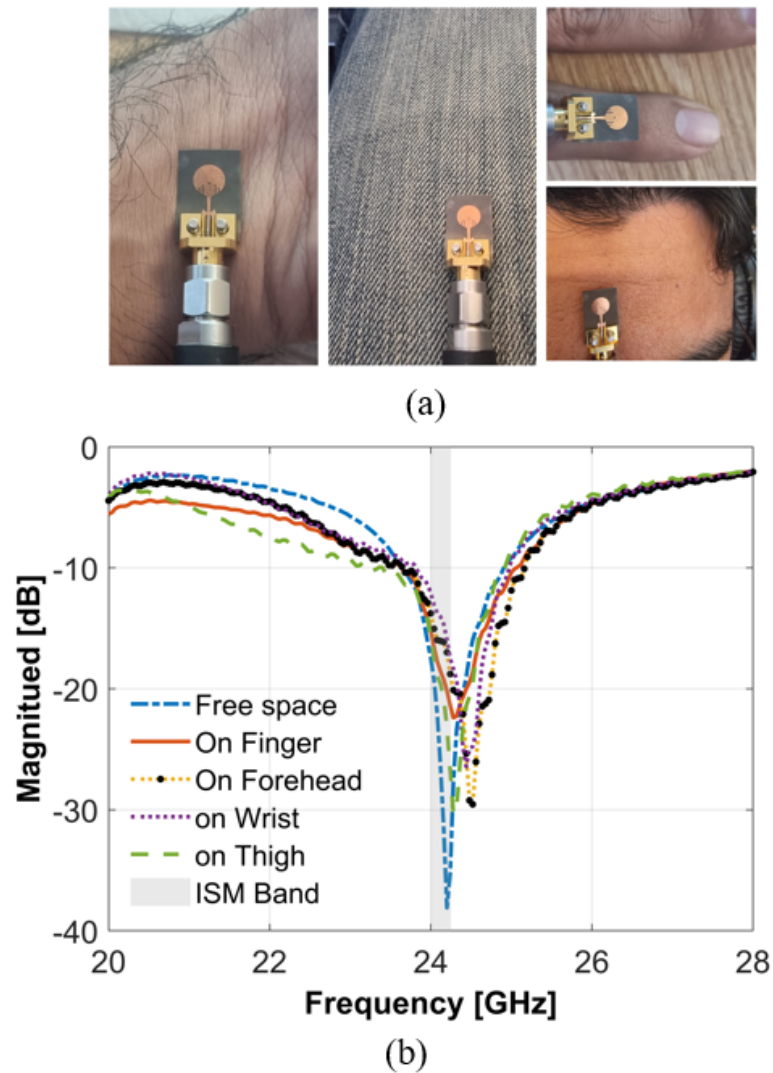


FIGURE 3.19: a) Antenna Placement on the body and b) Measured reflection coefficients of the antenna on the human body.

typically linearly polarized, meaning that it radiates electromagnetic waves in a single plane. The antenna's structure consists of several linear dipole elements, with one element acting as the "driver" and the others as "directors". The driver element is directly connected to the feedline and receives the input signal, while the directors are arranged in a specific pattern behind the driver. The mutual coupling effect between the driver and directors causes current to induce in the remaining dipole elements, resulting in a directional radiation pattern [19]. This antenna is particularly useful in wearable applications where high directionality is desired, such as for tracking or communication purposes [17]. Compared to broadside arrays, end-fire arrays typically exhibit better performance in terms of directional

gain and radiation efficiency [20]. Therefore, in the design of millimeter-wave (mm-wave) wearable antennas, end-fire arrays can be a suitable option for achieving high gain and directionality in a compact form factor. However, the challenge lies in finding an end-fire antenna array with a simple structure that can be implemented using planar technology.

3.4.1 Structure Design / Geometry

In the presence of dielectric material, an optimized driven element is resonant at 0.24λ from the center of the feed line as shown in Fig.3.20). The bottom layer of the antenna contains a reflector element that also acts as a ground plane for the feed line, which helps to improve its performance. As shown in Fig.3.14, the antenna also includes seven parasitic elements called directors, which are designed to have different lengths than the feed elements. The directors have lengths ranging from $0.35\lambda_0$ to $0.33\lambda_0$, and the spacing between the dipole elements is less than $0.22\lambda_0$. This design helps to improve the gain and directivity of the antenna, which are important characteristics for many applications.

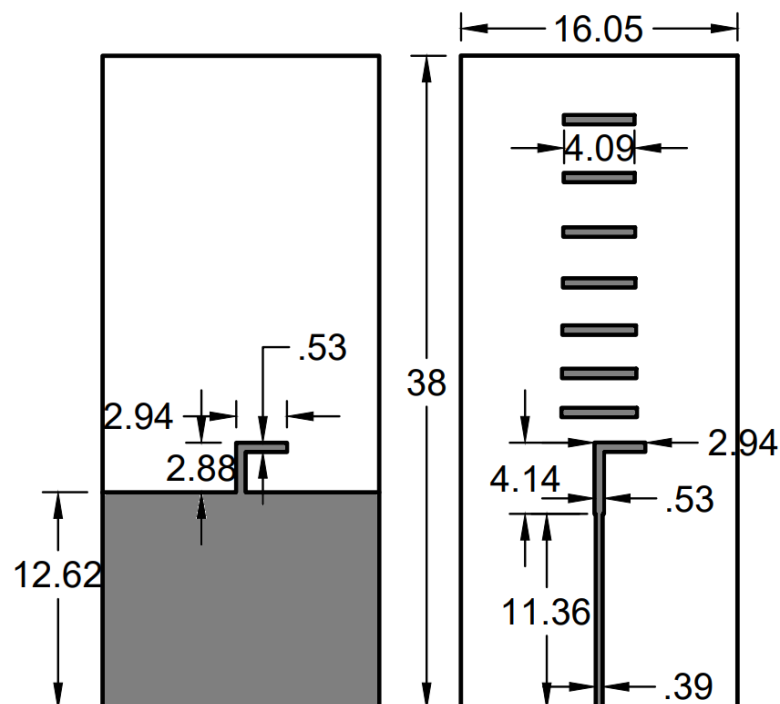


FIGURE 3.20: Planar Yagi Uda antenna geometry and dimensions

In addition, the antenna is optimized to achieve a large impedance bandwidth, which is necessary to overcome the degradation in return loss performance that can occur when the antenna is in close proximity to human tissue. However, there is a trade-off between gain and impedance bandwidth, as increasing the bandwidth can reduce the obtainable gain [21]. Therefore, it is important to carefully balance these factors when designing an antenna for use in wearable or implantable devices, where the antenna must perform well in the presence of biological tissues.

3.4.2 Performance analysis

To evaluate the performance of the designed antenna, both simulation and measurement techniques were used. The return loss of the antenna was computed using CST Microwave Studio and then a prototype was measured using a 60-GHz vector network analyzer (VNA) (Anritsu 37397c) in the 20-28 GHz band. As shown in Fig(3.21, there is a good agreement between the simulated and measured performance, indicating that the antenna design is accurate and reliable.

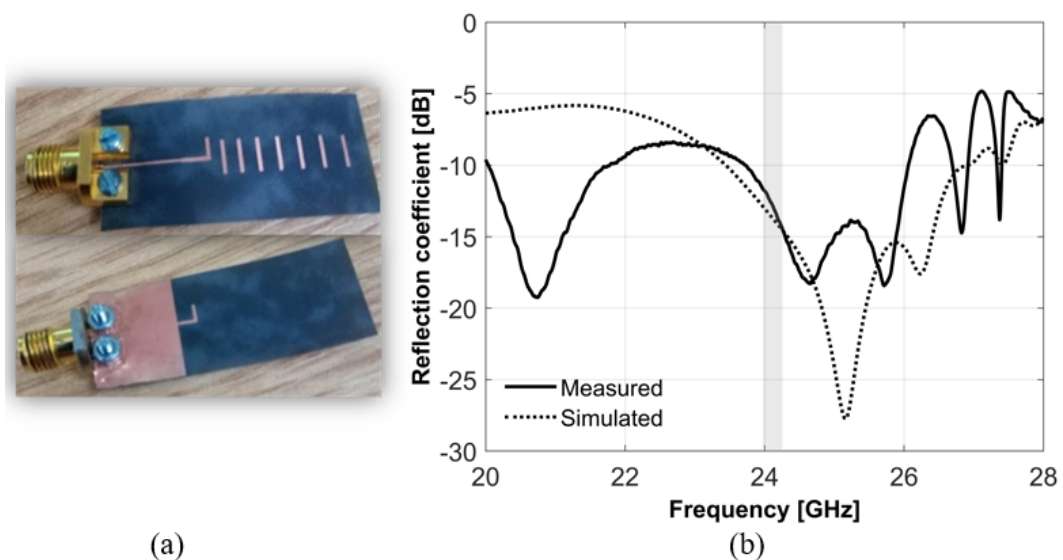


FIGURE 3.21: a) Planar Yagi Uda Antenna Prototype. b) Free space Yagi Uda antenna S_{11} performance.

The return loss of the antenna was found to be well below -10dB (23.8 to 26 GHz) in the 24 GHz ISM band, which is a free frequency band for wireless communication

systems. This suggests that the antenna has 2.2 GHz bandwidth and is suitable for use in a wide range of applications that operate within this band.

3.4.3 On-body performance

To assess the performance of the on-body antenna, S_{11} measurements were taken on a 61 kg, 178 cm tall male volunteer on four different mounting sites: chest, forehead, thigh, and wrist. The on-body reflection coefficient of the antenna is shown in Fig.3.22. It is observed that the varied capacitance and dielectric constant values of human tissues at different mounting sites result in distinct curves.

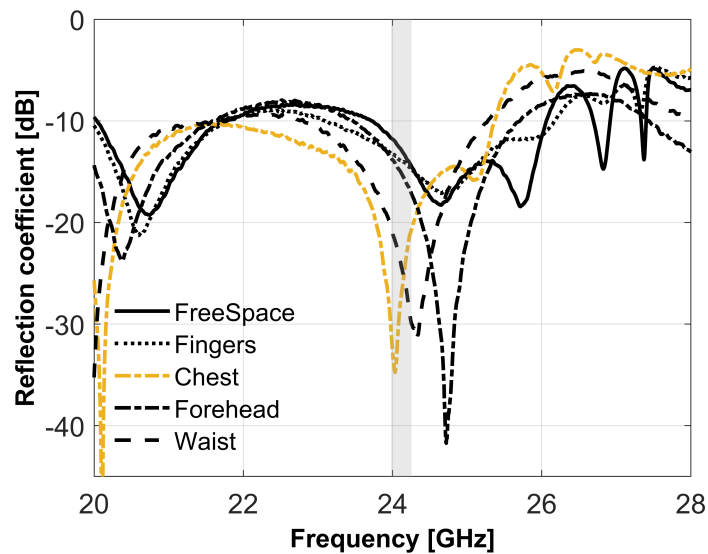


FIGURE 3.22: Return loss performance of Yagi Uda antenna when placed in different positions on the human body

The prototype antenna has a 2.2 GHz bandwidth and is optimized for the 24 GHz ISM band. The robust S_{11} response of the antenna when attached to the body makes it an excellent choice for wearable applications within this band. The antenna is capable of maintaining a low return loss even when mounted on different parts of the body, which is essential for reliable signal transmission and reception.

The ability to maintain a stable S_{11} response on different mounting sites is crucial for wearable applications, where the antenna is in close proximity to the body and may experience varying loading conditions. The on-body measurements on

the male volunteer demonstrate the suitability of the antenna for use in such scenarios, where reliable and robust performance is essential.

3.4.4 Effect of bending

The human body has many curved surfaces, which can cause structural deformation in wearable antennas. To evaluate this, S_{11} measurements of the antenna were taken while it was bent along the X- and Y-axis with radii of curvature of 15 mm, as shown in Fig.3.23.

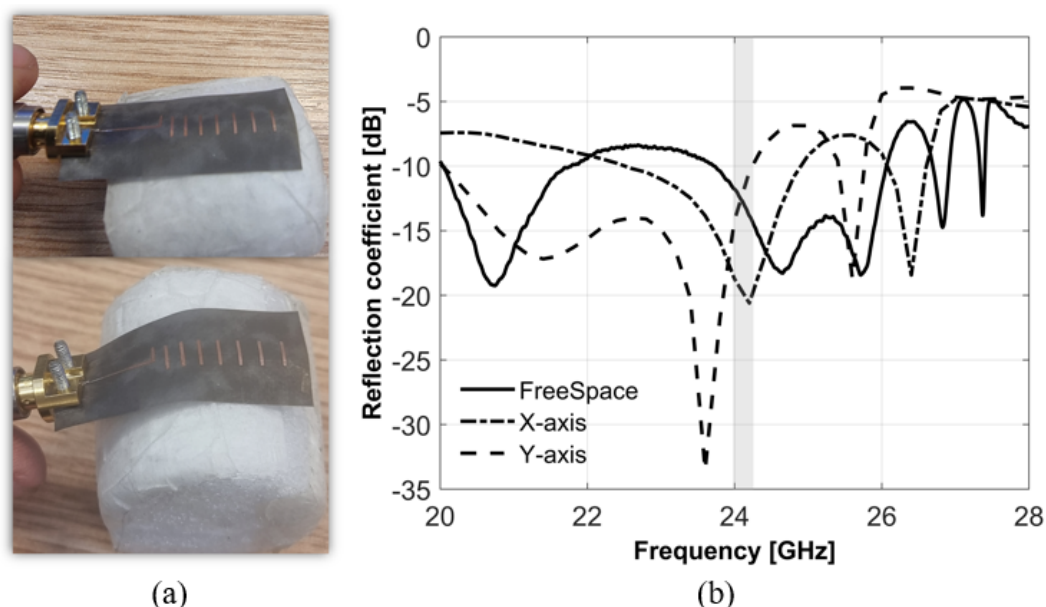


FIGURE 3.23: a) Planar Yagi Uda Antenna bent along a 14 mm radial cylinder. b) Reflection coefficients of Yagi Uda antenna when bending along a 14 mm radial cylinder.

The results of the investigation show that there is a slight shift of 400 MHz from the center frequency when the antenna is bent along the X-axis. However, a severe shift and degradation in the S_{11} performance is observed when it is bent along the Y-axis. Despite this, the S_{11} value remains better than -10 dB at 24.125 GHz, which is well within the ISM band. The shift in center frequency may be due to the change in the effective length of the antenna caused by the bending. The investigation demonstrates the antenna's ability to withstand structural bending while maintaining its performance within the 24 GHz ISM band. However, it is

important to note that the level of deformation that the antenna can withstand may depend on its design and materials. Therefore, further optimization may be required to ensure that the antenna can withstand more significant bending without compromising its performance.

3.4.5 Radiation pattern

Figs.3.24 and 3.25 display the measured E- and H-plane patterns of the antenna, which illustrate its directional characteristics. At 24 GHz, the realized gain is measured to be 10 dBi, indicating that the antenna is highly efficient at converting input power into radiated power. The results indicate that the radiation pattern of the antenna is predominantly in the forward direction. The presented Yagi antenna array has the potential for increased directivity with the addition of more array elements. The primary objective of this antenna is to function as a transmitter for off-body communication in subsequent path loss propagation modeling. Due to the intended application and the high frequency of operation (24GHz), on-body radiation pattern simulations and measurements were not conducted. Performing such simulations and measurements at this frequency would necessitate a substantial amount of computational resources.

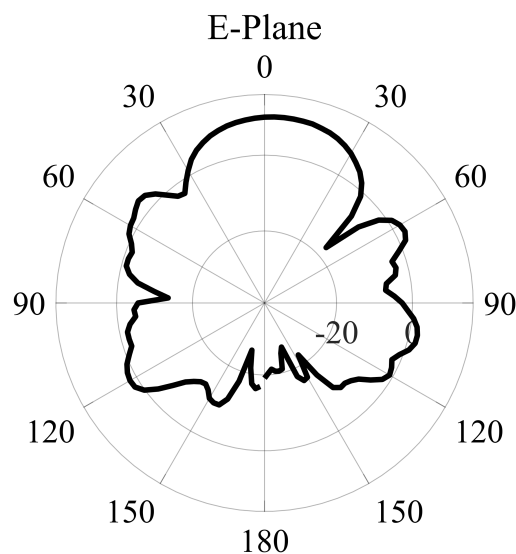


FIGURE 3.24: measured E-Plane radiation patterns of Yagi Uda antenna

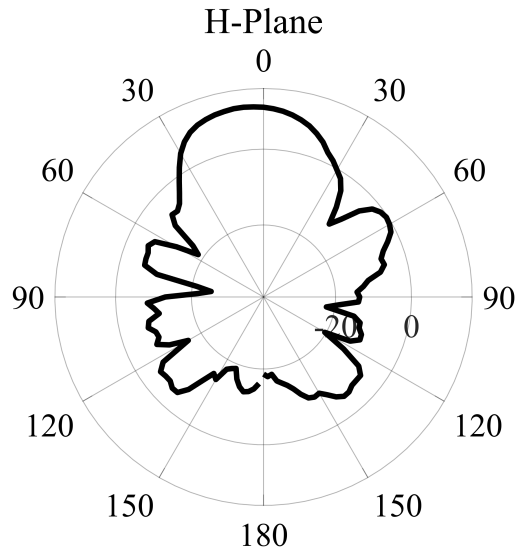


FIGURE 3.25: measured H-Plane radiation patterns of Yagi Uda antenna

3.5 Microstrip-based Vivaldi antenna

A microstrip-fed Vivaldi antenna was designed comprising of a conductive dielectric substrate, specifically Rogers 5880, which has an exponentially tapered slot in its metallization. In Fig.3.26, it can be seen that the antenna has a short length of slot line that connects a circular slot line cavity to the flared end of the tapered slot line. On the other side, the antenna has a microstrip line that terminates in a broadband radial quarter wave stub, with the base of the stub crossing the slot line near the circular cavity. The microstrip to slot line feed is used for excitation, which is terminated by a circular slot line cavity.

The radiation pattern of the Vivaldi antenna is end-fire, with a forward gain characteristic. If the taper profile, flare height, flare length, cavity diameter, substrate height, cavity diameter, and dielectric constant are selected appropriately, as illustrated in Fig.3.25, it can generate a symmetric beam in the E- and H- planes over a wide bandwidth. The design of the Vivaldi antenna allows for a broad frequency range with excellent gain and radiation pattern characteristics, making it an attractive option for various applications in the field of antenna technology.

Additionally, Fig.3.27 illustrates the antenna's performance in terms of the free

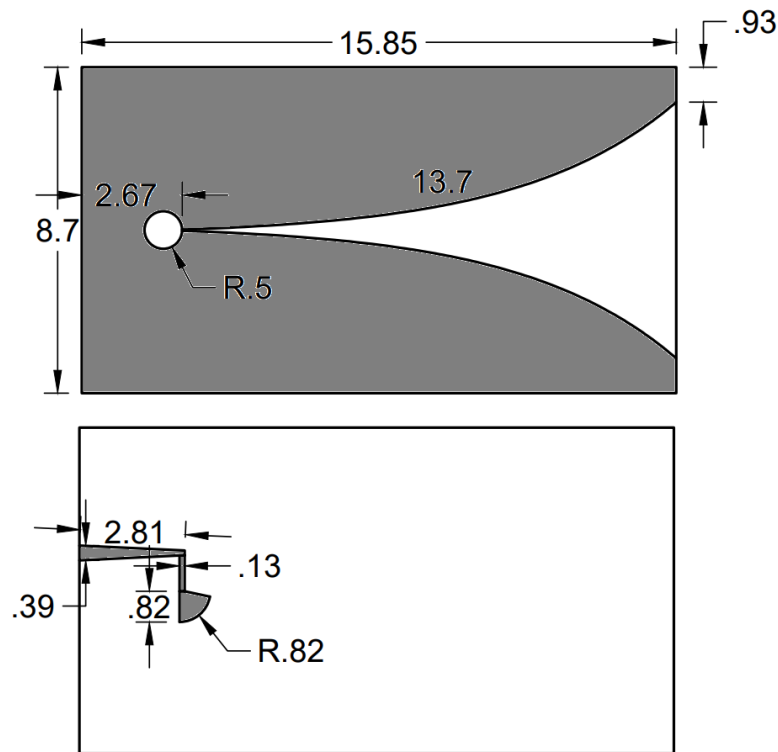


FIGURE 3.26: Geometry and dimensions of Vivaldi antenna

space reflection coefficient over a bandwidth of 2.5 GHz. Furthermore, the measured radiation pattern of the antenna is depicted in Figs.3.28 and 3.29. This pattern gives an indication of how the antenna's signal propagates in different directions, which is important for optimizing antenna placement and orientation. Finally, the realized gain of the antenna, which is a measure of how much power is radiated by the antenna compared to a theoretical isotropic radiator, is approximately 7 dBi. This value is useful for comparing the performance of different antennas and for determining the range and coverage area of the antenna.

3.5.1 On-body performance

In order to evaluate the performance of the on-body antenna, S_{11} measurements were taken on a male volunteer who was 61 kg and 178 cm tall. The antenna was mounted on four different sites on the volunteer's body: the chest, forehead, fingers, and wrist. Fig. (3.30 shows the on-body reflection coefficient of the

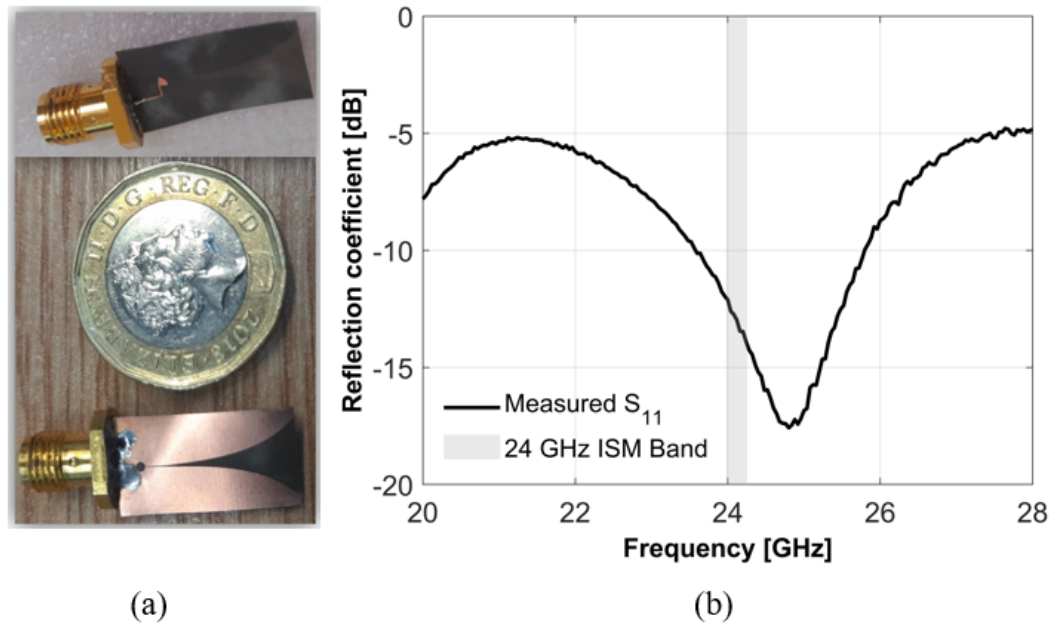


FIGURE 3.27: a) Vivaldi Antenna Prototype. b) Free space Vivaldi antenna S_{11} performance.

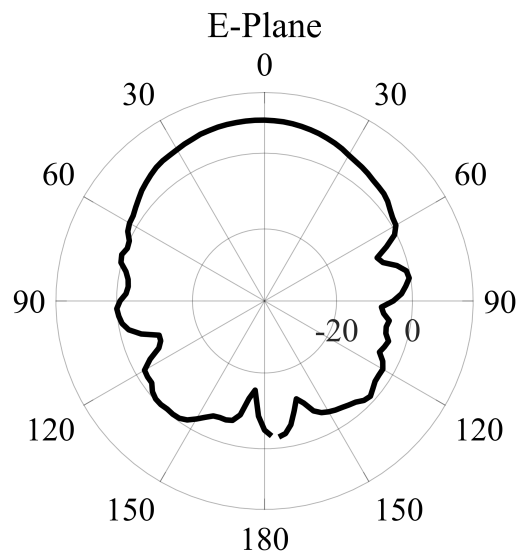


FIGURE 3.28: measured E-Plane radiation patterns of Vivaldi antenna

antenna, which reveals distinct curves due to the varied capacitance and dielectric constant values of human tissues at different mounting sites.

The prototype antenna has a 2.5 GHz bandwidth and is optimized for use in the 24 GHz ISM band. The robust S_{11} response of the antenna when attached to the body makes it well-suited for wearable applications within this frequency range. Furthermore, the antenna is capable of maintaining a low return loss even when

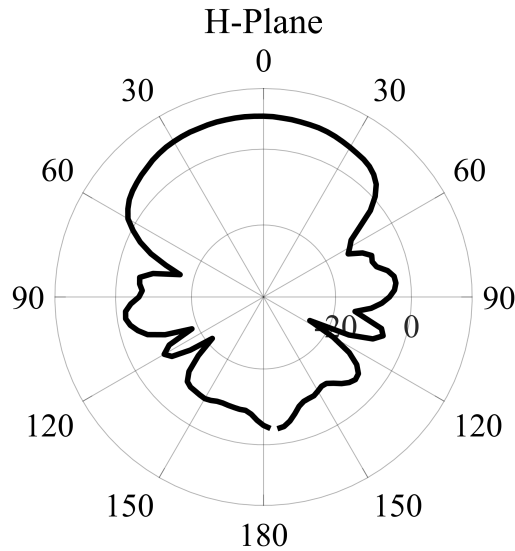


FIGURE 3.29: measured H-Plane radiation patterns of Vivaldi antenna

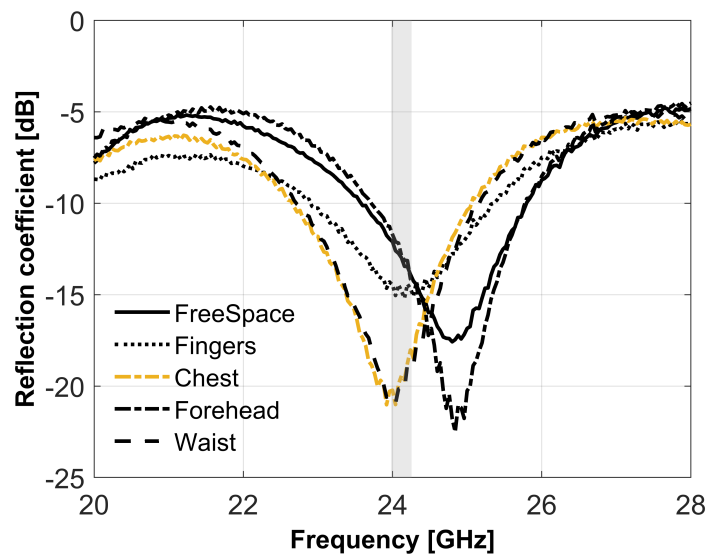


FIGURE 3.30: On-body return loss performance of Vivaldi antenna

mounted on various parts of the body, which is essential for ensuring reliable signal transmission and reception. This feature enhances the versatility of the antenna, making it suitable for use in a wide range of wearable devices.

3.5.2 Effect of bending

To evaluate this, S_{11} measurements were taken while the antenna was bent along the X- and Y-axes with radii of curvature of 15 mm, as illustrated in Fig.3.31.

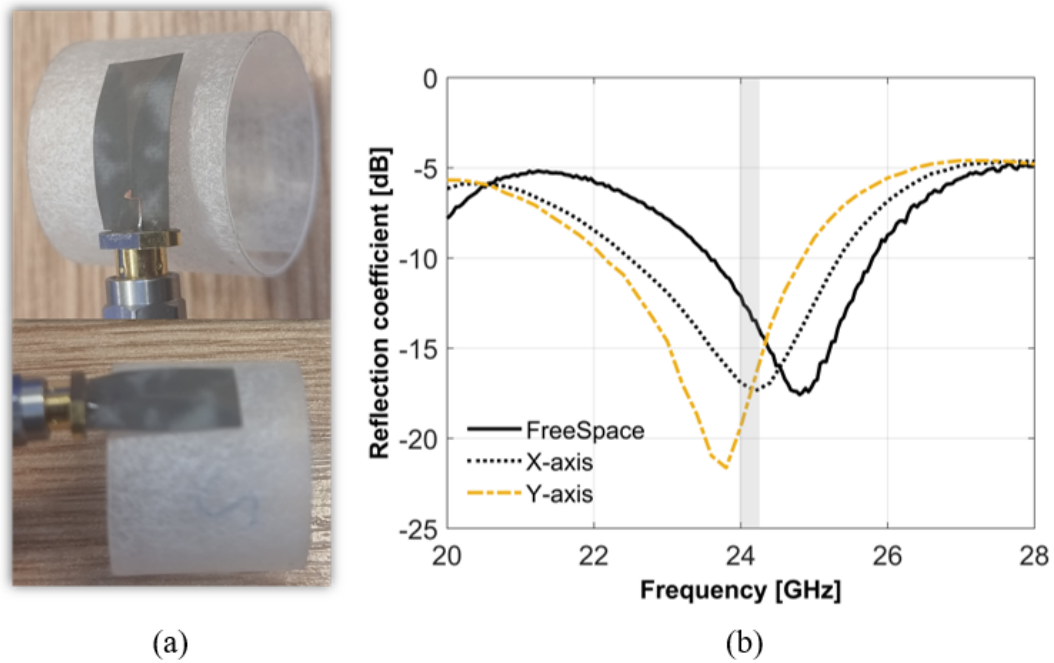


FIGURE 3.31: a) Vivaldi Antenna bent along a 14 mm radial cylinder. b) Reflection coefficients of Vivaldi antenna when bending along a 14 mm radial cylinder.

The investigation revealed that the antenna experiences a slight shift in the center frequency of 300 MHz when bent along the X-axis. However, a significant shift in the S_{11} performance was observed when the antenna was bent along the Y-axis. Despite this, the S_{11} value remained better than -10 dB at 24.125 GHz, which is well within the ISM band.

The shift in center frequency may be attributed to the change in the antenna's effective length resulting from the bending. These findings demonstrate the antenna's ability to withstand structural bending while maintaining its performance within the 24 GHz ISM band. This characteristic is crucial for wearable applications, where antennas may experience deformation due to the movements of the body, ensuring reliable signal transmission and reception.

3.6 Conclusion

This chapter presents on-body antennas designed for wireless body area networks operating at the 24 GHz ISM band. These antennas will be utilized for characterizing the on-body path loss channel later on. First, a low-profile thin-layered split square-ring EBG structure is presented at 24 GHz ISM band. A 5×5 element EBG array is investigated then placed beneath a bow-tie slot antenna. This antenna is the thinnest ($0.02\lambda_0$) EBG-backed antenna reported in the K band according to the authors' knowledge. Radiation measurements in the anechoic chamber show an increase in the gain by 2.6 dB and in the front-to-back ratio by 14.83 dB. High insensitivity to body proximity is observed from the on-body S11 performance of the EBG backed antenna.

Furthermore, insignificant variation in bandwidth and center frequency is noticed in the results when the proposed antenna is bent over curves of 30 and 15 mm. Also, measurements of the radiation patterns in bending scenarios show gain and directivity are not significantly altered. Finally, the SAR investigation in CST studio shows a 90% decrease in absorption rate because of the EBG shield under the 100mW input power. The proposed first antenna performance demonstrates its suitability for 24 GHz ISM band wearable applications.

The second antenna showcased a wearable, thin, and low-profile design, featuring radial stubs, for the 24 GHz ISM band. The antenna's size was effectively reduced, and its bandwidth improved by employing meandering slits. The antenna's impedance bandwidth was measured at 5%, spanning from 23.7 to 24.9 GHz, and it exhibited a peak gain of 4.1 dBi. To further test its performance, the antenna underwent structural deformation experiments under various curvature radii.

Results showed minimal frequency detuning, with a maximum of 0.3% along the X-axis and 1.04% along the Y-axis. Additionally, the bandwidth remained almost constant, making it highly suitable for flexible applications. In summary, the proposed antenna design is ideal for wearable and flexible devices due to its stable

performance, ability to withstand human body loading, and improved bandwidth and structural stability.

The goal of developing the aforementioned antennas was to utilize them for 24 GHz ISM band on-body channel characterization purposes. The novelty of the presented antennas lies in their ultra-thin structure, while simultaneously maintaining on-body performance under rigorous environmental tests within the required 24GHz ISM band. To achieve this objective, two additional antenna types were chosen, namely the Yagi Uda and Vivaldi antennas. These antennas were selected for their forward gain radiation patterns, with the Vivaldi antenna possessing a wider beam width than the Yagi antenna.

The Yagi antenna prototype demonstrated a gain of 10 to 12 dBi and a bandwidth of 5.8 GHz. In contrast, the Vivaldi antenna showed a stable on-body reflection coefficient with a bandwidth of 2.15 GHz. The measured pattern of the Vivaldi antenna indicated a wide beam directional radiation, with a realized gain of approximately 7 dBi.

Both antennas exhibited a robust S11 response when attached to the body and bent along a 14 mm radial cylinder in both the X and Y axes. Thus, these antennas are suitable for use in channel characterization applications due to their reliable performance and ability to withstand human body loading.

References

- [1] N. F. M. Aun, P. J. Soh, A. A. Al-Hadi, M. F. Jamlos, G. A. E. Vandenbosch, and D. Schreurs, "Revolutionizing wearables for 5G: 5G technologies: Recent developments and future perspectives for wearable devices and antennas," *in IEEE Microw. Mag.*, vol. 18, no. 3, pp. 108–124, May 2017.
- [2] Ali, M., Zafar, J., Zafar, H., O'Halloran, M. and Sharif, F., "Multiband ultra-thin flexible on-body transceivers for wearable health informatics." *Australian physical engineering sciences in medicine*, 42(1), pp. 53-63, 2019.
- [3] Arif, A., Zubair, M., Ali, M., Khan, M. U. and Mehmood, M.Q., "A compact, low-profile fractal antenna for wearable on-body WBAN applications," *IEEE Antennas and Wireless Propag. Lett.*, vol. 18, no. 5, pp. 981-985, May 2019.
- [4] H. Attia, M. L. Abdelghani, and T. A. Denidni, "Wideband and high-gain millimeter-wave antenna based on FSS Fabry-Perot cavity," *IEEE Trans. Antennas Propag.*, vol. 65, no. 10, pp. 5589–5594, Oct. 2017.
- [5] B. K. Tehrani, B. S. Cook, and M. M. Tentzeris, "Inkjet printing of multilayer millimeter-wave Yagi-Uda antennas on flexible substrates," *IEEE Antennas Wireless Propag. Lett.*, vol. 15, pp. 143–146, 2016.
- [6] N. Chahat, M. Zhadobov, L. Le Coq, and R. Sauleau, "Wearable endfire textile antenna for on-body communications at 60 GHz," *IEEE Antennas Wireless Propag. Lett.*, vol. 11, pp. 799–802, 2012.
- [7] Tayari, K., Werfelli, H., Chaoui, M., Ghariani, H. and Lahiani, M., Study of the effects of human tissue on performance of a loop antenna. *IOSR J. Electr. Electron. Eng.*, 11(4), pp.6-12,2016.

-
- [8] R. Das and H. Yoo, "Application of a compact electromagnetic bandgap array in a phone case for suppression of mobile phone radiation exposure," *IEEE Trans. Microw. Theory Techn.*, vol. 66, no. 5, pp. 2363–2372, May 2018.
- [9] X. Lin, B. Seet, F. Joseph, E. Li, "Flexible Fractal Electromagnetic Bandgap for Millimeter-Wave Wearable Antennas," in *IEEE Antennas Wirel. Propag. Lett.*, vol. 17, no. 7, pp. 1281–1285, Jul. 2018.
- [10] Ali, Mubasher, John C. Batchelor, Irfan Ullah, and Nathan J. Gomes. "Ultra-thin EBG backed flexible antenna for 24 GHz ISM band WBAN." In *Antenna Measurement Techniques Association Symposium (AMTA)*, Denver, Colorado, 2022 pp. 1-4.
- [11] Andreuccetti, D.; Fossi, R.; Petrucci, C. "An Internet Resource for the Calculation of the Dielectric Properties of Body Tissues in the Frequency Range 10 Hz–100 GHz," *IFAC-CNR: Florence, Italy*, 1997.
- [12] G. A. E. Vandenbosch, "State-of-the-art in Antenna Software Benchmarking—'Are we there yet?'," *IEEE Antennas Propag. Mag.*, vol. 56, no. 4, pp. 300–308, Aug. 2014.
- [13] Lin, X., Seet, B.C., Joseph, F. and Li, E., "Flexible fractal electromagnetic bandgap for millimeter-wave wearable antennas." *IEEE Antennas and Wireless Propagation Letters*, 17(7), pp.1281-1285, 2018.
- [14] Iqbal, A., Basir, A., Smida, A., Mallat, N.K., Elfergani, I., Rodriguez, J. and Kim, S. "Electromagnetic bandgap backed millimeter-wave MIMO antenna for wearable applications." *IEEE Access*, 7, pp.111135-111144, 2019.
- [15] Ashraf, N., Haraz, O., Ashraf, M.A. and Alshebeili, S., "28/38-GHz dual-band millimeter wave SIW array antenna with EBG structures for 5G applications." In *international conference on information and communication technology research (ICTRC)*, 2015, pp. 5-8.
- [16] L. Xu, L. Li and W. Zhang, "Study and Design of Broadband Bow-tie Slot Antenna Fed With Asymmetric CPW," in *IEEE Transactions on*

-
- Antennas and Propagation*, vol. 63, no. 2, pp. 760-765, Feb. 2015, doi: 10.1109/TAP.2014.2378265
- [17] G. Thiele, E. Ekelman and L. Henderson, "On the accuracy of the transmission line model of the folded dipole," *IEEE Trans. Antennas and Propagation*, vol. 28, no. 5, pp. 700-703, Sep. 1980.
- [18] Samineni, P., Khan, T., De, A. "Modeling of electromagnetic band gap structures: A review." *International Journal of RF and Microwave Computer-Aided Engineering*, 27(2), e21055, 2017.
- [19] J. Huang and A. C. Densmore, "Microstrip Yagi array antenna for mobile satellite vehicle application," in *IEEE Transactions on Antennas and Propagation*, vol. 39, no. 7, pp. 1024-1030, July 1991, doi: 10.1109/8.86924.
- [20] Feng, S., Xin, X., Chuxuan, R. "5G Millimeter Wave Endfire Array Antenna with Printed Inverted-F Structure." *International Journal of Antennas and Propagation*, 2022.
- [21] Koziel, S., Bekasiewicz, A. "Constrained optimisation for generating gain-bandwidth design trade-offs of wideband unidirectional antennas." *IET Microwaves, Antennas Propagation*, 13(7), 1017-1022, 2019.

Chapter 4

EBG backed Fractal geometry-based antenna for 24 GHz ISM band WBAN

4.1 Introduction

Nowadays, wireless networks for wearables have gained substantial attention within both academic and industrial communities as they offer the potential to further enhance the usage in military applications, navigation, remote monitoring of health-care systems, and sporting performance [1, 2]. The millimeter-wave (mm-wave) spectrum offers many benefits such as large data rates, larger channel multiplexes, reduction in interference because of the uncongested spectrum, miniaturization of devices, and unlicensed frequency bands [3]. Choosing a 24 GHz (ISM) band over 60 GHz enables a lower path loss environment, less shadow fading, and the use of lesser directive antennas. However, wearable antennas for body-centric applications have been mostly studied in the microwave spectrum rather than at mm-wave frequencies [4, 5]. Recently, two different inkjet-printed multilayers, multidirector mm-wave Yagi-Uda antennas have been developed on thin flexible material for 24.5 GHz (ISM) band applications [6]. In [7], a wearable end-fire

antenna has been proposed for 60 GHz on-body communication. However, these mm-wave body-worn antennas pose a potential radiation hazard to the human body because of high backward radiation (>5 dBi). The penetration depth of mm-waves to the human body is small due to the very short wavelength, and this restricts the risk to the skin. The value of the power transmission coefficient is extremely high in human tissues at mm-waves as compared to sub-6 GHz frequencies. Consequently, much of the electromagnetic energy is absorbed into human skin. This issue can drastically decrease the efficiency of the antenna as well as cause a risk to the wearer's safety. Therefore, adequate isolation is necessary between the antenna and the human tissues [8]. An electromagnetic bandgap (EBG) structure is considered an effective approach to reducing harmful radiation by suppressing the back lobe and surface waves [9]. An EBG array in a phone case has been developed to minimize human exposure at microwave frequency in terms of SAR by 24%. This further reduces the effects of the proximity of the human body and thereby enhances the gain of the antenna by 19% [10]. A textile-based square EBG has been developed at 26 GHz that improved the gain by 2.52 dB [11].

This chapter presents 2 iterations of Koch fractal geometry on the bow-tie slot antenna backed by the EBG/AMC structure. A 1st iteration Koch fractal base antenna has been published in [12] which Presented an ultra-thin Koch fractal geometry-based antenna integrated with a compact EBG/AMC structure having a total thickness of $0.02\lambda_0$. The proposed antenna geometry consists of Koch fractal-based bow-tie slots on a radiating monopole, backed by a compact 5×5 cell EBG structure demonstrating both bandgap and required phase reflection at 24GHz ISM band, which significantly reduces surface waves and the back-lobe of the antenna, respectively. The proposed structure uses an extremely thin (127 um) substrate of rogers 5880 which made it flexible enough to fit on any shape or part of the human body. both the two iteration fractal structures are compact and electrically thinner than comparable structures in the literature. They also possess good bandwidth when attached directly to the skin, a minimal shift in S_{11} while bending, a high front-to-back ratio (FBR) with a 30% decrease in thickness, and the largest decrease in SAR percentage when compared with existing wearable

EBG-backed antennas in K band. The chapter is organized as follows: Section 4.2 presents the design and characterisation of the EBG/AMC structure. Section 4.3 discusses the 1st iteration Koch fractal bow-tie antenna structure design and the performance of the prototyped EBG-backed antenna in terms of the reflection coefficient S_{11} , radiations pattern, on-body operations, structural bending, and SAR. Section 4.4 presents the 2nd Iteration Koch Fractal-based Antenna Design, Integration with EBG Surface, and on-body performance.

4.2 Electromagnetic band gap structure

This section provides the geometry and structure of an EBG structure. A split square ring resonator-based EBG geometry is designed and investigated. A unit cell of $W \times W = 3.18 \times 3.18 \text{ mm}^2$ on a Rogers 5880 dielectric substrate ($\epsilon_r = 2.2$) and thickness of 0.127 mm over a ground plane was simulated in CST Microwave Studio using periodic boundary conditions (PBCs), Fig.4.1. The proposed EBG unit cell consists of an approximately one wavelength perimeter split square ring resonator with coupling gaps on two corners. The proposed unit cell is also optimized to achieve good return loss performance under the proposed fractal geometry-based slot antenna, and that is why it has a different structure than presented in the previous chapter. The EBG structure is symmetric along both X and Y-axis as shown in Fig.4.1 and the proposed geometry acts as a two-dimensional electric filter within the 24 GHz ISM band where the surface exhibits high impedance. The change in the dimension of trace width and coupling gap varies the operating region, i.e., a decrease in the trace width and slot gap shifts the band gap region to lower frequencies. The unit cell was optimized to obtain the required phase reflection response at 24.125 GHz.

This configuration provides 0° phase shift from the reflected wave and behaves as an artificial magnetic conductor (AMC) [19]. Fig.(4.2) presents the simulated reflection phase diagram of a normally incident plane wave on the unit cell surface. The resonant frequency is 24.125GHz, and the bandwidth is approximately

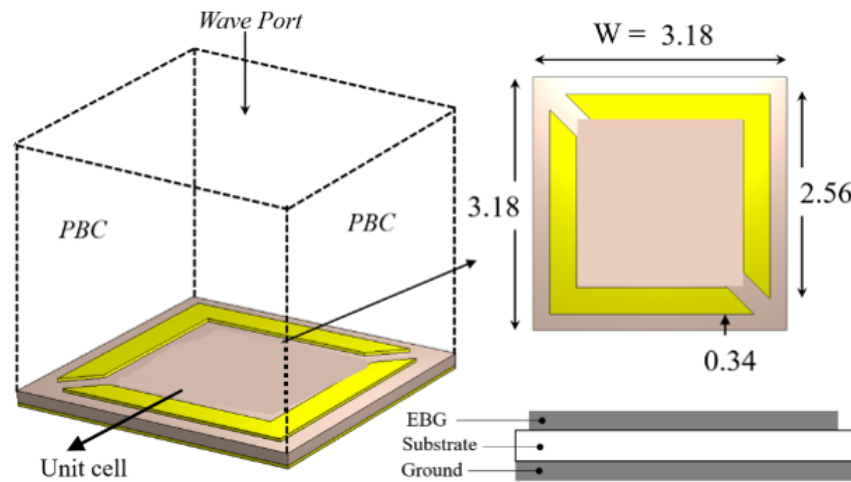


FIGURE 4.1: Proposed EBG geometry

250MHz. The AMC is a single layer and does not require vias which simplifies the fabrication and reduces cost.

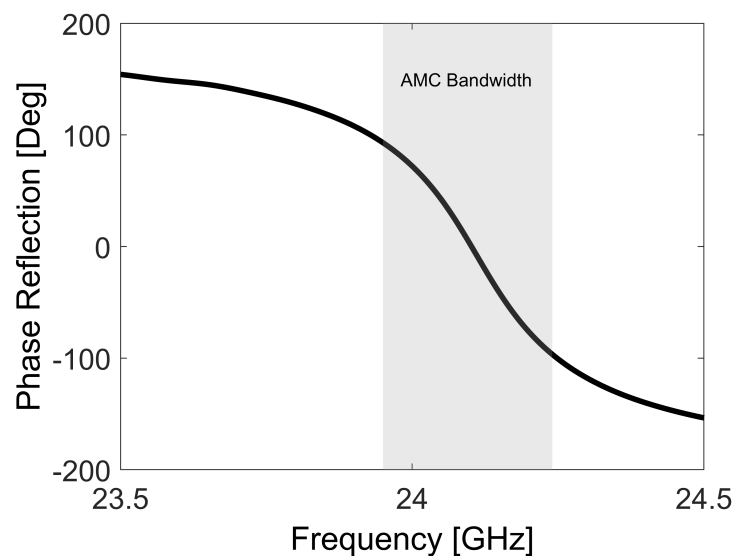


FIGURE 4.2: Phase reflection diagram

The characteristics of periodic electromagnetic bandgap (EBG) structures can be investigated by employing two different techniques: the dispersion diagram and the suspended transmission line method. We analyse the bandgap region using both approaches. To calculate the dispersion diagram from the unit cell, periodic boundary conditions and an appropriate phase shift are applied to the sides. The unit cell repeats infinitely with periodicity P_x , P_y , and lattice angle α . The impact of a finite structure in calculating a dispersion diagram arises from the use of

periodic boundary conditions to simulate an infinite repetition of the unit cell. Firstly, edge effects can occur at the boundaries of the finite unit cell, introducing reflections and interactions that differ from those in an infinite structure. Secondly, the periodic boundary conditions may not perfectly replicate the actual behavior of the finite unit cell, particularly in regions where the assumptions of periodicity break down. Finally, size-dependent phenomena and the finite nature of the unit cell can lead to deviations in the dispersion diagram. The CST Eigenmode Solver is used to generate the dispersion response in Fig.4.3. The vertical axis shows frequency, while the horizontal represents transverse wavenumbers, specifically Γ , X, and M as indicated in the inset. The hexahedral mesh type is used and JDM (Jacobi-Davidson Method) eigenmode solver is chosen, which is found to be faster for the given example. Dispersion diagram calculations often prefer the Jacobi-Davidson method due to its effectiveness in efficiently solving the large and sparse eigenvalue problems commonly encountered when analysing intricate periodic electromagnetic structures. An EBG bandgap region from 23.9 to 24.48 GHz is observed, and surface waves will be suppressed in this band. Therefore, the interaction between the fields and the skin at the structure edge is reduced. The AMC characteristic improves the forward radiation, while the EBG effect improves the decoupling of the structure from the skin.

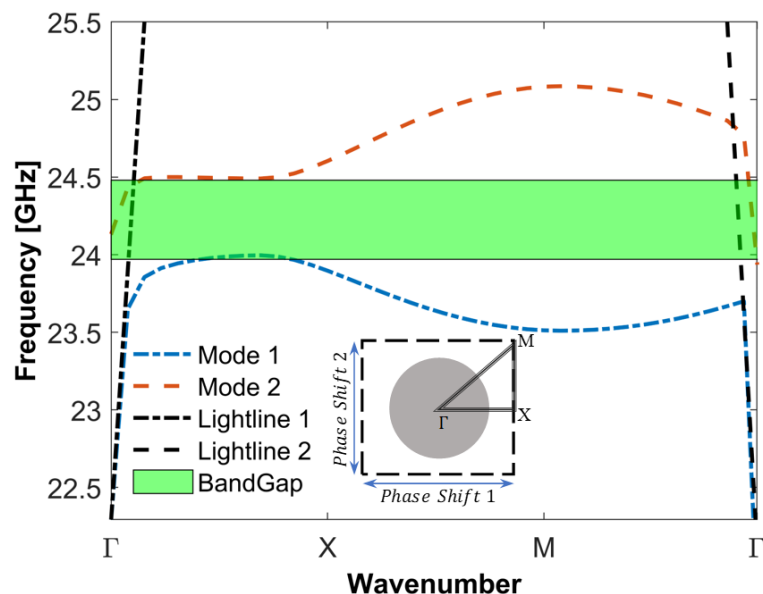


FIGURE 4.3: Dispersion diagram

The dispersion diagram represents the relationship between the frequency (or wavelength) and the propagation constant of these modes. mode 1 corresponds to the primary mode with the lowest frequency or longest wavelength that can propagate through the structure. Mode 2, being the second mode, has a higher frequency (or shorter wavelength) compared to mode 1.

To further verify the bandgap region, the suspended transmission line approach was modeled using a 0.5 mm wide microstrip line placed $0.02\lambda_0$ above a 5×5 EBG array. The simulated transmission coefficient is presented in Fig.4.4. The S_{21} is below -20 dB between 23.962 GHz and 24.353 GHz.

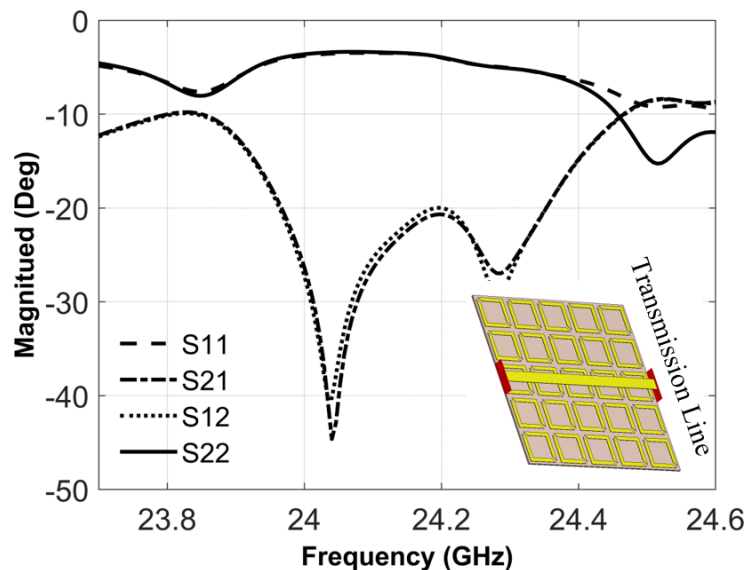


FIGURE 4.4: EBG suspended transmission line S parameters

4.3 First Iteration Koch Fractal based Antenna Design and Integration with EBG Surface

In this subsection, the Koch fractal geometry-based slotted bow-tie antenna is presented in Fig.4.5. To achieve flexibility, the antenna is kept the EBG (no gap between EBG and antenna), reducing the impedance bandwidth. Then, the bandwidth of the proposed antenna is further enhanced by adding fractal repetition [13]

along the resonant length of the patch. This fractal bow-tie slot antenna has single metallization and dielectric layers, such that ungrounded coplanar waveguide feeding is a suitable option in terms of fabrication. After the integration of the antenna with the EBG structure, grounded CPW feeding was chosen as the EBG array has a metal ground plane. The female type $50\ \Omega$ SMA edge mount connector (HRM(G)-300-467B-1 specified to 28 GHz) was simulated with the full structure to improve comparison with measurement. The fractal bow-tie slot antenna simulations were performed using the CST time domain solver and a prototype was fabricated using chemical etching.

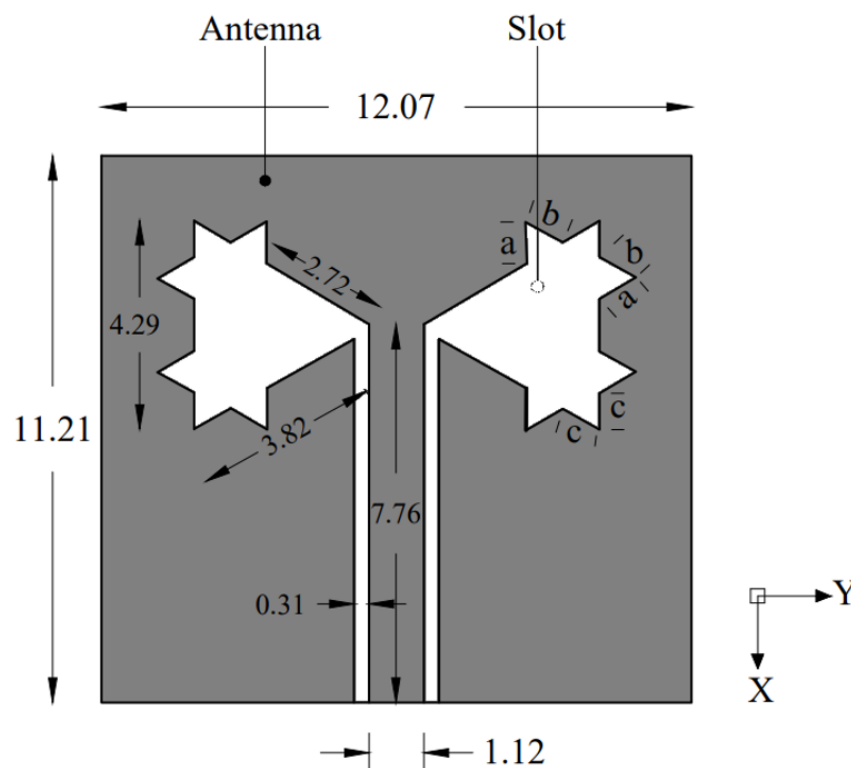


FIGURE 4.5: Koch fractal based Bow-tie slot antenna geometry, $a = 0.72$, $b = 0.67$ and $c = 0.75$ mm

A 5×5 EBG structure was placed underneath the slot antenna. Fig.4.6 shows the dielectric and metal layer stack of the antenna-EBG structure, this prototype has an edge-mounted connector and no air gap between the layers. The EBG-backed antenna was shown by measurement in Fig.4.6 to be well isolated from the skin meaning the design process was valid without accounting for body loading. This

configuration is suitable for wearing on the surface of the body as the resultant antenna is ultra-thin with overall dimensions of $16.19 \times 16.19 \times 0.254 \text{mm}^3$.

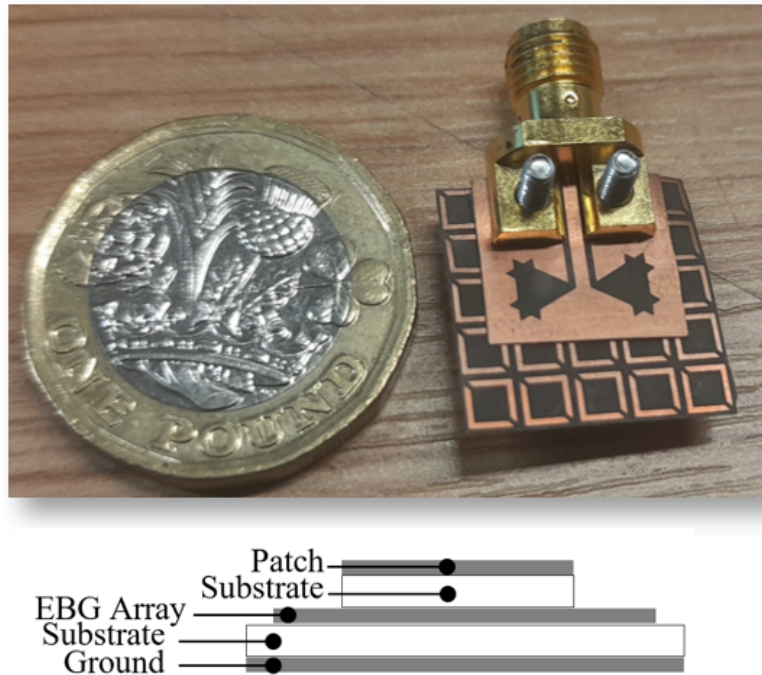


FIGURE 4.6: Integration of EBG with antenna

4.3.1 Results and Discussions

This section presents simulated and measured S_{11} and radiation patterns together with a consideration of body loading and a deformation study.

4.3.1.1 Reflection Coefficient Evaluation

The prototype was tested in-house, and the measured reflection parameters were taken with a 65 GHz VNA (Anritsu 37397c). Fig.4.7 shows the S_{11} values are less than -10 dB from 22.6 GHz to 25.35 GHz (bandwidth of 2.75 GHz). The shaded bar in Fig.4.7 shows the simulated and measured reflection coefficient of the EBG-backed antenna is below -15 dB in the ISM band (24 - 24.250 GHz). Owing to the unavailability of a comprehensive whole-body skin model at 24 GHz and the significant computational resources required for simulating the skin model,

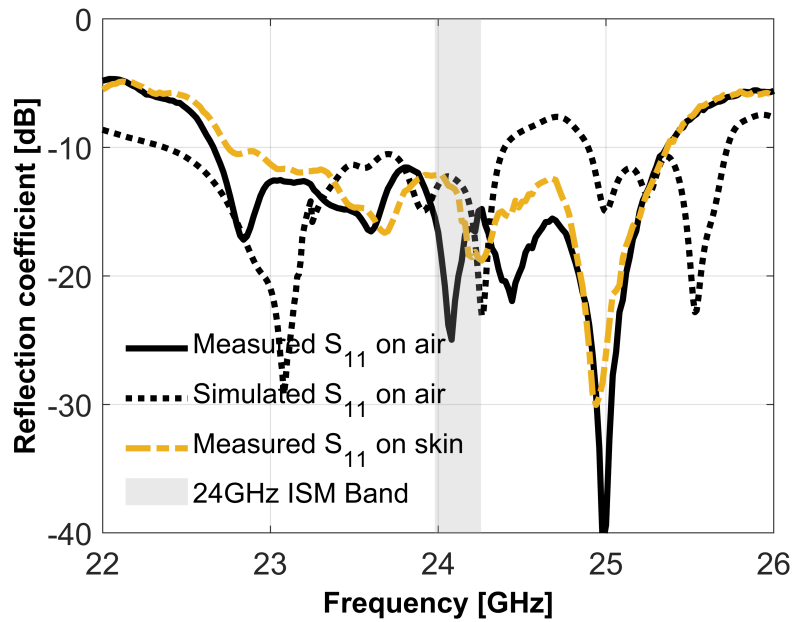


FIGURE 4.7: S_{11} of EBG backed antenna shown in Fig. 4.6.

including the antenna structure, we have opted to forego the simulation of the antenna under a whole-body skin model. Instead, we rely on measured results, as they provide a more accurate representation of the antenna's behavior when interacting with human skin. This approach ensures efficiency in resource utilisation while maintaining the reliability of our findings. This investigation considers the antenna for application in the 24 GHz ISM band, so although the structure is a wider band, this additional performance is not required here.

4.3.1.2 Far-Field Radiation Properties

The far-field radiation measurements were taken in an anechoic chamber. Fig.4.8 and 4.9 shows the H- and E-plane polar plots with and without the EBG/AMC array structure at 24 GHz. Placing the EBG/AMC structure underneath the antenna suppresses the back lobe by 12.6 dB at 24 GHz, whereas the realized gain increases by 2.3 dB to 5.1 dBi at 24 GHz. The results indicate the effectiveness of the EBG/AMC structure in suppressing surface waves and reflecting radiation away from the human body. Simulated radiation patterns on and off the skin are included in Fig.(4.8 and 4.9). Given the ultra-thin structure of the antenna,

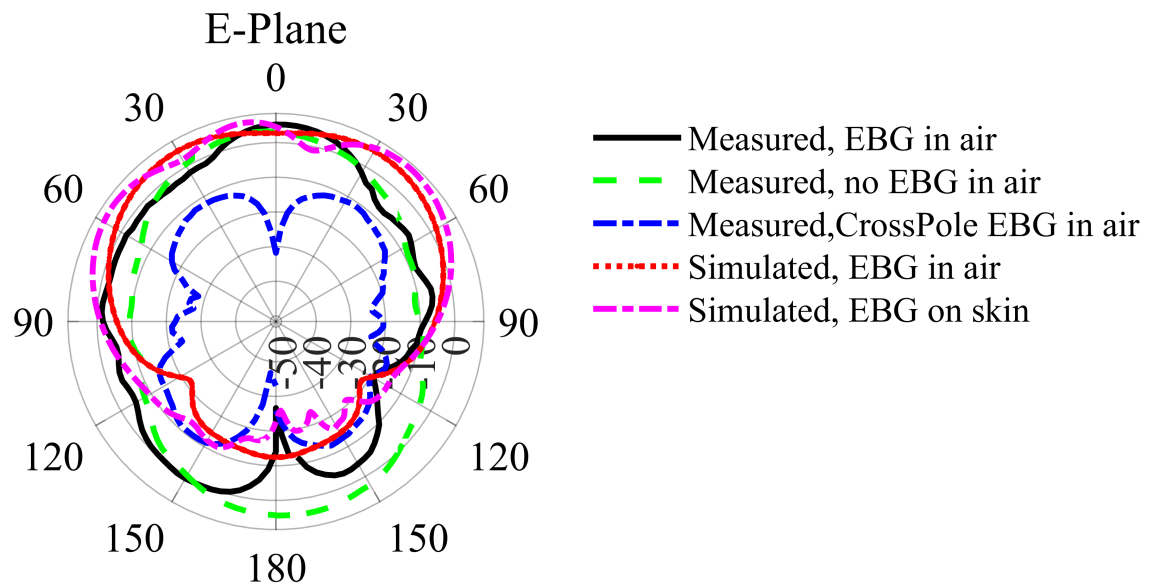


FIGURE 4.8: Measured and simulated E Plane radiation polar plots of EBG backed antenna shown in Fig. 4.6.

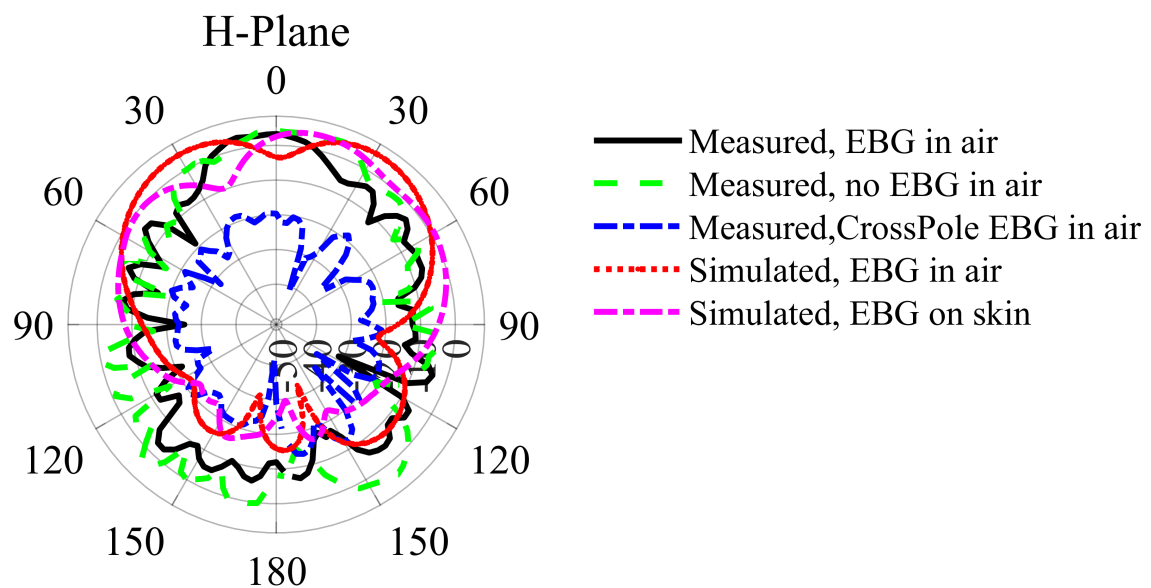


FIGURE 4.9: Measured and simulated H Plane radiation polar plots of EBG backed antenna shown in Fig. 4.6.

obtaining accurate measurements of the radiation pattern poses a considerable challenge. The difficulty lies in achieving a straight and conforming surface for the antenna, directed towards the transmitter. This inherent challenge introduces inaccuracies in both the simulation and measured results. It can be seen that the EBG reduces the skin loading effect such that the difference at a given angle in the rear hemisphere is within about 10 dB.

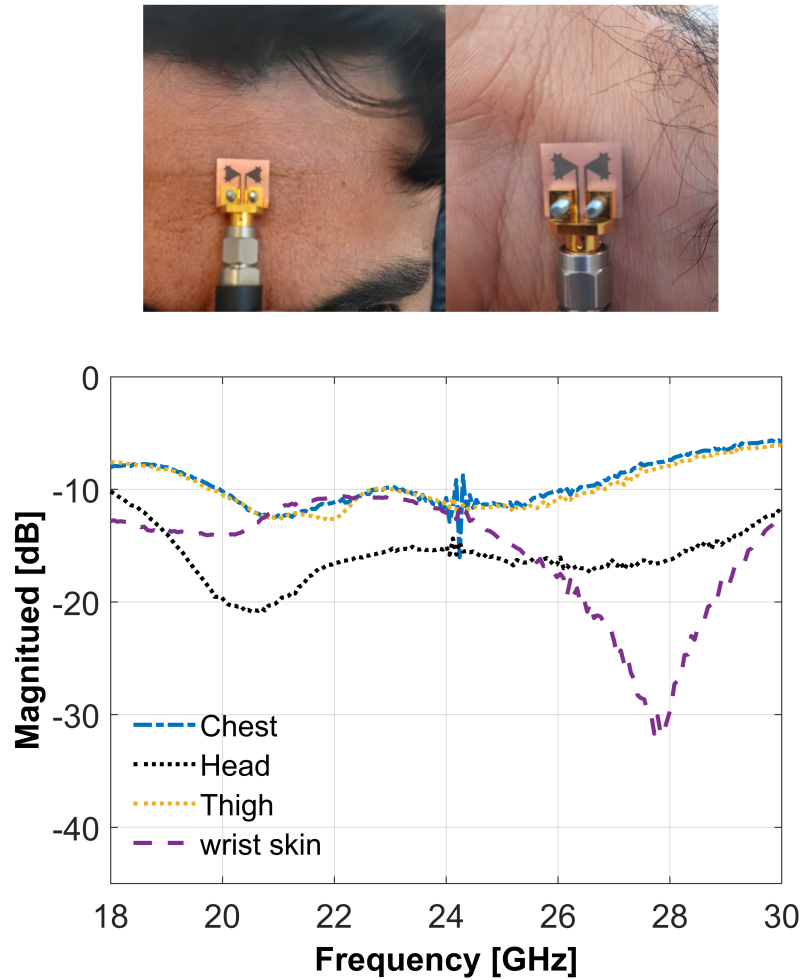


FIGURE 4.10: Measured reflection coefficients of the antenna on the human body without EBG shown in Fig. 4.5.

4.3.1.3 On-body Performance

As the proposed EBG suppresses backward radiation, the prototype antenna should be tolerant to human tissue loading. On-body measurements were performed on the chest, forehead, thigh, and wrist of a male volunteer who weighed 61 kg and was 178 cm in height. The S_{11} of the human body-loaded antenna is presented in Fig.4.10. The curves differ due to the varying capacitive and dielectric constant values of human tissues at different mounting sites. However, apart from the thigh, all measured S_{11} were at < -10 dB over the desired 24 GHz ISM band. Fig.4.10 illustrates that without an EBG/AMC, the structure is highly lossy across the entire measured band, and the antenna is detuned in all cases. Utilising only a ground plane beneath the antenna exacerbates the return loss, thereby

demonstrating the enhanced effectiveness of the proposed Electromagnetic Band Gap (EBG) structure.

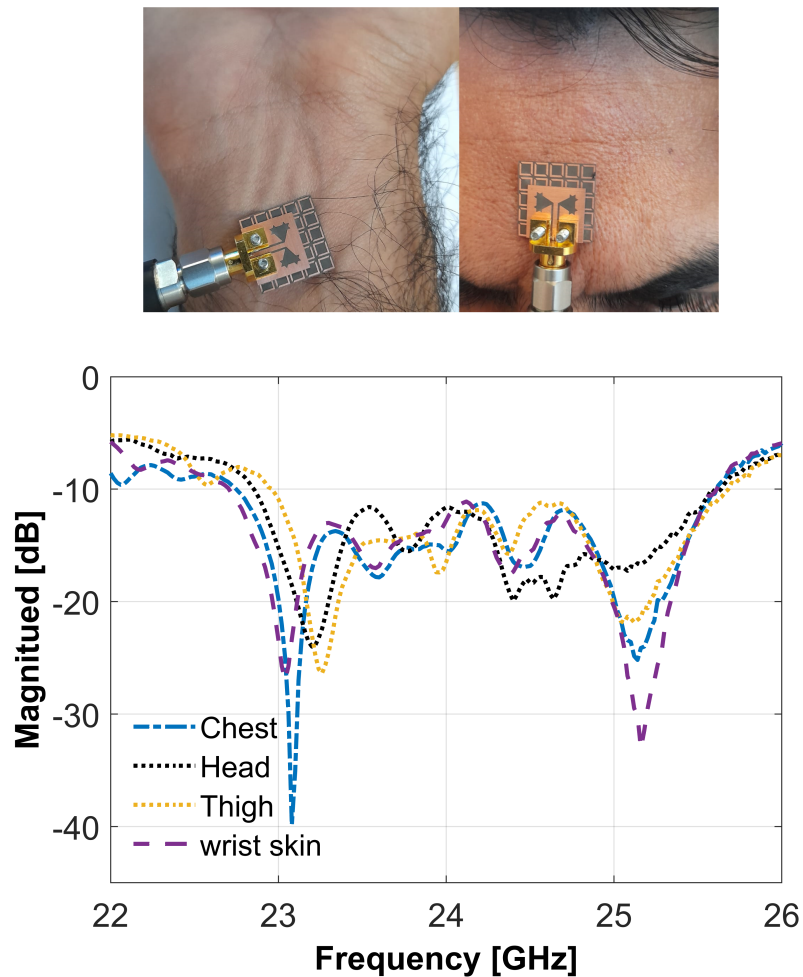


FIGURE 4.11: Measured reflection coefficients of the antenna on the human body with EBG shown in Fig. 4.6.

When the EBG/AMC is added, in Fig.4.11, the structure is tuned for the ISM band for all mounting sites, and the out-of-band loss decreases by around 5 dB. The prototype not only covers the 24 GHz ISM band but has 2.7 GHz bandwidth. Hence, this optimized EBG-backed Koch fractal bow-tie slot antenna with stable S11 response when attached to the body is a suitable candidate for 24 GHz ISM band wearable applications.

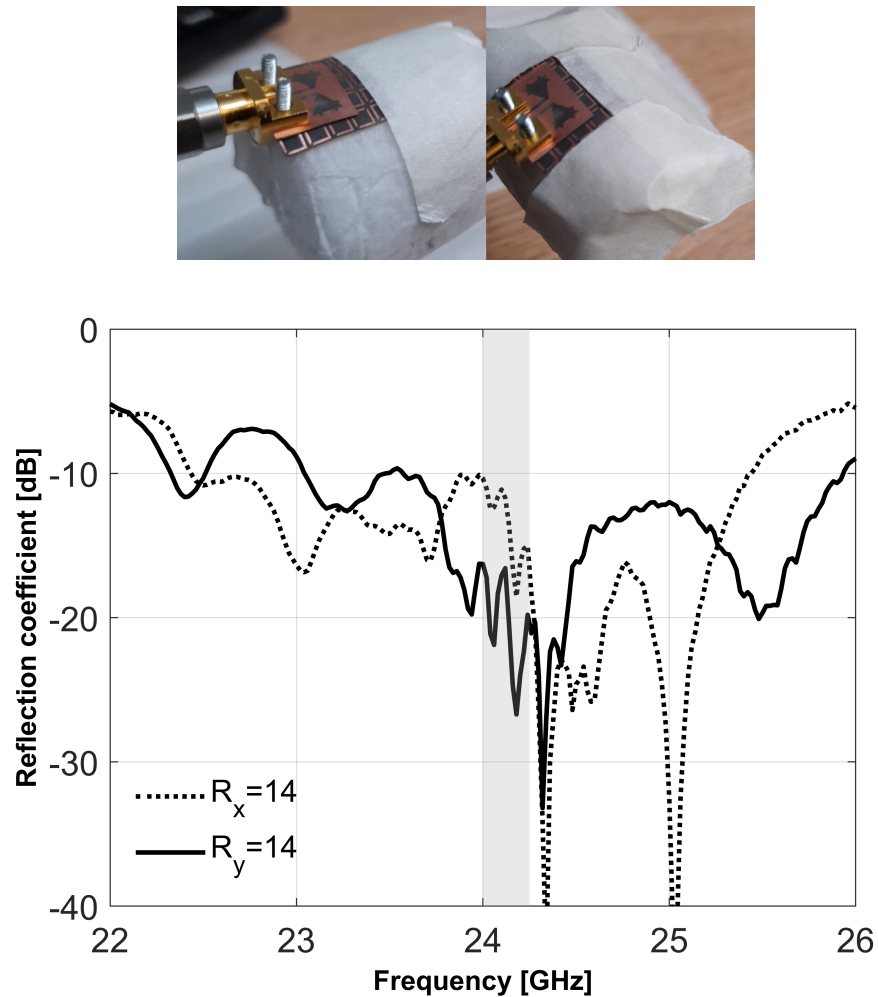


FIGURE 4.12: Reflection Coefficient of the EBG-backed antenna (Fig. 4.6.) when bent on 14 mm radial cylinder along "Y" and "X" axis.

4.3.1.4 Structural Conformability

The chosen antenna placement positions can be considered relatively flat. However, the capability to bear some structural deformation while retaining radiation performance with close conformance to the curved surface of the body is important for on-skin mounting. Therefore, the structure was further investigated under bending conditions. Fig.4.12 shows the reflection coefficient measurements when the antenna is bent around a polystyrene foam cylinder separately along the X and the Y-axis. The dielectric constant of the available polystyrene is between 1.3 to 1.6. A tissue phantom was not used, as it has been shown that the antenna is not strongly loaded by the body and therefore the curvature effect would dominate.

Due to the reduction in resonant length while bending, a slight shift in center frequency can be seen from the plot when bent along the X-axis. A severe detuning and a shift of 400 MHz are observed when bent along the Y-axis. Bending along the 'y-axis exerts a more significant impact, as it results in greater deformation of both the radiating patch element and the feeding portion of the antenna compared to bending along the x-axis. However, even with a 14 mm radius of curvature, the EBG-backed bow-tie slot antenna still achieves reasonable reflection coefficient values (< -10 dB) at the 24 GHz ISM band.

Furthermore, Fig.4.13 presents the radiation patterns under bending for radii R_x and $R_y = 14$ mm along the Y- and X- axis. The directivity is seen to be around -2.1 dB for both axes of curvature.

4.3.1.5 Specific Absorption Rate Evaluation

To investigate the performance of the antenna in terms of specific absorption rate (SAR), a rectangular three-layer skin-fat-muscle block model (Fig.4.14c) is used in CST MWS. Table 4.1 presents the dielectric properties of dry skin, fat, and muscle layers, which were obtained from the online website of the Italian National Research Council [14]. The total size of the three-layer tissue model was $50 \times 30 \times 6$ mm³. For the SAR evaluation, there was a 2mm gap between the skin and the EBG ground plane due to the height of the connector. Fig.4.14 presents the SAR distribution using the IEEE/IEC 62704-1 averaging technique for 1 g of tissue volume. The maximum SAR values were 6.14 W/kg and 50.93 W/kg at 200mW input power, with and without EBG respectively. Thus, in the EBG case, the maximum SAR was reduced by 90% compared to direct exposure from the antenna. The ICNIRP basic restrictions for electromagnetic field exposure from 100 kHz to 300 GHz, for averaging intervals 6 min Whole-body average SAR is 0.4 W/kg.

To further analyze the effectiveness of the EBG structure, the rear ground plane without an EBG element array is placed underneath the antenna. The proposed

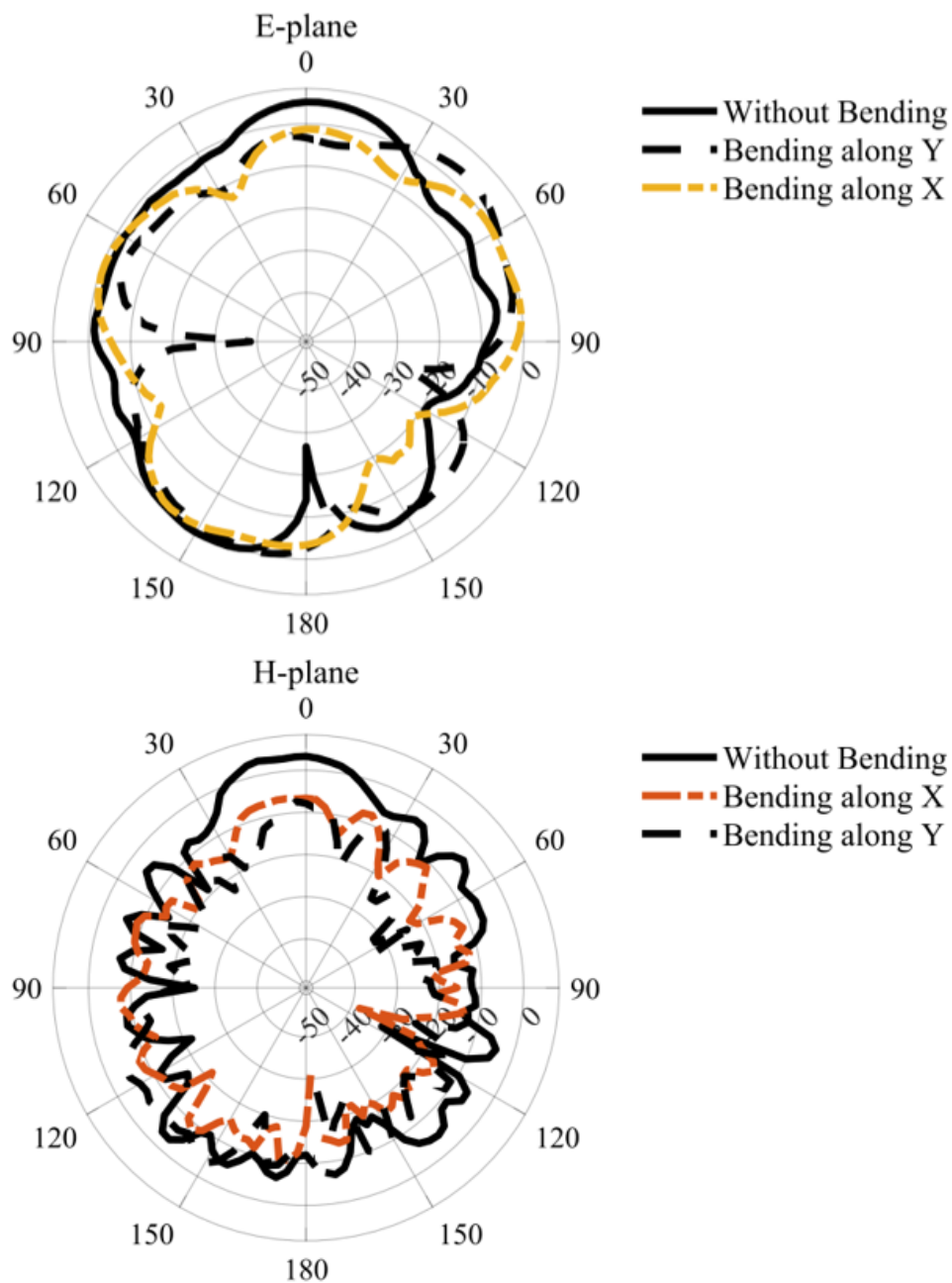


FIGURE 4.13: Measured radiation polar plots of EBG backed antenna (Fig. 4.6) when bent on 14 mm radius cylinder along X-axis (Red dash-line), Y-axis (orange dash-line) and without bending (solid-line) at 24 GHz

antenna becomes 3.57 mm thick to get the required reflection coefficient performance at 24 GHz and a significant decrease in the front-to-back ratio has also been observed.

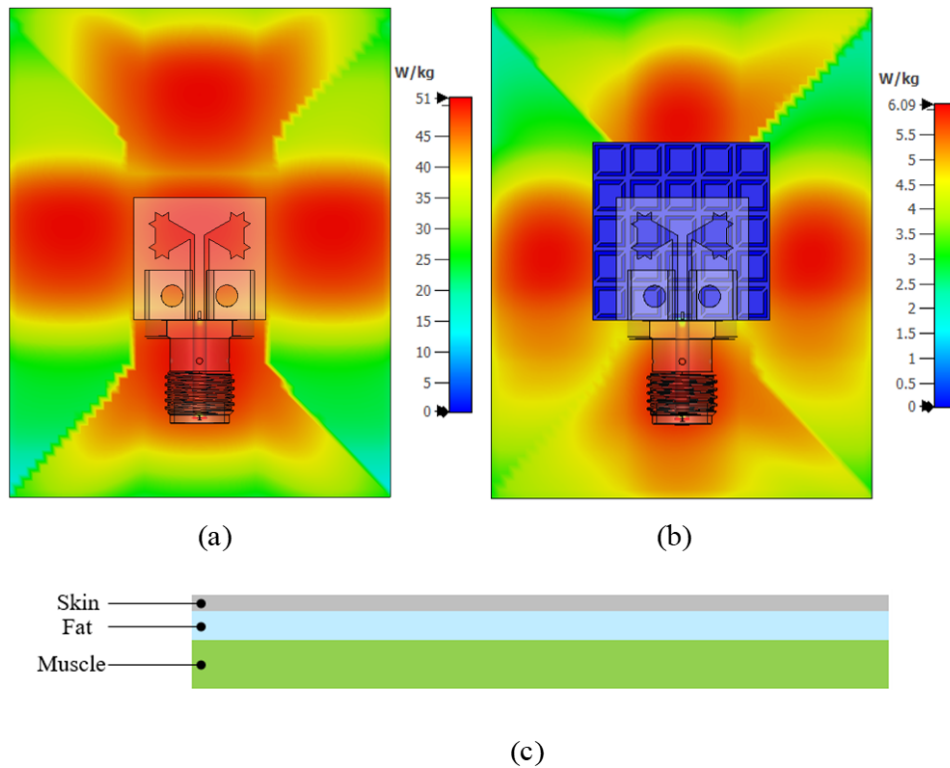


FIGURE 4.14: SAR distribution of prototype antenna (a) without EBG (b) with EBG (c) placement setting of tissues. Note, different scales are used in (a) and (b) owing to large variations in peak values.

TABLE 4.1: Material properties of skin, fat, muscle tissues at 24 GHz

Material	Dielectric Constant ϵ_r	Loss Tangent $\tan\delta$	Penetration depth(mm)	Conductivity (S/m)	Thickness (mm)
Skin	18.99	0.90073	1.097	22.841	1.5
Fat	3.84	0.29076	7.053	1.489	2
Muscle	27.39	0.80483	1.008	29.437	2.5

4.4 2nd Iteration Koch Fractal based Antenna Design and Integration with EBG Surface

The bandwidth of the 1st iteration fractal antenna has been further increased in the design (Section 4.3) by adding 2nd iteration fractal repetitions along the resonant length of the patch. The 2nd iteration of the Koch fractal geometry-based slotted bow-tie antenna is depicted in Fig.4.15. A fabricated prototype antenna uses a 127 μ m thick, polymer-based flexible substrate called Roger RT/duroid 5880.

The conductive components of the antenna are etched onto a $35\mu\text{m}$ thick copper cladding with an anticipated conductivity of $5.96 \times 10^7 \text{ S/m}$. The Rogers substrate has an estimated dielectric constant of 2.20 and a tangent loss of 9×10^{-4} within the operational frequency band. The antenna's design focuses on achieving flexibility by keeping the antenna height low, which results in reduced impedance bandwidth. Similar to the 1st iteration (Section 4.3), the 2nd iteration fractal bow-tie structure also features single metalization and dielectric layers, making ungrounded co-planar wave-guide feeding a suitable option for fabrication. After integrating the antenna with an EBG array, grounded CPW feeding was chosen as the EBG array includes a metal ground plane. To improve comparison with measurements, a female type 50Ω SMA edge mount connector (HRM(G)-300-467B-1 specified to 28 GHz) was simulated with the full structure using the CST time domain solver.

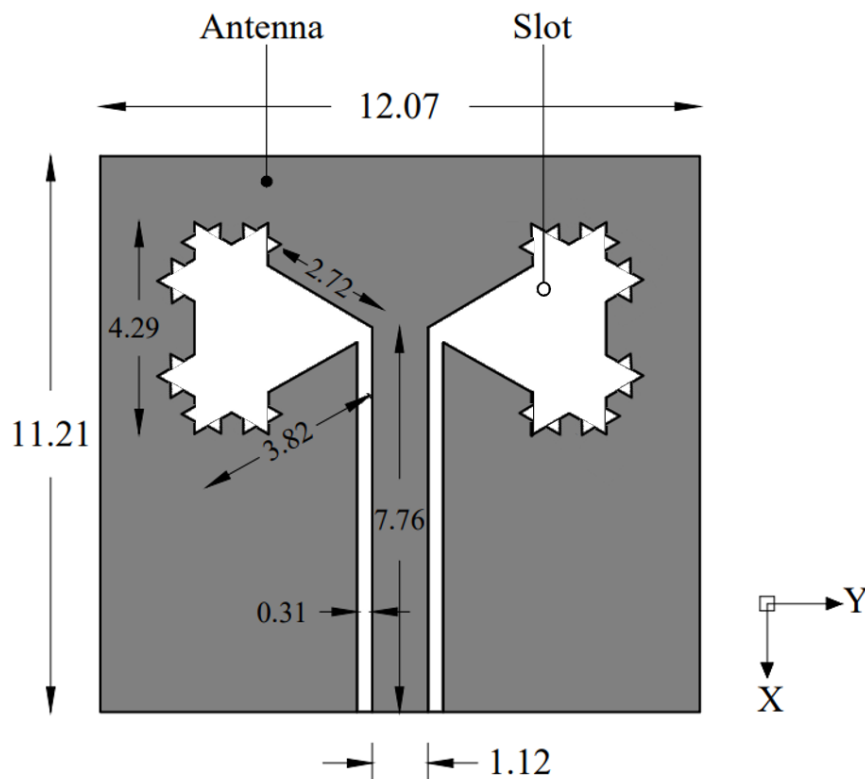


FIGURE 4.15: 2nd Iteration Koch fractal based Bow-tie slot antenna geometry

The integration of an EBG array with an antenna is an effective way to improve microstrip-based antenna performance. Similar to the 1st iteration fractal antenna (Section 4.2), a 5×5 EBG array was placed underneath the 2nd iteration fractal,

forming an antenna-EBG structure. The dielectric and metal layer stack of this structure is illustrated in Fig.4.16. This prototype features an edge-mounted connector, and there is no air gap between the EBG and the antenna. The EBG-backed 2nd iteration fractal antenna was also assessed for its isolation from the skin, which is an important parameter when designing antennas that will be worn on the body. As shown in Fig.4.17, the return loss performance of the 2nd iteration fractal EBG-backed antenna exhibits significant isolation from the skin. This means that the antenna design process was valid without accounting for body loading, and the antenna is suitable for use on the surface of the body.

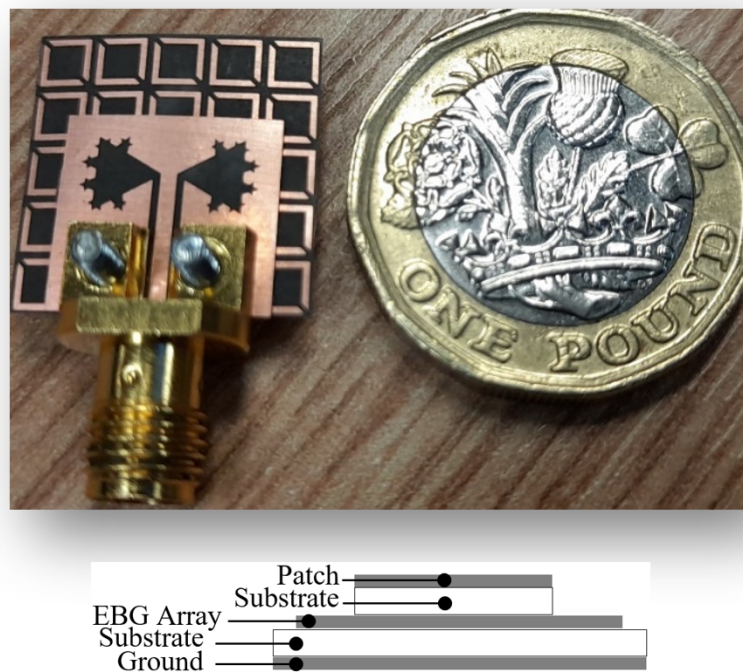


FIGURE 4.16: Integration of EBG with antenna

Additionally, this integration results in an ultra-thin antenna with overall dimensions of $16.19 \times 16.19 \times 0.254 \text{mm}^3$ (same as 1st Iteration). The compactness and thinness of the antenna is an essential factors when designing wearable technology, where users require lightweight, comfortable, and unobtrusive devices. Therefore, the integration of an EBG array with a proposed fractal geometry-based slot antenna is a promising technique for enhancing the antenna performance while maintaining a small form factor.

4.4.1 Results and Discussions

In this section, we present a comprehensive analysis of the 2nd Iteration fractal antenna design, which includes both simulated and measured results. The reflection coefficient, S_{11} , is evaluated to determine the impedance matching of the antenna. Additionally, the radiation patterns of the antenna are investigated, taking into account the effects of body loading and deformation.

4.4.1.1 Reflection Coefficient Evaluation

The 2nd iteration Koch fractal prototype was evaluated through in-house testing, and the reflection parameters were measured using a 65 GHz VNA (Anritsu 37397c). The results of the measurements are shown in Fig. 4.17, which demonstrates that the measured S_{11} values are less than -10 dB within the bandwidth of 3.02 GHz, ranging from 22.38 GHz to 25.4 GHz. This indicates that the proposed antenna has good impedance matching and can operate efficiently within this frequency range. To further evaluate the performance of the EBG-backed antenna, the simulated and measured reflection coefficient within the ISM band (24 - 24.250 GHz) is shown in the shaded bar in Fig.4.17. It is noteworthy that the reflection coefficient is below -15 dB, which indicates that the antenna has excellent reflection characteristics in the 24 GHz ISM band, making it suitable for applications within this frequency range.

Although the proposed structure is a wider band, the investigation is primarily focused on the 24 GHz ISM band application. Therefore, the additional performance that the antenna offers beyond this frequency range is not necessary for the proposed application. Overall, the results demonstrate that the EBG-backed antenna has a good impedance match and performs well within the desired frequency range, making it suitable for use in 24 GHz ISM band applications.

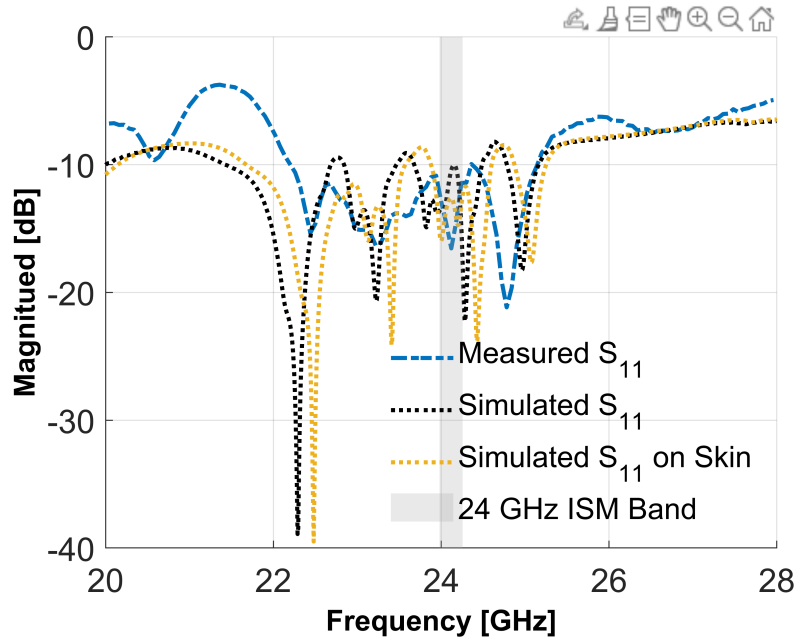


FIGURE 4.17: S_{11} of EBG backed antenna shown Fig.4.16

4.4.1.2 Far-Field Radiation Properties

To further evaluate the performance of the proposed 2nd iteration fractal-based EBG antenna, far-field radiation measurements were conducted in an anechoic chamber. The H- and E-plane polar plots with and without the EBG/AMC array structure at 24 GHz are presented in Fig.4.18 and 4.19. The results of these measurements demonstrated that placing the EBG/AMC structure beneath the antenna significantly suppressed the back lobe by 11.0 dB at 24 GHz while increasing the realized gain by 2.49 dB to 4.25 dBi at 24 GHz. These results show the efficacy of the EBG/AMC structure in reducing surface waves and deflecting radiation away from the human body. 2nd iteration fractal-based EBG antenna has more bandwidth and better performance under severe conformal deformation than 1st iteration.

Figs.4.18 and 4.19 present both actual and simulated radiation patterns on and off the skin. These patterns demonstrate that the EBG is effective in minimizing the skin loading effect, as the discrepancy at a specific angle in the back hemisphere is approximately 9.6 dB or less. This implies that the radiation pattern is relatively

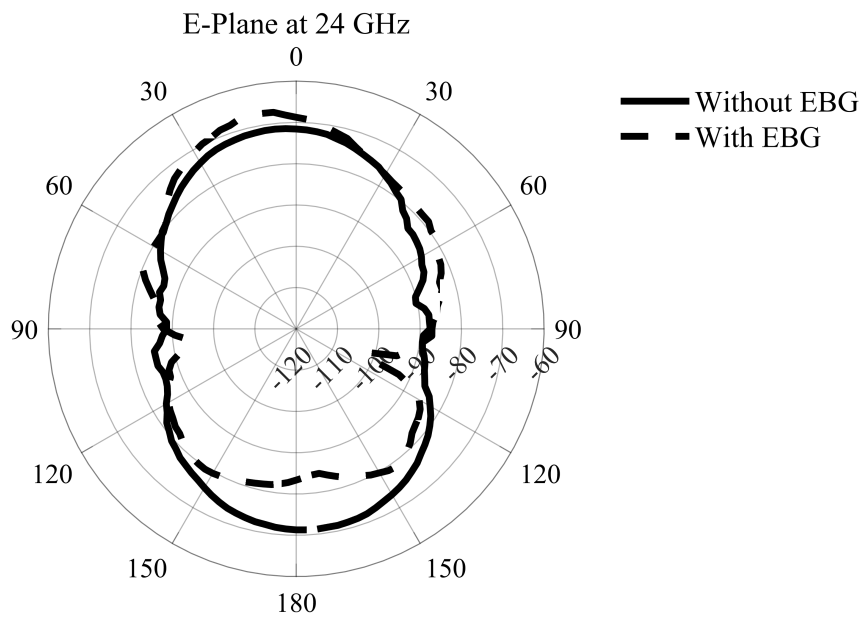


FIGURE 4.18: Measured and simulated E Plane radiation polar plots of EBG backed antenna shown Fig.4.16

insensitive to the presence of the human body, and the antenna can maintain a stable performance even when worn on the body.

4.4.1.3 On-body Performance

The proposed EBG (Section 4.2) in the antenna design helps to suppress backward radiation, making the prototype antenna more tolerant to human tissue loading. To test this, on-body measurements were conducted on various parts of a male volunteer's body, and the S_{11} of the human body-loaded antenna was plotted in Fig.4.20. The curves varied extremely due to differences in capacitive and dielectric constant values of human tissues at different mounting sites. However, except for the thigh, all measurements showed S_{11} below -10 dB over the desired 24 GHz ISM band, indicating good performance. Without the EBG/AMC, the antenna suffered from high losses and detuning across the entire band, as shown in Fig.4.20.

However, with the addition of the EBG/AMC, as seen in Fig.4.21, the structure is well-tuned for the ISM band at all mounting sites, and out-of-band loss decreased

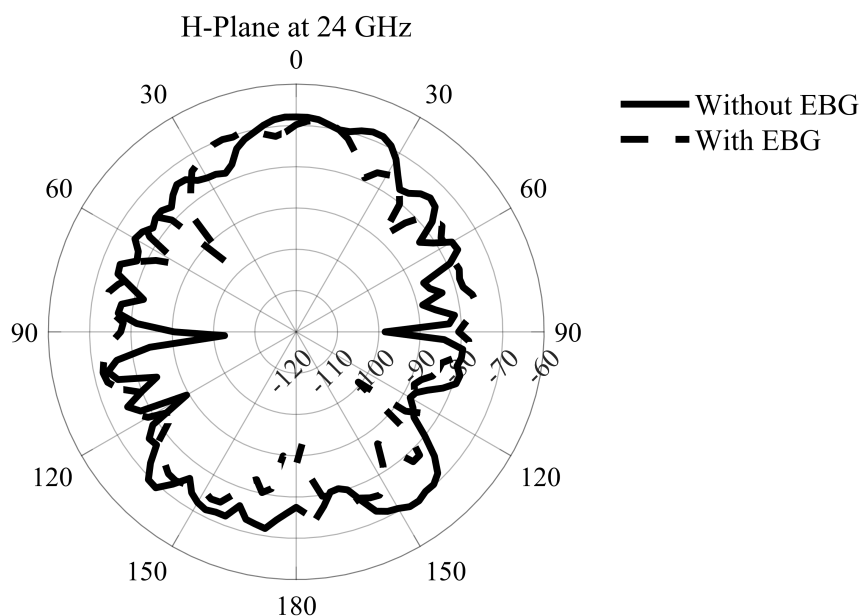


FIGURE 4.19: Measured and simulated H Plane radiation polar plots of EBG backed antenna shown Fig.4.16

by around 5 dB. The optimized EBG-backed Koch fractal bow-tie slot antenna not only covers the 24 GHz ISM band but also has a 3.2 GHz bandwidth, making it a suitable candidate for wearable applications in this frequency range. Therefore, this prototype antenna with a stable S_{11} response when attached to the body could be used in various wearable technologies that operate in the 24 GHz ISM band.

4.4.1.4 Structural Conformability

The antenna placement positions are relatively flat, but for on-skin mounting, it is important to have antennas that can withstand some structural deformation while maintaining good reflection and radiation performance that conforms to the curved surface of the body. Therefore, the prototype antenna was further investigated under bending conditions. Fig.4.22 shows the reflection coefficient measurements when the antenna is bent around a polyethylene foam cylinder along the X and Y axes separately. The dielectric constant of the available polyethylene is between

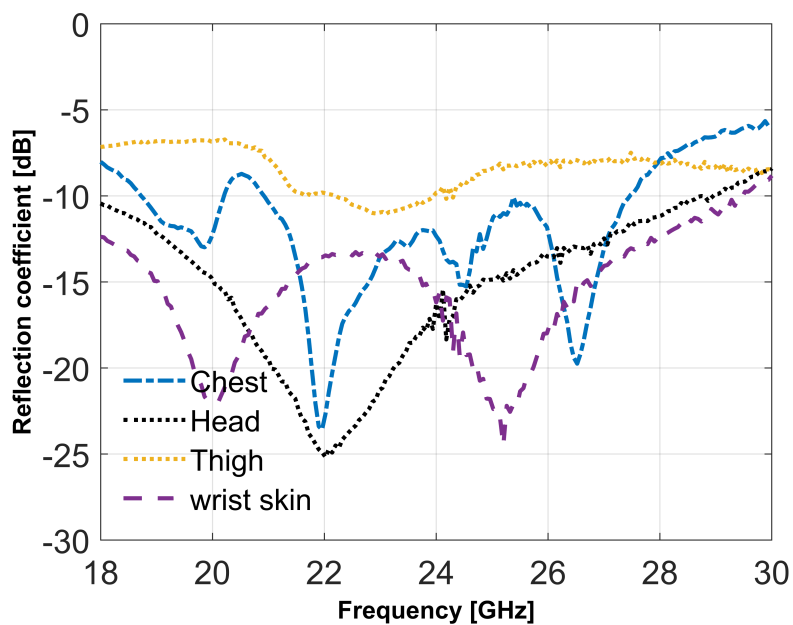


FIGURE 4.20: Measured reflection coefficients of the antenna (Fig.4.15) on the human body without EBG

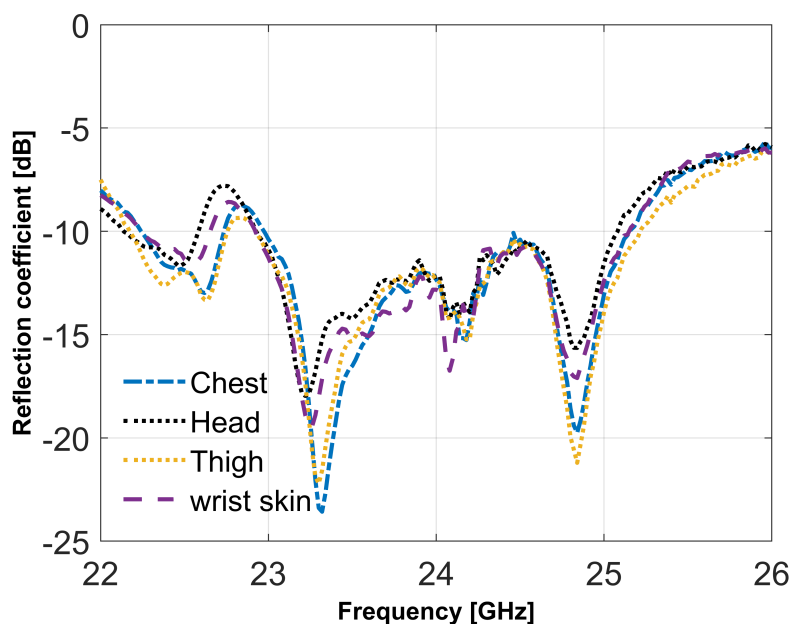


FIGURE 4.21: Measured reflection coefficients of the antenna (Fig.4.16) on the human body with EBG

1.3 and 1.6. As the antenna is not strongly loaded by the body, a tissue phantom was not used, and the curvature effect dominates.

A slight shift in center frequency can be noticed when the EBG-backed 2nd Iteration fractal antenna is bent along the X-axis, due to the reduction in resonant

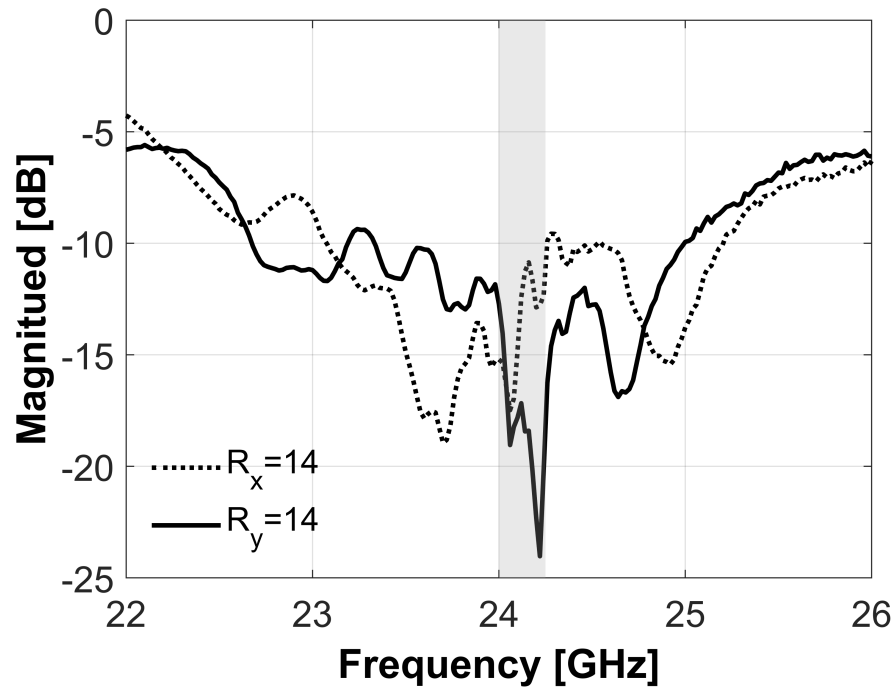


FIGURE 4.22: Reflection Coefficient of the EBG-backed antenna when bent on 14 mm radial cylinder along "Y" and "X" axis.

length caused by the bending. On the other hand, when bent along the Y-axis, a small detuning and a 260 MHz shift are observed. Despite having a 14 mm radius of curvature, the antenna still performs reasonably well in the 24 GHz ISM band, as depicted in Fig.4.22, with reflection coefficient values remaining below -10 dB. Additionally, Fig.4.23 shows the radiation patterns under bending for radii R_x and $R_y = 14$ mm along the Y- and X- axis. The directivity is approximately -2.96 dB for both axes of curvature. These results indicate that the optimized EBG-backed 2^{nd} iteration fractal antenna can tolerate some degree of bending while still maintaining good performance, which is crucial for on-skin mounting. Therefore, this antenna design can be used for wearable devices that require on-skin mounting and operate in the 24 GHz ISM band.

4.4.1.5 Specific Absorption Rate Evaluation

In order to assess the performance of the antenna in terms of specific absorption rate (SAR), a three-layer skin-fat-muscle model was used in CST MWS. The model

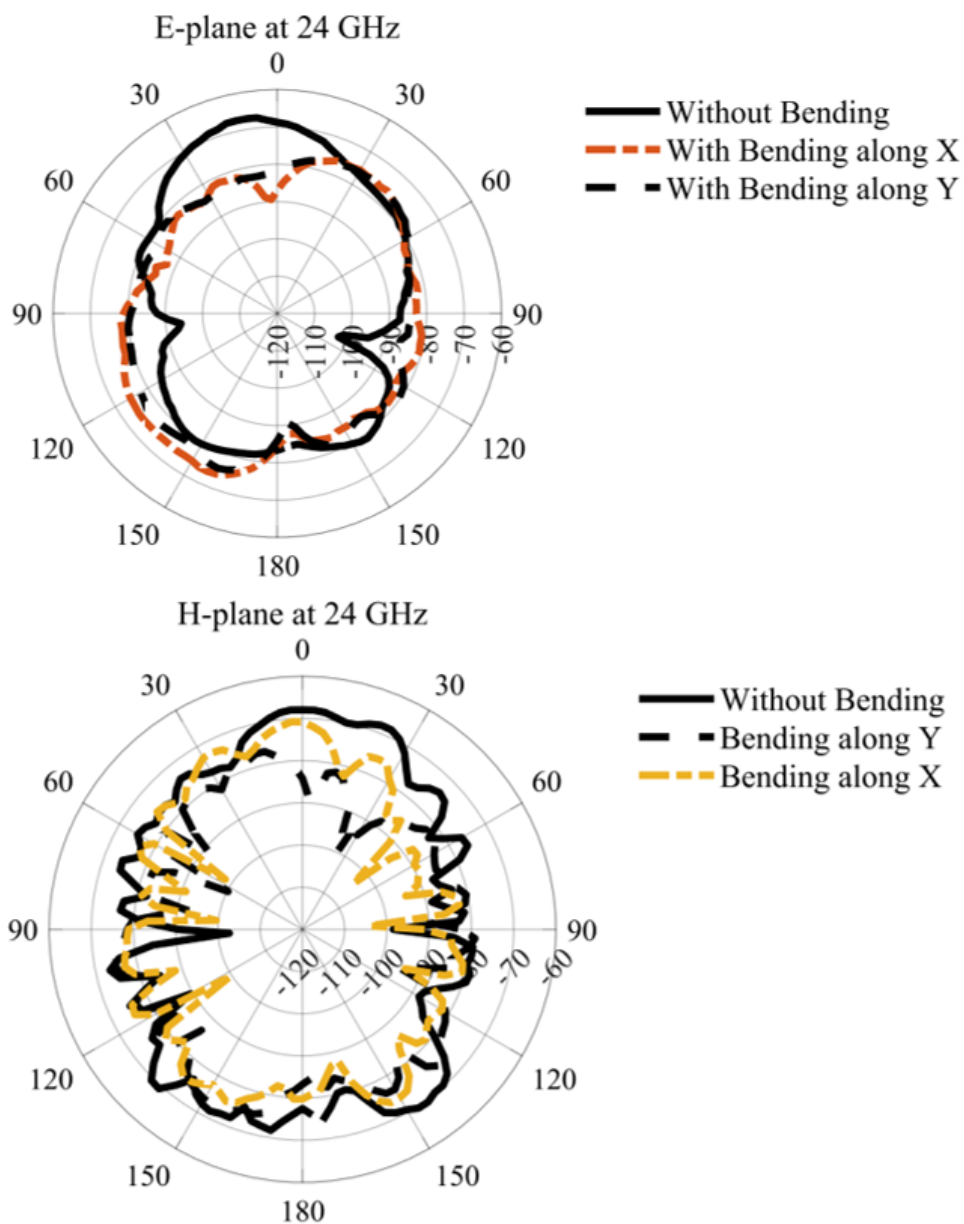


FIGURE 4.23: Measured radiation polar plots of EBG backed antenna (Fig.4.16) when bent on 14 mm radius cylinder along X-axis (Red dash-line), Y-axis (orange dash-line) and without bending (solid-line) at 24 GHz

consisted of dry skin, fat, and muscle layers, and the dielectric properties of each layer are mentioned in Table 4.1. The total size of the tissue model was $50 \times 30 \times 6 \text{ mm}^3$, and there was a 2mm gap between the skin and the EBG ground plane due to the connector height. The SAR distribution was obtained using the IEEE/IEC 62704-1 averaging technique for 1 g of tissue volume, and Fig.4.24 shows the results. The maximum SAR values were 4.68 W/kg and 35.2 W/kg at 200mW input power, respectively. Compared to direct exposure from the antenna,

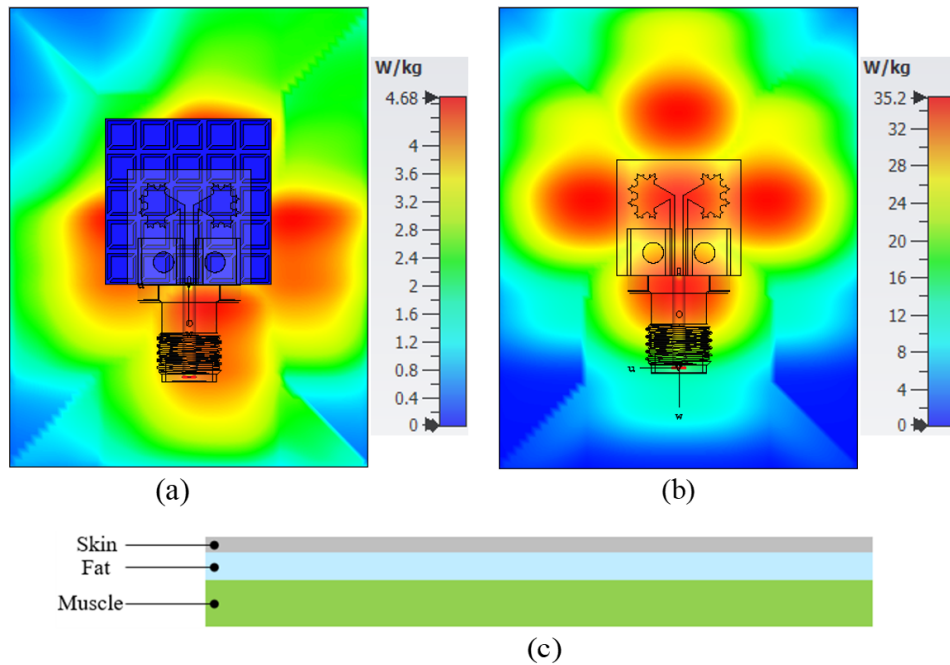


FIGURE 4.24: SAR distribution of prototype antenna (Fig.4.15)(a) without EBG (b) with EBG (c) placement setting of tissues. Note, different scales are used in (a) and (b) owing to large variations in peak values.

the EBG case reduced the maximum SAR by 87%. To evaluate the effectiveness of the EBG structure, the rear ground plane without an EBG element array was placed underneath the antenna. This resulted in a thicker structure, with a significant decrease in the front-to-back ratio. Therefore, the proposed EBG element is responsible for the ultra-thin structure of the antenna.

4.5 Conclusion

The chapter presents two novel, ultra-thin, and compact two-iteration Koch fractal antennas backed by an EBG structure that exhibits both AMC and EBG characteristics in the 24 GHz ISM band. To achieve this, a 5×5 element EBG array is evaluated beneath both Koch fractal bow-tie slot antennas, which are the thinnest ($0.02\lambda_0$) EBG-backed antennas reported in the K-band. Table 4.2 compares the proposed antenna's different features with previously published K-band EBG-integrated antennas, demonstrating that the proposed antennas are not only the thinnest but also the smallest in size.

TABLE 4.2: Comparison of proposed antenna (Fig. 4.15) with previously reported K-band EBG antennas

Ref	Freq. GHz	Dimension λ_0	Gain dBi	Antenna body gap	On- body S_{11} BW (GHz/%)	SAR decline	S_{11} shift MHz/ radii mm	FBR (Front to back ratio)
1st Iter.	24	1.29×1.29 $\times 0.02$	5.08	On Skin	2.7/ 11.3%	90%	400/14	14.9 dB
2nd Iter.	24	1.29×1.29 $\times 0.02$	4.25	On Skin	3.2/ 13.3%	87%	260/14	13.5 dB
[15]	26	2.79×1.91 $\times 0.032$	8.65	On Skin	0.6/ 2.3%	69.9%	400/30	2 dB
[16]	28	2.67×3.14 $\times 0.07$	7.90	Adhesive Fabric	10/ 40%	N/A	1500/30	15 dB
[17]	24	2.16×2.16 $\times 0.05$	6	Fabric	0.7/ 3%	N/A	400/30	9.9 dB
[18]	28	1.9×1.9 $\times 0.14$	5.2	N/A	0.9/ 3.3%	N/A	N/A	N/A

The proposed antennas have several key features that make them suitable for on-skin mounting in WBAN applications. The 1st and 2nd iteration fractal structure exhibits a large bandwidth of 11.25% and 13.3%, when attached directly to the skin. Additionally, the proposed antennas show a minimal shift in S_{11} while bending, making them more resistant to deformation while still maintaining good performance. They also have a high front-to-back ratio (FBR), indicating that they can transmit and receive signals more effectively away from the body. Finally, the proposed EBG-backed Koch fractal geometry-based antennas are shown to reduce SAR by 90% and 87% compared to direct exposure from the antennas, making them safe for use in close proximity to the human body.

The anechoic chamber measurements of the EBG-backed Koch fractal geometry-based antennas also show significant improvements in gain and front-to-back ratio, with a gain increase of 2.3 dB and 1.9 dB, respectively and a front-to-back ratio increase of 14.9 dB and 13.5 dB. The return loss performance of the 2nd iteration fractal antenna with EBG while attached to the human skin is better than the 1st

iteration fractal antenna, showing better insensitivity to body proximity.

Moreover, when the EBG-backed antennas are subjected to structural deformation over a curve of 14 mm radius, the 2nd iteration fractal antenna shows slight detuning (260 MHz) of the center frequency and insignificant variation in bandwidth. On the other hand, the 1st iteration fractal antenna shows slight detuning (260 MHz) of the center frequency. The radiation pattern of the curved EBG antennas also exhibits reasonable directivity and gain of -2.1 dB and -2.8 under bending.

Overall, the proposed EBG-backed 1st iteration Koch fractal antenna structures exhibit excellent performance characteristics, making them highly suitable for on-skin mounting in WBAN applications, especially in the 24 GHz ISM band.

References

- [1] Aun, Nur Farahiyah Mohamad, et al.: "Revolutionizing wearables for 5G: 5G technologies: Recent developments and future perspectives for wearable devices and antennas", *IEEE Microwave Magazine*, 18 (3), 108-124, 2017.
- [2] Ali, Mubasher, et al.: "Multiband ultra-thin flexible on-body transceivers for wearable health informatics," *Australasian physical engineering sciences in medicine*, 423-63, 2019.
- [3] Attia, Hussein, M. Lamine Abdelghani, and Tayeb A. Denidni.: "Wideband and high-gain millimeter-wave antenna based on FSS Fabry–Perot cavity", *IEEE transactions on antennas and propagation*, 65 (10), 5589-5594, 2017.
- [4] Ukkonen, Leena, Lauri Sydänheimo, and Yahya Rahmat-Samii.: 'Embroidered textile antennas for wireless body-centric communication and sensing.' *Loughborough Antennas Propagation Conference (LAPC)*. *IEEE*, 2015.
- [5] Arif, Ali, et al.: "A compact, low-profile fractal antenna for wearable on-body WBAN applications", *IEEE Antennas and Wireless Propagation Letters*, 18 (5), 981-985, 2019.
- [6] Tehrani, Bijan K., Benjamin S. Cook, and Manos M. Tentzeris.: "Inkjet printing of multilayer millimeter-wave Yagi-Uda antennas on flexible substrates", *IEEE Antennas and Wireless Propagation Letters*, 15, 143-146, 2015.
- [7] Chahat, Nacer, et al.: "Wearable endfire textile antenna for on-body communications at 60 GHz", *IEEE Antennas and Wireless Propagation Letters*, 11, 799-802, 2012.

-
- [8] Wang, Mengjun, et al.: "Investigation of SAR reduction using flexible antenna with metamaterial structure in wireless body area network", *IEEE Transactions on Antennas and Propagation*, 66(6), 3076-3086, 2018.
- [9] Wu, Ting, et al.: "The Human Body and Millimeter-Wave Wireless Communication Systems: Interactions and Implications," *IEEE International Conference on Communications (ICC)*, 2015, pp. 2423-2429.
- [10] Das, Rupam, and Hyongsuk Yoo.: "Application of a compact electromagnetic bandgap array in a phone case for suppression of mobile phone radiation exposure," *IEEE Transactions on Microwave Theory and Techniques*, 66 (5), 2363-2372, 2018.
- [11] Lin, Xiaoyou, et al.: "Flexible fractal electromagnetic bandgap for millimeter-wave wearable antennas," *IEEE Antennas and Wireless Propagation Letters*, 17 (7), 1281-1285, 2018.
- [12] Ali, M., et al.: "Ultra-thin electromagnetic band gap backed fractal geometry-based antenna for 24 GHz ISM band WBAN.," *IET Microw. Antennas Propag.* 17(3),216–222, 2023.
- [13] Soliman, E. A., et al.: "Bow-tie slot antenna fed by CPW," *Electronics letters*, 35 (7), 514-515, 1999.
- [14] Andreuccetti, D. et al: "An Internet resource for the calculation of the dielectric properties of body tissues in the frequency range 10 Hz-100 GHz." 2012.
- [15] Wissem, EL May, et al.: "A textile EBG-based antenna for future 5G-IoT millimeter-wave applications", *Electronics*, 10(2), 154, 2021.
- [16] Lin, Xiaoyou, et al.: "Flexible fractal electromagnetic bandgap for millimeter-wave wearable antennas", *IEEE Antennas and Wireless Propagation Letters*, 17 (7), 1281-1285, 2018.

- [17] Iqbal, Amjad, et al.: "Electromagnetic bandgap backed millimeter-wave MIMO antenna for wearable applications", *IEEE Access*, 7, 111135-111144, 2019.
- [18] Ashraf, Nadeem, et al.: '28/38-GHz dual-band millimeter wave SIW array antenna with EBG structures for 5G applications', *international conference on information and communication technology research (ICTRC)*. IEEE, 2015.
- [19] H. Zhou and F. Xu, "Artificial magnetic conductor and its application," *Proceedings of the International Symposium on Antennas Propagation*, Nanjing, China, 2013, pp. 1110-1113.

Chapter 5

Empirical propagation path loss model for on-body communication at 24 GHz ISM band

5.1 Introduction

Body-centric wireless communication networks can have a direct and great impact on the socio-economic betterment of society. Therefore, on-body propagation studies attract substantial attention and recognition in both academic and industrial communities [1] - [3]. In general indoor/outdoor wireless communication, the human body is only taken into account as a source of fading and electromagnetic scattering. On the other hand, in on-body or body-centric wireless communication networks (BCWNs), the surface of the human body is used as a transmission medium or path for electromagnetic waves [4] - [6]. BCWNs are an attractive low-cost solution that can be used in healthcare, sports, and lifestyle monitoring applications enabling constant health screening and access to patients regardless

of their current location or activity. Devices like ECG (Electrocardiogram) monitors, pulse oximeters, blood pressure sensors, insulin pumps, and blood glucose monitors can be coupled with wireless and wearable communication devices. Many BCWN antennas and on-body propagation studies have been focused on the 2.4 GHz, 5.8 GHz, and UWBs (Ultra Wide Bands) [1], [7] - [9].

Greater bandwidth is needed for some body-centric wireless applications, such as real-time transmissions of uncompressed HD (High-definition) video [10]. Exploring a higher frequency band for BCWNs is crucial because the frequency band below 10 GHz is already crowded. For high-speed wireless communications, it is desirable to use the mmWave (millimeter wave) frequency bands; e.g. the 24, 28, and 38 GHz bands are suitable candidates for BCWNs. At 2.45 GHz, the free space attenuation across a 50 cm link is 34 dB; at 24 GHz, 60 GHz, and 94 GHz, it is 54 dB, 62 dB, and 66 dB, respectively. Due to this higher path loss at mmWave frequencies compared to microwave frequencies, security is enhanced. This crucial property enables the confinement of wave propagation in close proximity to the human body, limiting the possibility of system interference and, in the case of military and defense applications, lowering the risk of interception by hostile forces [11]. On-body mmWave BCWNs face challenges: first, substantial propagation attenuation is experienced, caused by both high free-space attenuation and low mmWave diffraction and penetration capability. These factors limit the radio signal's ability to propagate around obstacles and bend around the edges of the human body, leading to signal blockage and reduced communication range. The dispersive nature of human tissue can cause signal distortion, which may further affect the accuracy of the channel characterisation. Dispersion can result in frequency-dependent signal attenuation, phase shifts, and delay, which can cause signal distortion, such as inter-symbol interference, and affect the signal-to-noise ratio. The human body poses a scattering medium with extremely large electrical dimensions due to the short wavelength at mmWaves. As a result, massive fades due to shadowing effects are introduced. Due to the preceding reasons, mmWave propagation may be highly attenuated in the on-body environment. Furthermore,

as demonstrated by [12] - [13], The curvature of the surface of the human body can have a significant impact on the performance of wireless communication channels. Furthermore, the frequencies, 24 GHz, 60 GHz, and 94 GHz are of special interest to BCWNS because widespread use is likely to be encouraged by the possibility of license-free operation. Propagation losses in free space for various separations relevant to body-centric systems operating at 24 GHz have been calculated using Matlab [14], as shown in Table 5.1. On the other hand, despite the fact that atmospheric absorption rises with frequency [15], it is not significant to the on-body link at the distances being considered. In order to plan reliable mmWave BCWNS, the propagation channel's characterisation is critically required. So far, full-wave simulations based on the finite-difference time-domain (FDTD) approach and measurement campaigns have been the major techniques used to model the propagation channel up to the X band [16], [17] - [22].

TABLE 5.1: Free space path loss and Atmospheric absorption at 24 GHz
Vapor density = $8g/m^3$, Air pressure = $102 \times 10^5 Kpa$, Temperature = $23^\circ C$

Distance (cm)	Free Space Path Loss (dB)	Atmospheric Absorption (dB)
30	49.59	5.60×10^{-5}
50	54.02	9.34×10^{-5}
100	60.04	1.87×10^{-4}
150	63.54	2.80×10^{-4}
200	66.06	3.74×10^{-4}

In this chapter, The objective is to conduct a preliminary study to determine the path loss for on-body communication at the 24 GHz ISM band. Additionally, the study aims to assess the difference between LOS (line-of-sight), partial LOS, and NLOS (non-line-of-sight) links by dividing the waist-to-torso receiver grid into three distinct zones. As the antenna plays a crucial role in any communication system, so its effect is quite often not separable from the propagation channel. Therefore, the study incorporates antenna effects in this 24 GHz ISM band on-body propagation channel over waist-to-torso links using four different antennas. The

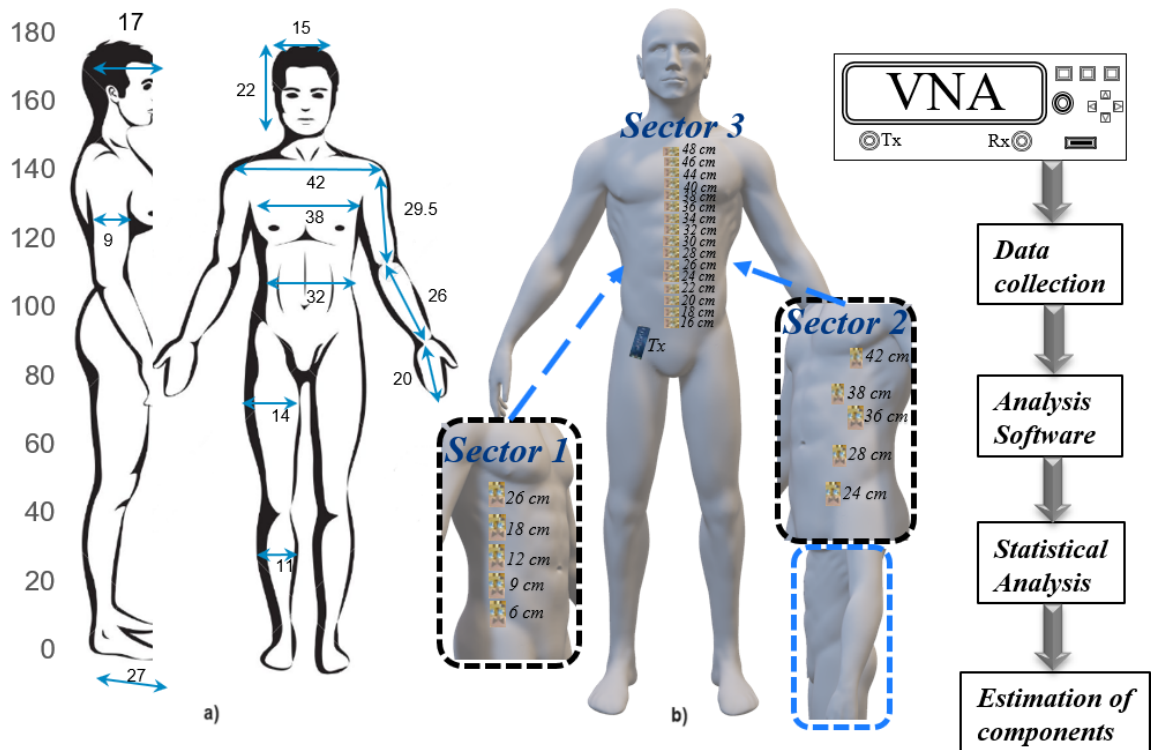


FIGURE 5.1: (a) Dimension of the body used in propagation measurements, (b) Locations of transmitter and receiver antennas for on-body channel characterisation campaign

receiver was placed in various positions on the chest area during a measurement campaign, and the results were compared to those using different radiation pattern antennas in the same setting.

This study aims to enhance the accuracy and robustness of the results by thoroughly examining the sensitivity of the receiver locations in the waist-to-torso link. Measured results will be presented that evaluate the effects of non and partial line-of-sight link losses by utilising three different grids. The findings are discussed in detail, shedding light on the impact of these losses on the system's performance. Section II provides experimental characterisation which includes the measurement setup, antenna development, and performance measurement. Section III provides details on the measurement campaign that has been performed on the channels under investigation along with a statistical analysis of measured data. Section III further estimates the path loss components and presents the comparison of all 4 cases of different transmitter antennas. Finally, the last section compiles the conclusion, presenting key findings.

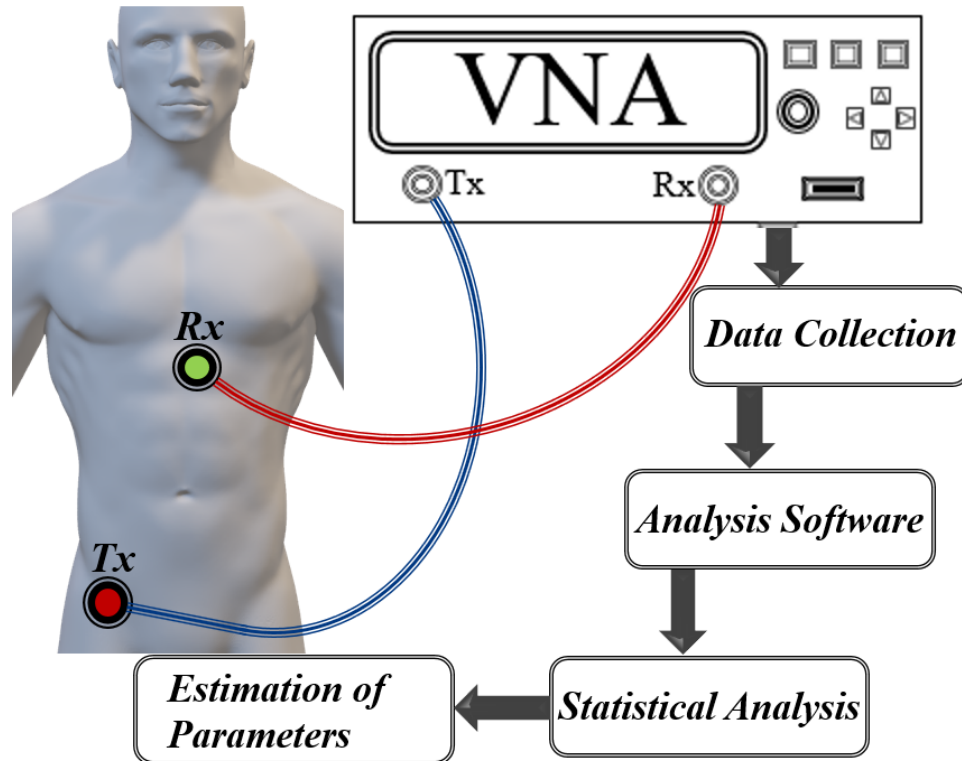


FIGURE 5.2: Measurement setup including post-processing steps.

5.2 Experimental Characterisation

This section describes the measurement setup and summarises the steps of the post-processing evaluation campaign. The rest of the discussion is on the structure of antennas and their on-body performance.

5.2.1 Frequency Domain Measurement Configuration

Fig.5.1 presents the dimensions of the volunteer body, and three grids of 15, 20, and 10 receiving probes, respectively, have been placed on the torso, where each grid is designed to conform to the shape of the body surface. The distance between each receiving point to others (in the same grid) on the body is 2 cm. In accordance with Fig.5.1b, the transmitter is positioned on the right side of the belt, and the receivers are positioned in the torso region, parallel to the body. Fig.5.1b illustrates the detailed grids and identifies three sectors, which represent the non-line-of-sight (NLoS), partial line-of-sight (PLoS), and line-of-sight (LoS) pathways

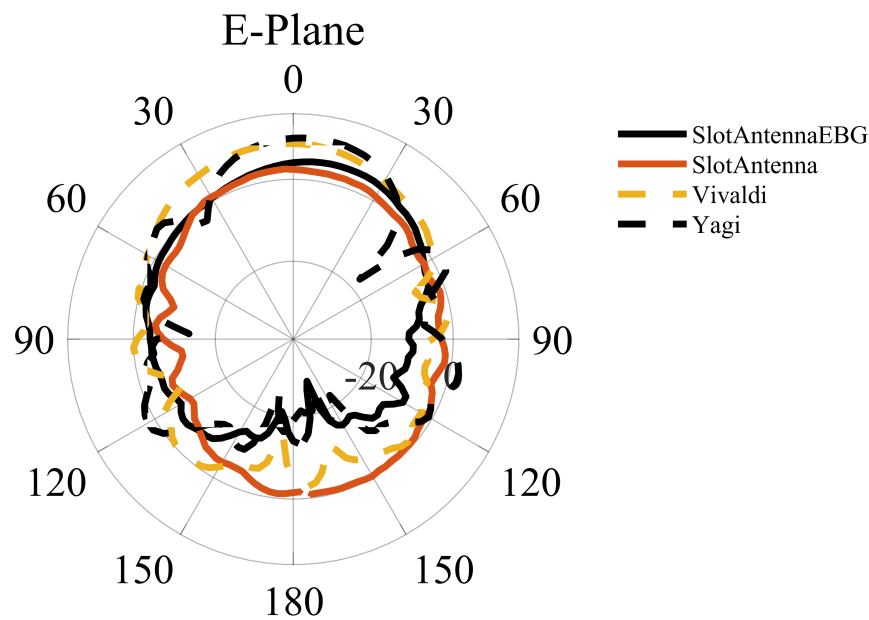


FIGURE 5.3: E-plane Radiation Pattern of antennas

involved in the waist-to-torso communication link: Sector I represents the LoS link, Sector II represents the PLoS link, and Sector III represents the NLoS link. An Anritsu-37397c vector network analyser (VNA) is used to measure the S_{21} parameter between two antennas placed at various positions on a human body as shown in Fig.5.2. Two flexible SMA coaxial cables with a two-meter length were used to link the antennas to the VNA. The attached VNA has a -90 dBm noise floor and -7 dBm transmit power.

Measurement sweeps are performed between 22 to 26 GHz with 801 points and a setting of 100 Hz IF bandwidth. Four sweeps are performed for each receiving point and the average is taken of the four measured values. The separation between the body and the antenna substantially affects the path loss and therefore must be closely monitored. The separation is adjusted by attaching the antenna using a 1 mm thick piece of fabric between the antenna and the body. The antenna is attached to this fabric using tape and held against the body using elastic bands to prevent movement during measurements. The measurements were taken in the different grid positions along the vertical axis of the torso (as shown in Fig.5.1b) and all channel parameters were obtained from these measurements.

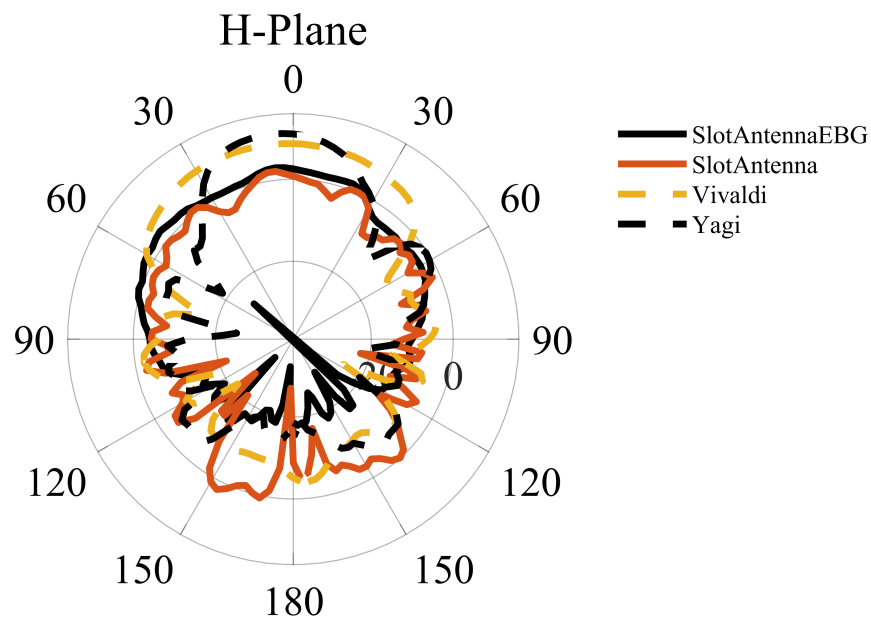


FIGURE 5.4: H-Plane Radiation Pattern of antennas

Four types of transmitter and two types of receiver antennas have been used and placed in the positions shown in Fig.5.1b. The chosen four types of antennas cover the characteristics of microstrip antennas that have the potential to be used in on-body wireless sensor networks. These characteristics include omnidirectional, directional, wide beam directional, and suppressed back lobe radiation patterns. Receiver nodes in current WBAN medium access schemes are required to either communicate with or sense the presence of other receiver nodes. Therefore, to enable receiving nodes to communicate with surrounding nodes, a non-directional pattern is selected for the receiver antenna.

All measurements were performed in a large room environment to ensure that reflections are received later than the components diffracting around the body. Due to the body's curvature, the measured data were gathered on a conformal grid. Fig.5.2 depicts the measuring setup for a single channel with a human participant. The minimum distance between two antennas to achieve minimum mutual coupling is typically around one-fifth of the operating frequency's wavelength. For example, in this study, the low-frequency limit in the 24 GHz ISM band has a wavelength of 1.25 cm, and the minimum distance between two antennas to minimize mutual

coupling is approximately 0.25 cm. To ensure avoidance of the mutual coupling effect in Sector 1, a minimum measurement distance of 3 cm has been chosen between the transmitter and receiver antenna's mutual coupling.

5.2.2 Antennas

Body-worn antennas should be miniaturized as far as possible to integrate with flexible and body-wearable transceivers. The human tissue's lossy and dispersive behaviour at mmWaves can impact antenna performance. Therefore, for a wearable antenna to be effective, it should have high efficiency and be minimally affected by the presence of the human body. Additionally, it should transmit minimal energy to the human skin to avoid any adverse effects. To meet the requirements of wearable applications, the antenna should also be lightweight, flexible, and conformable, allowing for comfortable use and mobility. Restrictions on high transmission power and increased path loss due to high atmospheric attenuation at mmWave frequencies enforces use of medium-gain (10dBi) antennas rather than low gain as the high gain microstrip-based antennas will increase radiations towards human skin [23].

Microstrip patch antennas are favored for body-centric communication due to their small size and planar structure, which makes them suitable to be integrated into wearable devices and attached to different body parts. Four different types of antennas were used to characterise the channel, each with its own unique radiation pattern. It is expected that these antennas will have varying effects on the radio channels, especially in body area networks where human skin tissue can affect the antenna's capacitive behavior. Therefore, it is necessary to characterise the radiation field of each antenna.

At the mmWaves frequencies band, input feeding lines cause spurious waves which severely impact radiation patterns. Therefore, the influence of input excitation should also be considered in the design with EBG structure and analysed when placed on the human body [24]. Three types of printed antenna are defined: (1)

a Yagi Uda array antenna, (2) a Vivaldi antenna (3) a CPW-based bow-tie slot antenna. These antennas and the EBG structures (presented in Chapter 3) were fabricated on Duroid 5880 substrate ($h=127 \mu\text{m}$, $\epsilon_r = 2.2$, $\tan\delta = 0.0009$). The 4th antenna comprises the bow tie with an EBG backplane for suppressing the back lobe and improving radiation efficiency. The Yagi Uda and Vivaldi antennas were selected as they have forward gain radiation patterns, with the Vivaldi antenna having a wider beam width than the Yagi antenna. On the other hand, a Bow tie slot antenna is low gain and omnidirectional.

The two forward gain antennas, Yagi Uda, and Vivaldi antenna are used as transmitter antennas. The Yagi Uda is a medium gain linearly polarised antenna. The design, development, and detailed performance of the antennas are presented in Chapter 3. The Yagi Uda demonstrates a gain of 10 to 12 dBi. On the other hand, the Vivaldi antenna exhibits a bandwidth of 2.15 GHz in terms of the on-body reflection coefficient. Chapter 3 includes the measured radiation pattern, where the realized gain of the Vivaldi antenna is approximately 7 dBi.

As a receiver antenna, a bow tie slot antenna either with or without EBG can be employed. In Chapter 3, the results demonstrated that the integration of the EBG increases the antenna's front-lobe gain by 2.6 dB, and reduces back-lobe radiation by 12.2 dB, thereby greatly reducing the radiation that would be absorbed by a human wearer [25], [25]. S_{11} measurements were taken on a male volunteer to determine the body-loading performance of the prototype antenna. Without an EBG, a significant amount of energy is lost in human tissues as all the reflection curves are detuned even though the observed S_{11} was below -10 dB over the desired 24 GHz ISM band (as presented in [26]). Therefore, The reflection response of the EBG structure is optimized (as explained in Chapter 3) for the 24GHz ISM band for all mounting sites after integration with the antenna. The prototype antenna has a 600 MHz bandwidth with a 5.2dBi gain.

Fig.5.3 and 5.4 depict the far-field E-Plane and H-Plane radiation patterns of all four antennas. During the measurement campaign, the antennas were placed parallel to the body with their main radiating elements facing away from the body.

Table 5.2 presents the radiation characteristics of the transmitter and receiver antennas, as well as their configurations for the channel measurements. To ensure full coverage of the torso portion in a sensor network, the transmitter or sink node requires a medium gain antenna. Therefore, the antennas with a forward radiation pattern and medium gain were used as transmitter antennas, while the antennas with an omnidirectional pattern were used as receiver antennas.

TABLE 5.2: Transmit Receive antennas configuration for channel measurements

Case#	Transmitter antenna	Tx Radiation direction	Receiver antenna	Rx Radiation direction
1	Bow-tie Slot	broadside	Bow-tie Slot	broadside
2	quasi-Yagi Uda array	Directional, End fire	Bow-tie Slot	broadside
3	Vivaldi	Directional, Wide-beam	Bow-tie Slot	broadside
4	Vivaldi	Directional, Wide-beam	EBG backed Bow-tie Slot	broadside, back-lobe suppressed

5.3 Path Loss Model and Data Analysis

The system configuration displayed in Fig.5.2 was employed to measure the path loss for the links described. In Section 5.2.1, the setup for each channel link in waist-to-torso communication was explained. The torso portion was divided into

three sectors to examine the behavior of all different paths, with the link between the transmitter and each sector varying in terms of line of sight (LoS) visibility. The measured channel data for several on-body scenarios were further analysed and processed in the statistical analysis software MATLAB to develop preliminary statistical models for path loss. However, currently, the on-body empirical and theoretical propagation models for 24 GHz are not established, making it difficult to compare the validity and applicability of the presented model. The propagation of the channel has been investigated in terms of path loss exponent and shadowing factor according to the following model [27] - [28]:

$$P_L(d) = P_L(d_0) + 10n \log \frac{d}{d_0} + \chi(0, \sigma) \quad (5.1)$$

where n is the path loss exponent, $\chi(0, \sigma)$ is a random variable taken from a normal distribution with zero expectation and a standard deviation σ , and $P_L(d_0)$ is the measured path loss at the reference distance d_0 between the transmitter and receiver.

In equation (5.1), the path loss exponent is expected to have a larger value than it has in a free-space environment due to the presence of scatterers and obstructions. Four sets of measured data, which correspond to four types of transmitter and receiver antenna configurations listed in Table 5.2, have been obtained. In each case, the path loss exponent and deviation shadowing factor will be estimated.

5.3.1 Case 1

In the first case, both the transmitter and receiver antennas are bow-tie slot antennas to investigate the impact of omnidirectional radiation around the body. Due to the omnidirectional pattern, the gain is low. The measurements have been carried out considering a minimum distance (d_0) of 6 cm, 20 cm, and 16 cm in sector 1, sector 2, and sector 3, respectively (as illustrated in Fig.5.1b). The reason behind having three different reference distances is two-fold. Firstly, it is because each sector boundary, defined in Fig.5.1b, starts at a specific distance from the

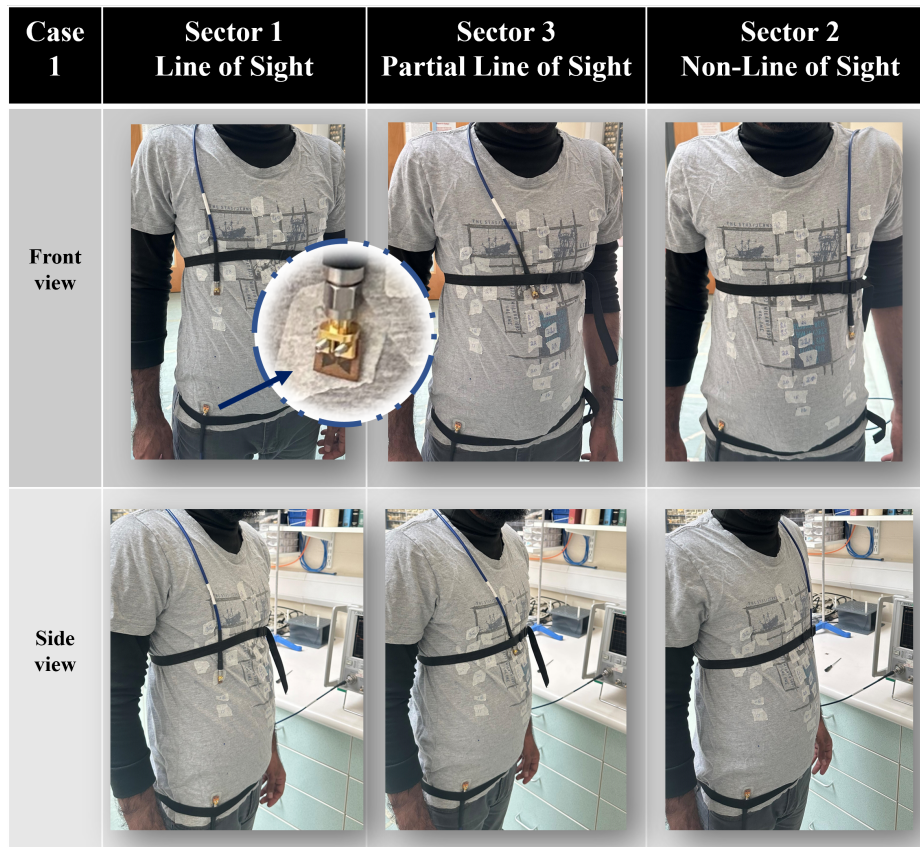


FIGURE 5.5: Measurement setup on a human subject in case 1 with front and side view

transmitter antenna which is located on the left side of the waist. Secondly, the size of the antennas used in the measurement settings while choosing the reference distance is taken into account to ensure minimal mutual coupling, which is dependent on both the antenna size and its location on the grid. Fig.5.5 illustrates the measurement setup for the waist-to-torso link on a human subject in case 1, providing both a front view and a side view. The purpose of this setup is to capture the body curvature and shows the line-of-sight angle between the transmit and receive antennas. In Fig.5.6, the measured path loss data for three frequencies (24, 24.125, 24.25 GHz) across different sectors of the waist-torso link has been plotted. The measurements provide a comprehensive view of the variation in path loss across the whole range of ISM band frequencies at each distance. Due to the sensitivity of the instruments and the noise floor of the VNA, path loss contributions higher than 90 dB (highlighted in green) have not been plotted. This ensures that only reliable data is included in the analysis and that any potential errors or

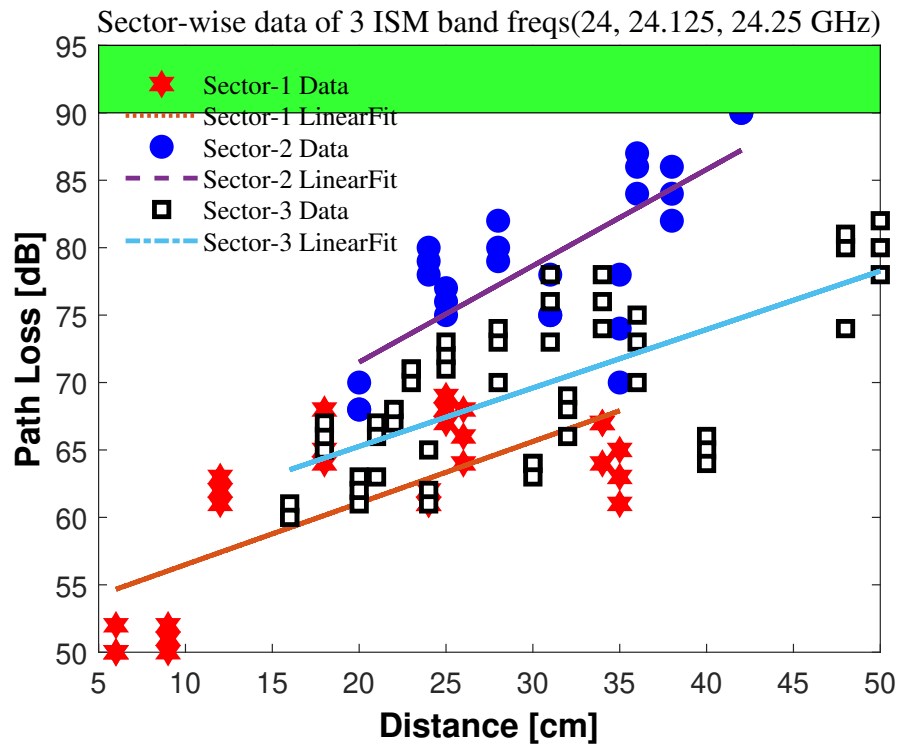


FIGURE 5.6: Linear regression on measured path loss data (case 1) at 3 frequencies sector-wise data covering complete band

outliers are removed.

Fig.5.7 presents sector-wise measured path loss data of a single frequency (24 GHz). For all 3 sectors, the mean path loss with reference to distance can be found through curve-fitting. A linear regression analysis has been applied to the measured path loss data to calculate the path loss exponent. The calculated path loss exponent for sector 1 (line of sight) is 2.42, and for sector 3 it is 3.75. However, for sector 2 (which is non-line of sight), the coefficient in equation (5.1) is 5.12. The higher coefficient value in sector 2 can be attributed to the limited penetration of K-band wavelengths through the human skin, which results in greater path loss compared to sector 1.

To further analyse the data, The cumulative distribution function (CDF) of the shadowing factor against the path loss deviation is plotted in Fig.5.8, to determine the probabilities of different levels of path loss deviation and can help identify the most likely path loss values for a given scenario. Fig.5.8 displays the cumulative distribution function (CDF) of the (shadowing data) shadowing factor $\chi(0,\sigma)$,

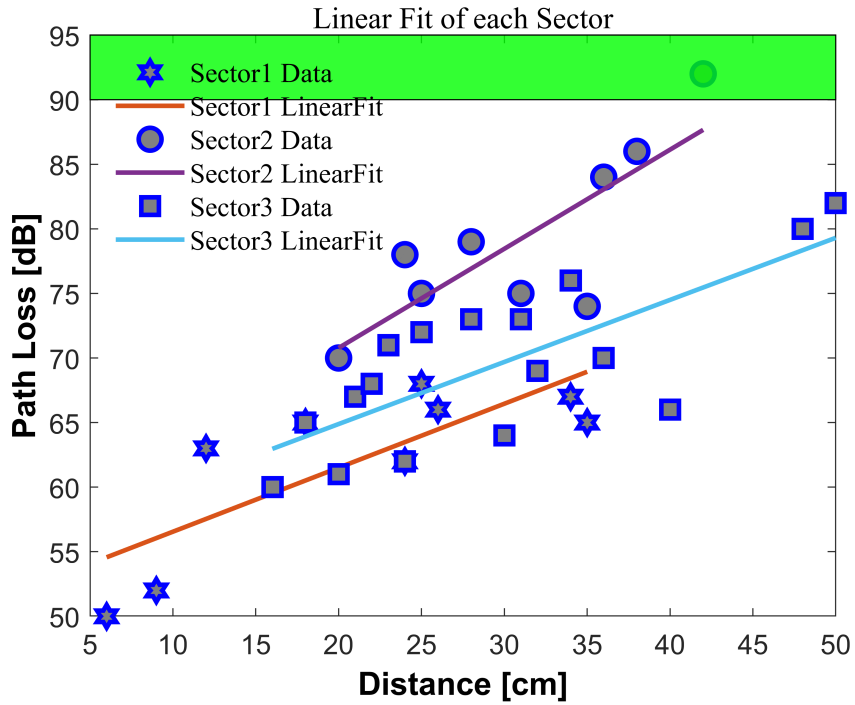


FIGURE 5.7: Linear regression on measured path loss data (case 1) at a 24 GHz on each sector

which was calculated using equation (5.1), for all three (sectors) sets of measured data. The standard deviation of the fitted curve for the measurements conducted on a human subject in sector 1 is 2.975, whereas, for non-line-of-sight measurements, it is 4.025. The rise in the pathloss exponent and shadowing factor indicates that the propagation channel is significantly influenced by the chest's curvilinear shape. Table 5.3 displays the estimated path loss exponents and deviation values. Equations 5.2, 5.3, and 5.4 represent the sector-wise lognormal path loss model with reference distance and maximum range, where these equations are valid under the settings mentioned in section 5.2.1:

$$\text{Sector1 : } P_L(d) = 50 + 10 \times 2.42 \times \log\left(\frac{d}{6}\right) + 2.975 \quad (5.2)$$

for $6\text{cm} \leq d \leq 100\text{cm}$

$$\text{Sector2 : } P_L(d) = 70 + 10 \times 5.12 \times \log\left(\frac{d}{20}\right) + 4.025 \quad (5.3)$$

for $20\text{cm} \leq d \leq 45\text{cm}$

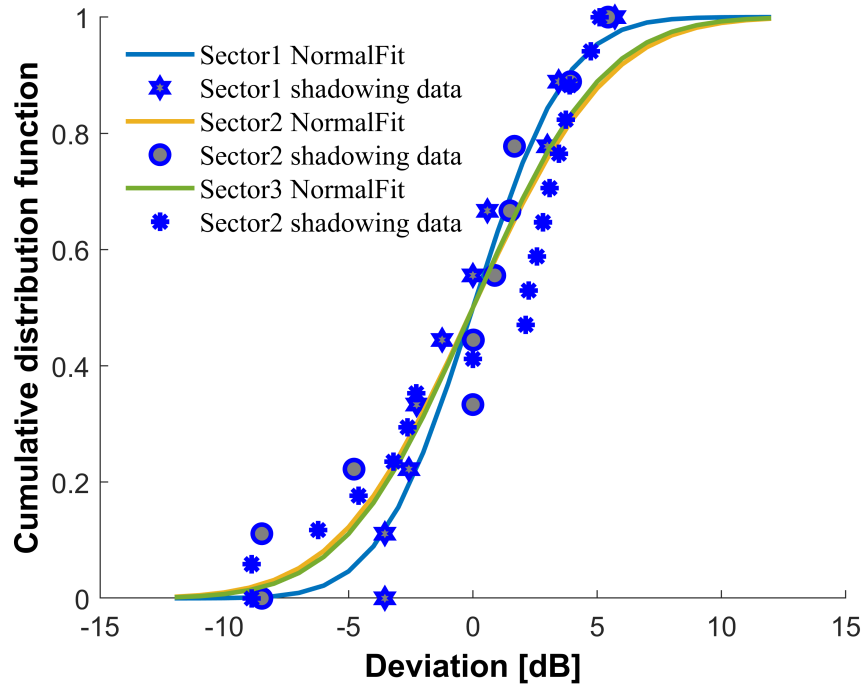


FIGURE 5.8: The cumulative distribution function of the shadowing factor for measured data (case 1)

$$\text{Sector3 : } P_L(d) = 60 + 10 \times 3.7458 \times \log\left(\frac{d}{16}\right) + 4.093 \quad (5.4)$$

for $16\text{cm} \leq d \leq 70\text{cm}$

TABLE 5.3: Path loss exponent and deviation values in case 1

Sector	d_0	$P_L(d_0)$ dB	Pathloss Exponent (n)	Deviation χ_σ
1(LoS)	6	50	2.42	2.975
2(NLoS)	20	70	5.12	4.025
3(PLoS)	16	60	3.7458	4.093

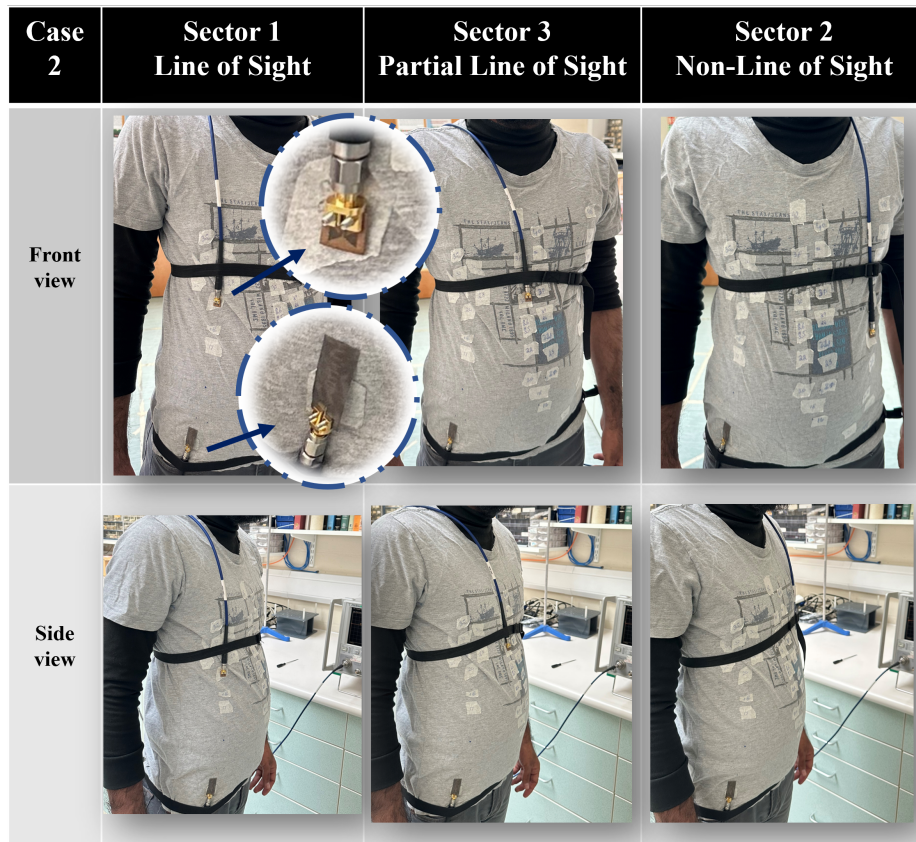


FIGURE 5.9: Measurement setup on a human subject in case 2 with front and side view

5.3.2 Case 2

In the 2nd case, the transmitter antenna is changed to more directional Yagi Uda antenna to examine the effects of end-fire along-the-body radiations. The gain is increased as a result of the forward, directional pattern. In sectors 1, 2, and 3, the measurements were performed under the reference distance (d_0) of 17 cm, 20 cm, and 16 cm, respectively. The minimum distance of sector 1 (LOS) is increased due to the larger size of the transmitter's Yagi antenna array.

In Fig.5.9, we can observe the measurement setup designed for the waist-to-torso link on a human subject in case 2, which includes both a front view and a side view. The primary objective of this particular setup is to accurately capture the curvature of the body and visually depict the line-of-sight angle between the transmit and receive antennas.

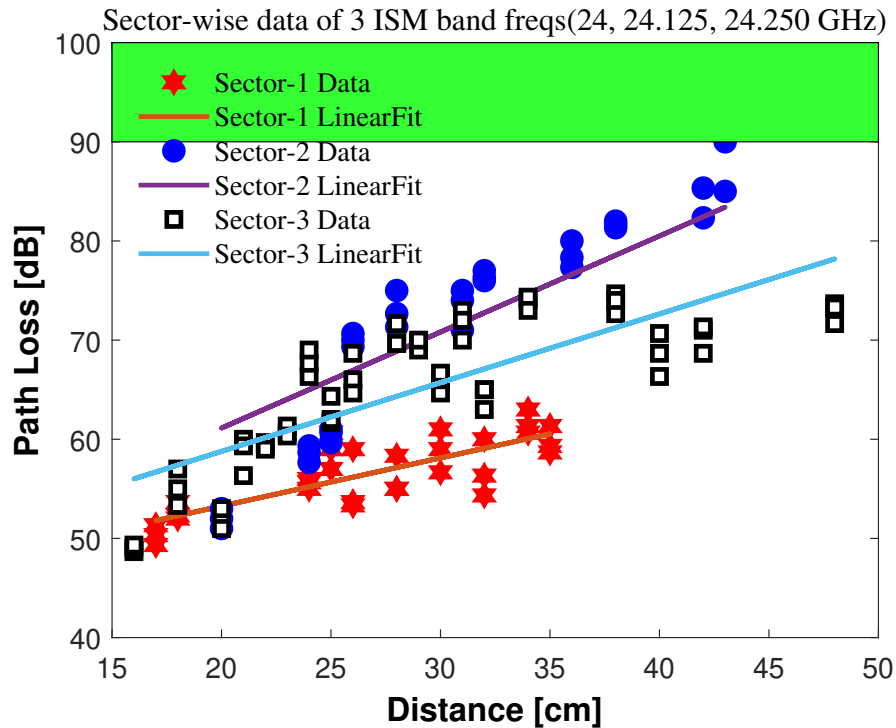


FIGURE 5.10: Linear regression on measured path loss data (case 2) at 3 frequencies sector-wise data covering complete band

Fig.5.10 shows the measured path loss for the waist-torso link for the three frequencies at distances defined by the receiver locations in each sector. As for Case 1, linear regression was used to determine the path loss exponents for each sector for the frequency of 24 GHz, as shown in Fig.5.11. The path loss exponent is 3.2 for sector 1 (line of sight), and 5.6 for sector 3. Nevertheless, for sector 2 (which is non-line of sight), the coefficient value is 7.9. This increase in the coefficient value (in each sector) can be attributed to a directional higher gain antenna that leads to an increase in the acceptable link range. Consequently, receiving points located far from the transmitter, such as those close to the shoulder, are not regarded as being in line-of-sight positions. This same trend is observed in the other two sectors as well.

Fig.5.12 shows the cumulative distribution function (CDF) of the shadowing factor $\chi(0,\sigma)$ calculated using equation (5.1) for three different sets of measured data. The standard deviation of the fitted curve for the measurements conducted on a human subject in sector 1 is 2.169, whereas, in sectors 2 and 3 (for non and partial line-of-sight measurements), it is 3.388 and 4.343, respectively. Table (5.4) lists

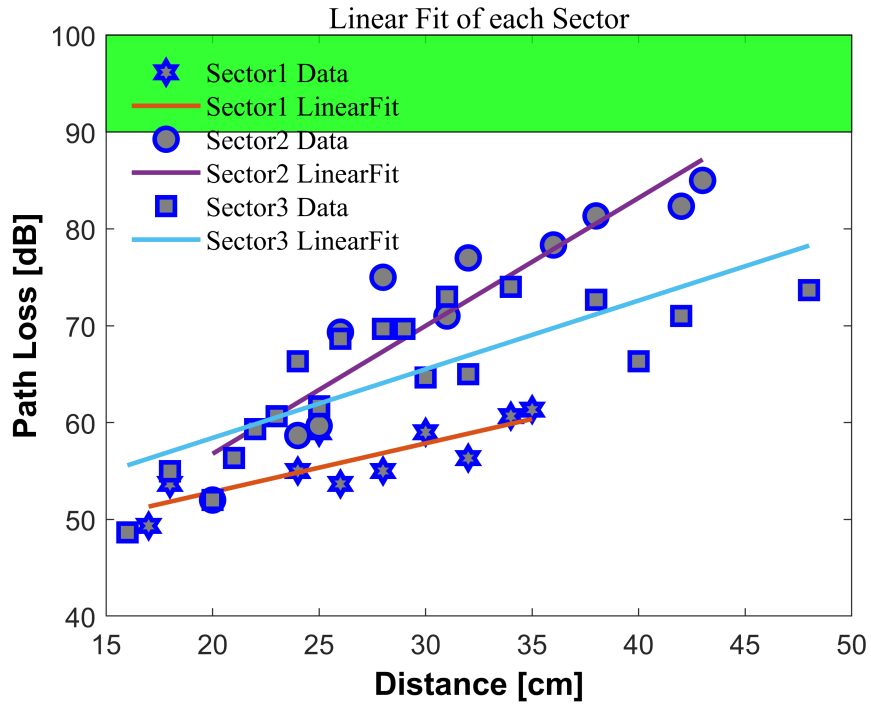


FIGURE 5.11: Linear regression on measured path loss data (case 2) at a 24 GHz on each sector

the estimated values of path loss exponent n and deviation χ_σ . The results show the acceptable link range increases in this case, especially in PLOS and NLOS sectors under mentioned transmit-receive settings. For all 3 sectors, the mean path loss with reference to distance can be expressed as a log-normal path loss model as shown in equations (5.5 - 5.7).

$$\begin{aligned} \text{Sector1 : } P_L(d) &= 49 + 10 \times 3.2 \times \log\left(\frac{d}{17}\right) + 2.169 \\ &\text{for } 17\text{cm} \leq d \leq 150\text{cm} \end{aligned} \quad (5.5)$$

$$\begin{aligned} \text{Sector2 : } P_L(d) &= 52 + 10 \times 7.9 \times \log\left(\frac{d}{20}\right) + 3.388 \\ &\text{for } 20\text{cm} \leq d \leq 60\text{cm} \end{aligned} \quad (5.6)$$

$$\begin{aligned} \text{Sector3 : } P_L(d) &= 48 + 10 \times 5.601 \times \log\left(\frac{d}{16}\right) + 4.343 \\ &\text{for } 16\text{cm} \leq d \leq 80\text{cm} \end{aligned} \quad (5.7)$$

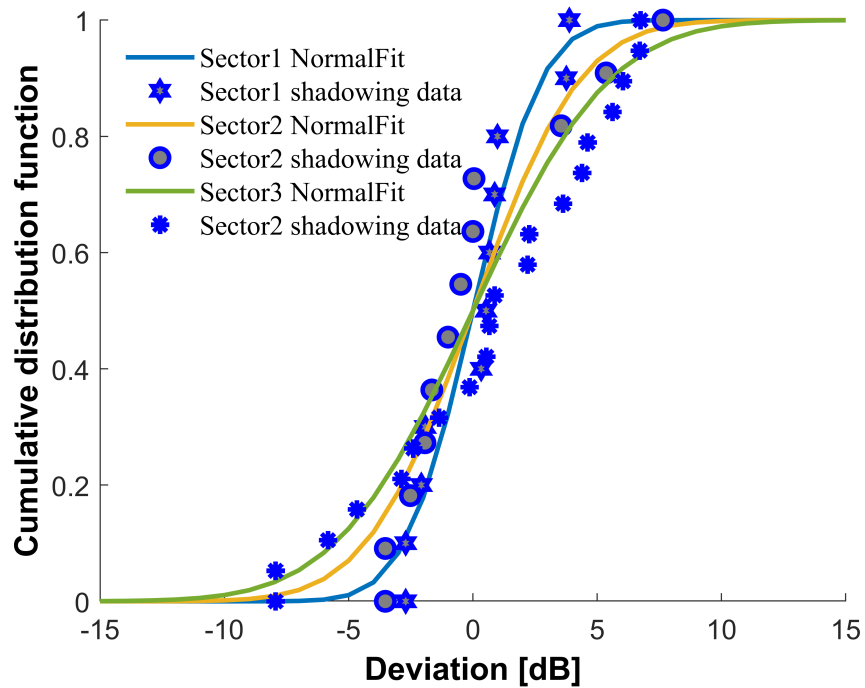


FIGURE 5.12: The cumulative distribution function of the shadowing factor for measured data (case 2)

TABLE 5.4: Path loss exponent and deviation values in case 2

Sector	d_0	$P_L(d_0)$ dB	Pathloss Exponent (n)	Deviation χ_σ
1(LoS)	17	-49	3.2	2.169
2(NLoS)	20	-52	7.9	3.388
3(PLoS)	16	-48	5.601	4.343

5.3.3 Case 3

In the 3rd case, the significant change in the experiment compared to case 2, is the replacement of the Yagi Uda antenna with a medium-gain (wider-beamwidth) Vivaldi antenna in the transmitter. A wider beam antenna may be desirable for several reasons, such as avoiding the need for accurate pointing, enabling a

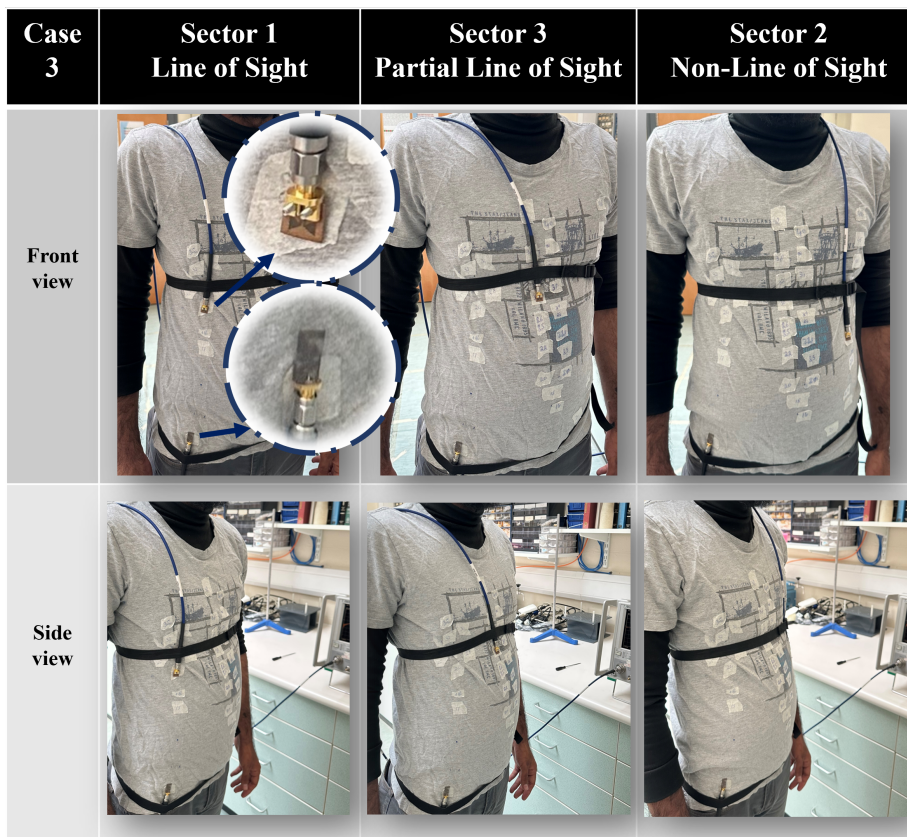


FIGURE 5.13: Measurement setup on a human subject in case 3 with front and side view

transmitter to transmit to multiple locations, or allowing a receiver to receive from multiple locations.

Measurements were performed in a similar manner to the previous cases, using three different reference distances (d_0) of 12 cm, 20 cm, and 16 cm in sectors 1, 2, and 3 respectively. The decrease in the minimum distance of sector 1 (LOS) from case 2 is because the transmitter's Vivaldi antenna is smaller in size than the Yagi Uda antenna. Similar to the previous case, Fig.5.13 is to illustrate the measurement setup for the waist-to-torso link on a human subject in case 3. The setup provides both front and side views and is designed to capture the body curvature. Additionally, it visually demonstrates the line-of-sight angle between the transmit and receive antennas. As before, the measurements were taken at the frequencies of 24, 24.125, and 24.25 GHz to observe the variation of path loss with each distance (shown in Fig.5.12).

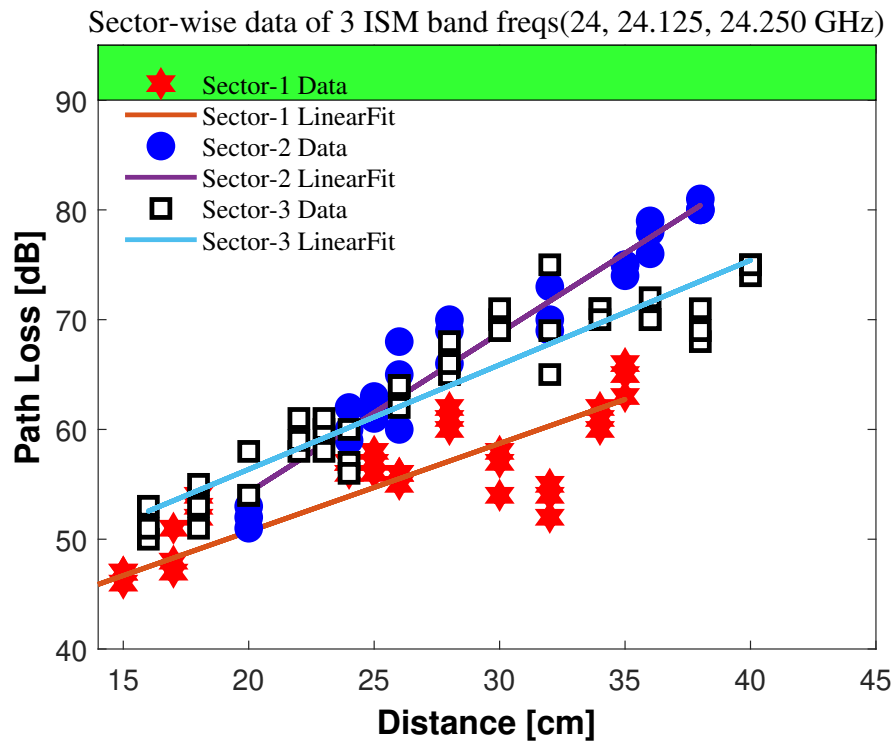


FIGURE 5.14: Linear regression on measured path loss data (case 3) at 3 frequencies sector-wise data covering complete band

Fig.5.14 shows the path loss at these three frequencies (24, 24.125, 24.25 GHz) for each sector, together with fits using linear regression analysis. The path loss exponent was determined by analysing the measured path loss data (shown in Fig.5.15) using linear regression. Compared to Case 2, the path loss exponent was found to be lower for each sector. The reduction in the coefficient value can be attributed to the use of a medium gain antenna with a wider beam, which results in better reception within the acceptable link range. The three different sets of measured data are represented in Fig.5.16, which displays the cumulative distribution function (CDF) of the shadowing factor $\chi(0,\sigma)$ calculated using equation (5.1). The standard deviation of the fitted curve for measurements conducted on a human subject in sector 1 is 2.931, while it is 2.436 and 1.862 for partial and non-line-of-sight measurements, respectively. Table 5.5 provides the estimated values of the path loss exponent n and deviation χ_σ .

The results of the experiments show that the acceptable link range improved in terms of Angular distance in the case of the medium-Gain Vivaldi antenna compared to the Yagi Uda antenna. This improvement was particularly noticeable in

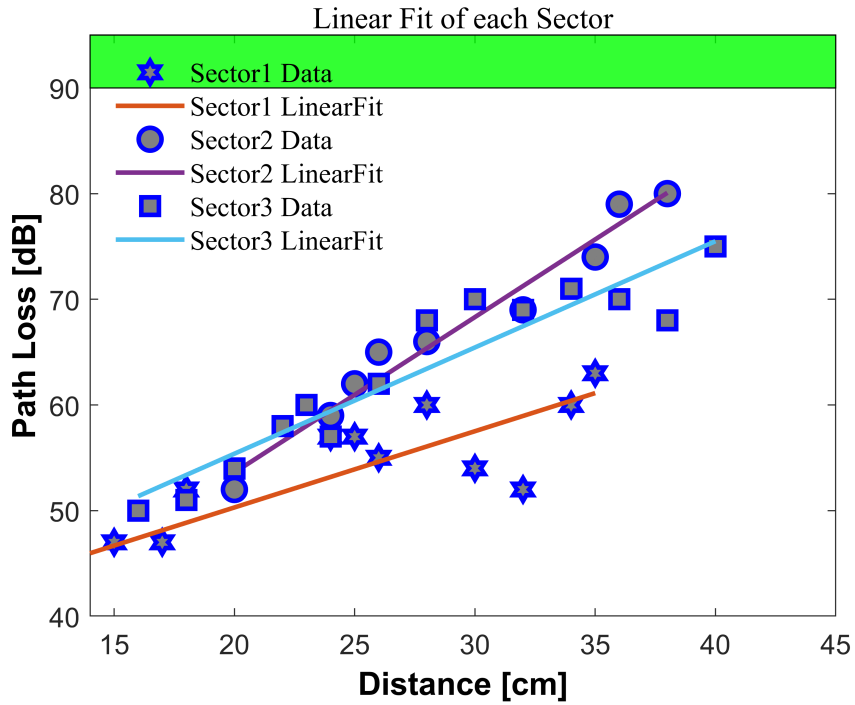


FIGURE 5.15: Linear regression on measured path loss data (case 3) at a 24 GHz on each sector

the PLOS and NLOS sectors with the mentioned transmit-receive settings.

$$\text{Sector1 : } P_L(d) = 40 + 10 \times 3.09 \times \log\left(\frac{d}{12}\right) + 2.931 \quad (5.8)$$

for $12\text{cm} \leq d \leq 100\text{cm}$

$$\text{Sector2 : } P_L(d) = 52 + 10 \times 7.57 \times \log\left(\frac{d}{20}\right) + 1.862 \quad (5.9)$$

for $20\text{cm} \leq d \leq 55\text{cm}$

$$\text{Sector3 : } P_L(d) = 50 + 10 \times 5.01 \times \log\left(\frac{d}{16}\right) + 2.436 \quad (5.10)$$

for $16\text{cm} \leq d \leq 75\text{cm}$

A lognormal model (5.8 - 5.10) was utilised to express the mean path loss as a function of distance across all three sectors. Section 5.1.2 provides the necessary conditions and settings for effectively utilising this model in predicting path loss.

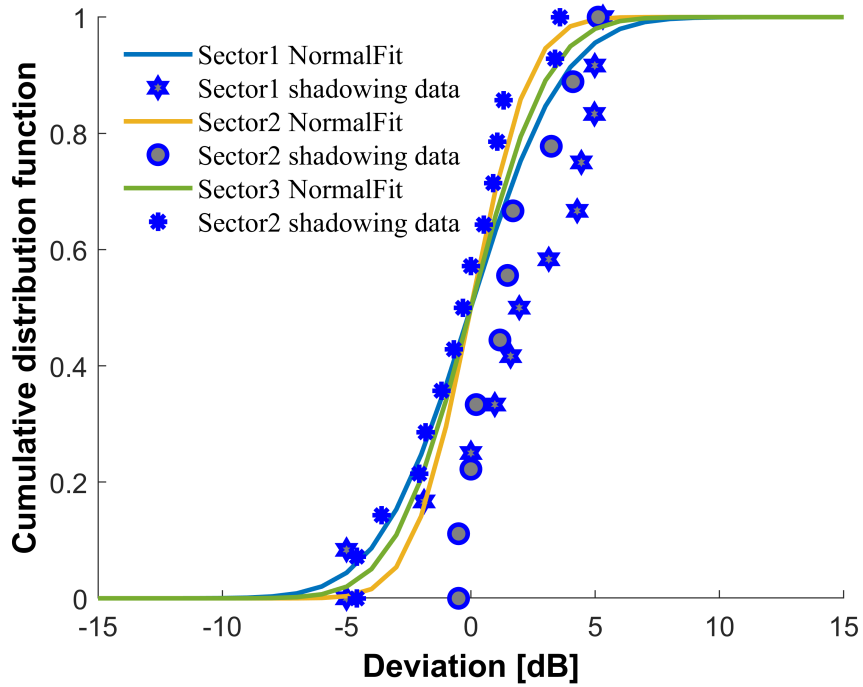


FIGURE 5.16: The cumulative distribution function of the shadowing factor for measured data (case 3)

TABLE 5.5: Path loss exponent and deviation values in case 3

Sector	d_0	$P_L(d_0)$ dB	Pathloss Expo- nent (n)	Deviation χ_σ
1(LoS)	12	-40	3.09	2.931
2(NLoS)	20	-52	7.57	1.862
3(PLoS)	16	-50	6.01	2.436

5.3.4 Case 4

In the final case, the receiver antenna was replaced by an EBG-backed bow-tie slot antenna, while the transmit antenna was kept as the Vivaldi antenna, as used in case 3. This change was made because the EBG-backed bow tie slot antenna was deemed to be the best suited in terms of its performance on the body, gain, and radiation pattern around the human body. As described in Section 5.2, the

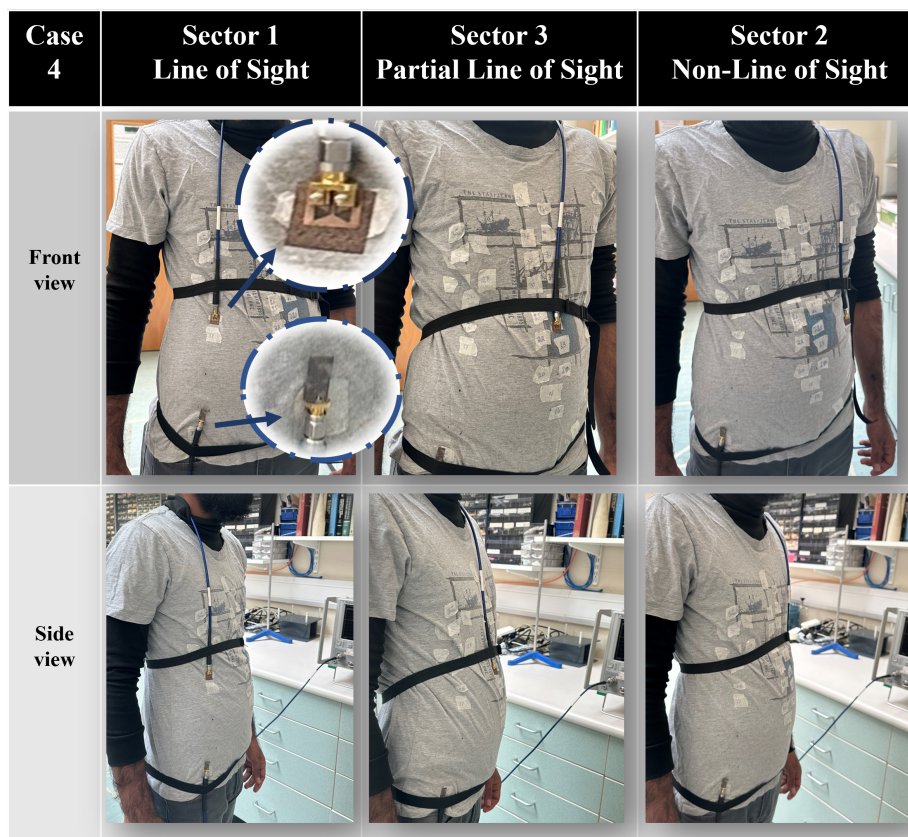


FIGURE 5.17: Measurement setup on a human subject in case 4 with front and side view

EBG-backed antenna has a reasonable gain, and a suppressed back lobe, and is insensitive to body loading.

The stable and improved performance of the receiving antenna at every location on the body enhances signal reception, resulting in an increased link range. Therefore, based on the information provided in Fig.5.1b, the measurement settings were modified and the number of receiving points was increased in all sectors, as compared to previous cases to get a comprehensive model to predict path loss in similar scenarios with similar equipment. The minimum distances (d_0) from the transmitter were set to 14 cm, 24 cm, and 14 cm in sectors 1, 2, and 3 respectively. The reason for the change in the minimum distance for all sectors from the previous cases is due to the larger size of the receiver antenna, which is an EBG-backed bow-tie antenna. Similar to all the previous 3 cases, The measurement setup for

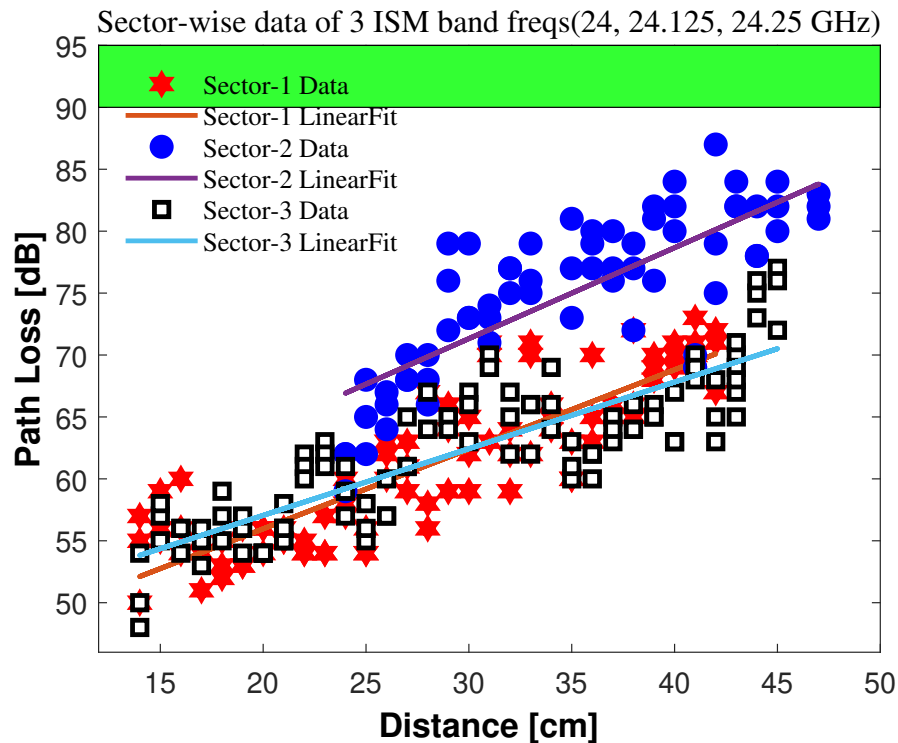


FIGURE 5.18: Linear regression on measured path loss data (case 4) at 3 frequencies sector-wise data covering complete band

the waist-to-torso link on a human subject in case 4 is depicted in Fig.5.17, offering both front and side views. This setup aims to accurately capture the body curvature and visually demonstrate the line-of-sight angle between the transmit and receive antennas.

Fig.5.18 presents path loss data for the 24 GHz ISM band frequencies, collected to understand how path loss behavior varies across the band, similar to previous cases. Using the data presented in Fig.5.19, values of the path loss exponent n were derived by employing linear regression analysis. The path loss exponent was lower for sector 3 compared to previous cases. Despite this reduction in the coefficient value, the acceptable link range was higher than in the previous cases. As in the previous cases, the mean path loss with reference to distance was expressed as a curve fitting for all three sectors. These models can be used to predict path loss in similar scenarios with similar equipment and conditions. Equations (5.11 - 5.13) describe a log-normal path loss model that can be applied to express the average path loss as a function of distance for all three sectors.

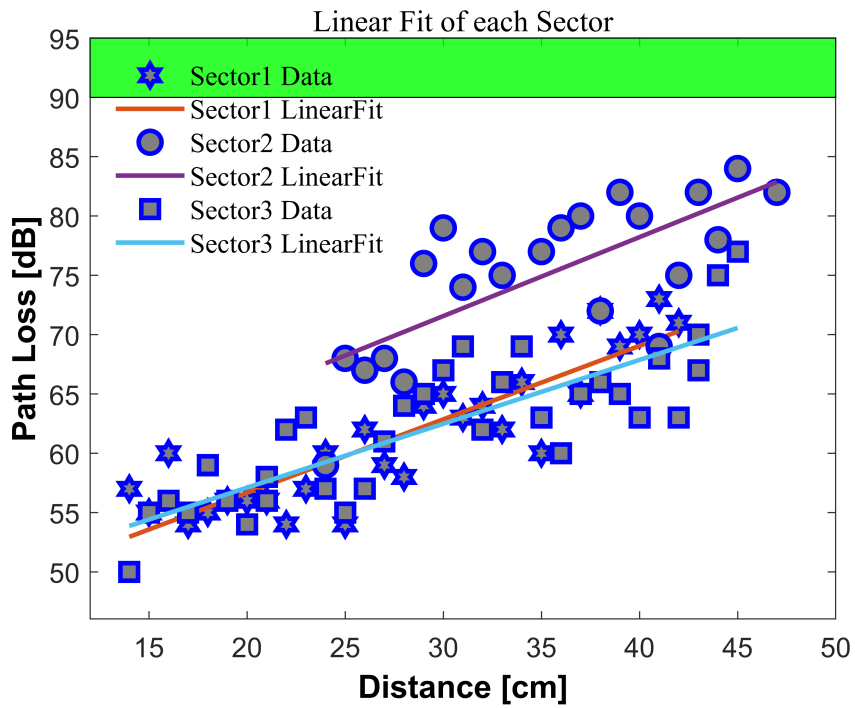


FIGURE 5.19: Linear regression on measured path loss data (case 4) at a 24 GHz on each sector

$$\text{Sector1 : } P_L(d) = 55 + 10 \times 2.62 \times \log\left(\frac{d}{14}\right) + 3.578 \quad (5.11)$$

for $12\text{cm} \leq d \leq 120\text{cm}$

$$\text{Sector2 : } P_L(d) = 62 + 10 \times 7.01 \times \log\left(\frac{d}{24}\right) + 3.424 \quad (5.12)$$

for $20\text{cm} \leq d \leq 60\text{cm}$

$$\text{Sector3 : } P_L(d) = 54 + 10 \times 2.91 \times \log\left(\frac{d}{14}\right) + 3.196 \quad (5.13)$$

for $16\text{cm} \leq d \leq 100\text{cm}$

In Fig.5.20, the cumulative distribution function (CDF) of the shadowing factor $\chi(0,\sigma)$ is shown for three different sets of measured data. The shadowing factor was calculated using equation (5.1). This model can be effectively applied to

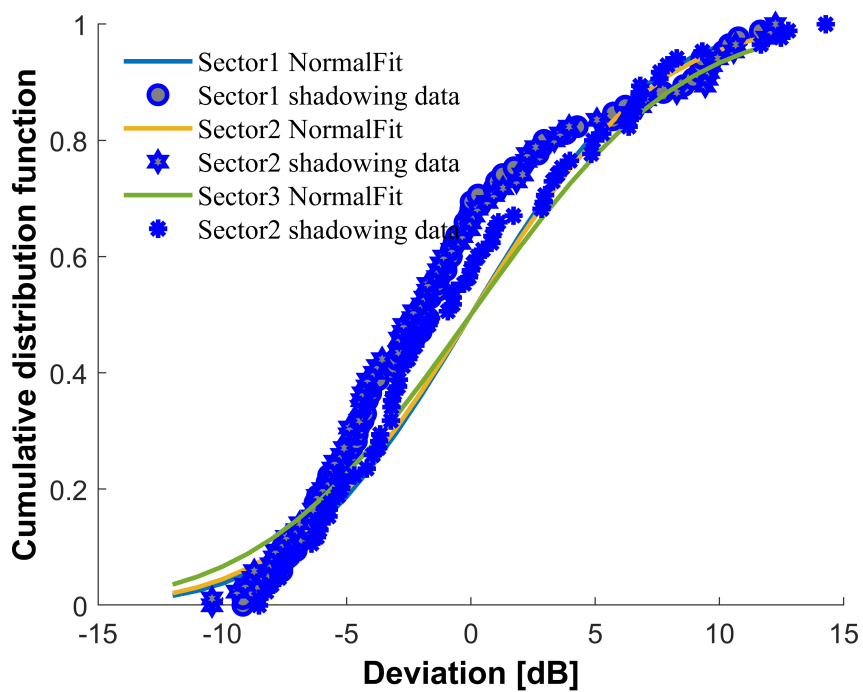


FIGURE 5.20: The cumulative distribution function of the shadowing factor for measured data (case 4)

predict path loss under the same conditions and settings, as described in section 5.1.2.

TABLE 5.6: Path loss exponent and deviation values in case 4

Sector	d_0	$P_L(d_0)$ dB	Pathloss Exponent (n)	Deviation χ_σ
1(LoS)	14	-55	2.62	3.578
2(NLoS)	24	-62	7.01	3.424
3(PLoS)	14	-54	2.91	3.196

5.4 Conclusion

This chapter has focused on investigating body-centric wireless communication at the 24 GHz ISM band. In this study, the propagation parameters (path loss exponent and shadowing factor) of on-body communication systems are determined, and the impact of different antenna types on the performance of these systems is investigated. Four antenna types, including Bow-tie, EBG-backed Bow-tie, Yagi Uda, and Vivaldi antennas, were selected for this investigation to demonstrate the significant antenna characteristics (radiation propagation) that should be incorporated for on-body channels.

It was also noted that the variation in the radiation pattern of both transmitting and receiving antennas can introduce additional uncertainty to the measurements. The results of the study demonstrate that the received power depends not only on the frequency of the on-body channel and distances but also on the antenna locations. Measurements were conducted with a human subject to achieve this objective, and the path loss exponent model was compared across all four cases and in all three sectors of the waist-to-torso link. In this study, the shadowing factor was modeled by a normal distribution after performing linear regression analysis on the data in terms of the path loss exponent and shadowing factor.

The findings from the experimental setup detailed in Section 5.2.1 reveal that a comparison of the path-loss exponent values in sector 2 (NLOS) consistently demonstrates a poor link range accompanied by a significantly high path-loss exponent. As a result, the optimal arrangement of placing the sink node on both sides of the waist can effectively mitigate the NLOS segment in the waist-to-torso link. This knowledge holds broader implications and can be applied more widely in similar scenarios where reducing the impact of NLOS propagation is crucial for achieving improved communication performance.

The observation that a high path loss exponent is consistently observed in sector 2 across all cases implies that this sector experiences a greater signal attenuation than sectors 1 and 3, possibly due to obstacles or interference in the communication

channel. However, in case 4, where both the transmit and receive antennas exhibit superior gain and good on-body performance, sectors 1 and 3 display similar path loss exponent values. This finding suggests that the signal strength decays at a slower rate in sectors 1 and 3, indicating that the directional beam antennas offer better signal propagation in these sectors. The findings of Case 4 underscore the significance of carefully selecting appropriate on-body transmit-receive antenna types for on-body communication systems. The observed improvement in system performance highlights how the right equipment can have a significant impact on the system's overall performance.

The results of this study highlight the importance of investigating the impact of the human body's contoured shape on path loss at 24 GHz. By recognizing the significant influence of body morphology on signal propagation, this information becomes crucial for developing precise path loss models, enabling accurate link budget evaluations for on-body communication systems. These findings contribute to the advancement and optimisation of wireless communication systems by providing insights into the contoured shape's effect on path loss.

References

- [1] P. S. Hall and Y. Hao, "Antennas and Propagation for Body-Centric Wireless Communications." *Boston, MA, USA: Artech House*, 2006.
- [2] D. Tze Huei Lai, M. Palaniswami, and R. Begg, "Healthcare Sensor Networks: Challenges Toward Practical Implementation." New York, NY, USA: CRC, 2011.
- [3] Z. N. Chen, "Antennas for Portable Device." Hoboken, NJ, USA: Wiley-Blackwell, 2007.
- [4] S. Collonge, G. Zaharia, and G. El Zein, "Influence of the human activity on wide-band characteristics of the 60 GHz indoor radio channel," *IEEE Trans. Wireless Commun.*, vol. 3, no. 6, pp. 2396–2406, Nov. 2004.
- [5] S. Obayashi and J. Zander, "A body-shadowing model for indoor radio communication environments," *IEEE Trans. Antennas Propag.*, vol. 46, no. 6, pp. 920–927, Jun. 1998.
- [6] S. Ali and M. J. Mughal, "Narrowband characterization of the 60 GHz indoor radio channel in the presence of human bodies," presented at the *Int. Conf. Emerging Technologies (ICET)*, Islamabad, Pakistan, 2010.
- [7] P. J. Soh, G. A. E. Vandenbosch, S. L. Ooi, and N. H. M. Rais, "Design of a broadband all-textile slotted PIFA," *IEEE Trans. Antennas Propag.*, vol. 60, no. 1, pp. 379–384, Jan. 2012.
- [8] G. Adamiuk, T. Zwick, and W. Wiesbeck, "UWB antennas for communication systems," *Proc. IEEE, to be published*.

-
- [9] W. Zheyu, Z. Lanlin, D. Psychoudakis, and J. L. Volakis, "Flexible textile antennas for body-worn communication," presented at the *IEEE Int. Workshop Antenna Technology*, Tucson, AZ, USA, 2012.
- [10] Pellegrini A, Brizzi A, Zhang L, et al." Numerical and experimental analysis of the on-body propagation channel at W band C", *European Conference on Antennas and Propagation. IEEE*,2012.
- [11] Abbasi Q H, Sani A, Alomainy A, et al. "Numerical Characterization and Modeling of Subject-Specific Ultrawideband Body-Centric Radio Channels and Systems for Healthcare Applications[J]". *IEEE Transactions on Information Technology in Biomedicine*, 16(2):221-227, 2012.
- [12] Y. Zhao, A. Sani, Y. Hao, S.-L. Lee, and G.-Z. Yang, "A subject-specific radio propagation study in wireless body area networks," in *Proc. LAPC, Loughborough, U.K.*, 2009, pp. 80–83.
- [13] X. Y. Wu et al., "Preliminary estimate for observability of 60 Ghz wireless body area networks," presented at the 2012 *Asian-Pacific Conf. Antennas and Propagation*, Singapore.
- [14] Attenuation by Atmospheric Gases, ITU-R, 2005, P.676-6.
- [15] Radiocommunication Sector of International Telecommunication Union. Recommendation ITU-R P.676-10: Attenuation by atmospheric gases 2013.
- [16] P. S. Hall, Y. Hao, and S. L. Cotton, "Progress in antennas and propagation for body area networks," presented at the *Int. Symp. Signal Systems and Electronics*, Nanjing, China, 2010.
- [17] A. Alomainy, Y. Hao, A. Owadally, C. G. Parini, Y. Nechayev, C. C. Constantinou, and P. S. Hall, "Statistical analysis and performance evaluation for on-body radio propagation with microstrip patch antennas," *IEEE Trans. Antennas Propag.*, vol. 55, no. 1, pp. 245–248, Jan. 2007.
- [18] Q. H. Abbasi, A. Sani, A. Alomainy, and Y. Hao, "Numerical characterization and modelling of subject-specific ultrawideband body-centric radio channels

-
- and systems for healthcare applications,” *IEEE Trans. Inf. Technol. Biomed.*, vol. 16, no. 2, pp. 221–227, Mar. 2012.
- [19] A. Sani, A. Alomainy, and Y. Hao, “Numerical characterization and link budget evaluation of wireless implants considering different digital human phantoms,” *IEEE Trans. Microw. Theory Tech.*, vol. 57, no. 10, pp. 2605–2613, Oct. 2009.
- [20] M. Gallo, P. S. Hall, Q. Bai, Y. I. Nechayev, C. C. Constantinou, and M. Bozzetti, “Simulation and measurement of dynamic on-body communication channels,” *IEEE Trans. Antennas Propag.*, vol. 59, no. 2, pp. 623–630, Feb. 2011.
- [21] S. Dumanli and C. J. Railton, “Analysis of coupled tilted slot antennas in FDTD using a novel time domain Huygens method with application to body area networks,” *IEEE Trans. Antennas Propag.*, vol. 60, no. 4, pp. 1987–1994, Apr. 2012.
- [22] K. Ali, A. Brizzi, S. Lee, Y. Hao, A. Alomainy, and G.-Z. Yang, “Numerical analysis of on-body channel for statistically-generated body shapes,” presented at the *Loughborough Antennas and Propagation Conf.*, Loughborough, U.K, 2011.
- [23] P. P. Viezbicke, “Yagi antenna design,” NBS Technical Note 688, National Bureau of Standards, Boulder, Colorado, 1976.
- [24] G. Thiele, E. Ekelman and L. Henderson, “On the accuracy of the transmission line model of the folded dipole,” *IEEE Trans. Antennas and Propagation*, vol. 28, no. 5, pp. 700-703, Sep. 1980.
- [25] M. Ali, J. C. Batchelor, I. Ullah and N. J. Gomes, ”Ultra-thin EBG backed flexible antenna for 24 GHz ISM band WBAN,” 2022 *Antenna Measurement Techniques Association Symposium (AMTA)*, Denver, CO, USA, 2022, pp. 1-4, doi: 10.23919/AMTA55213.2022.9954953.

- [26] Ali, M., et al.: Ultra-thin electromagnetic bandgap backed fractal geometry-based antenna for 24 GHz ISM band WBAN. *IET Microw. Antennas Propag.* 1– 7, 2022. <https://doi.org/10.1049/mia2.12321>.
- [27] A. Sani, Y. Zhao, Y. Hao, S.-L. Lee, and G.-Z. Yang, “Subject-specific analysis of the on-body radiation channel adopting a parallel FDTD code,” presented at the *Eur. Conf. Antennas and Propagation*, 2010.
- [28] E. Reusens, W. Joseph, B. Latre, B. Braem, G. Vermeeren, E. Tanghe, L. Martens, I. Moerman, and C. Blondia, “Characterization of on-body communication channel and energy efficient topology design for wireless body area networks,” *IEEE Trans. Inf. Technol. Biomed.*, vol. 13, no. 6, pp. 933–945, 2009.

Chapter 6

A Case Study of CSMA (ZigBee) for WBANs at 24 GHz

6.1 Introduction

Wireless Body Area Network (WBAN) is a rapidly advancing technology that plays a crucial and sensitive role in eHealth and telemedicine. Ensuring a high data rate and uninterrupted communication link is of utmost importance. The WBAN's physical (PHY) layer must meet certain prerequisites, such as avoiding any adverse effects on human health, having wearable devices of small size, and providing suitable coverage for a limited area. On the other hand, the Media Access Control (MAC) layer of WBAN needs to prioritise services and ensure fairness in resource sharing. Traditionally, WBAN PHY-MAC has been based on 2.4 GHz microwave frequency. However, there is growing interest in utilising 24 and 60 GHz millimeter-wave (mmWave) frequencies as a potential solution to the aforementioned challenges [1].

Wireless communication at mm-wave frequencies is considered the best option to achieve high data rates in upcoming future wireless networks. However, these very high-frequency waves undergo significant attenuation, deafness, and blockage, and may require microwave or sub-6 GHz networks for synchronisation and fallback

support. mm-Wave communication systems have special hardware constraints that introduce new challenges for efficient MAC and physical layer design. The hardware architecture of an antenna array-based mm-wave transceiver is complicated and contains many RF analog components [2]. More importantly, these analog components are generally imperfect due to manufacturing errors and introduce different hardware imperfections such as phase noise, power amplifier nonlinearities, IQ imbalance, and so on, especially in mm-Wave frequencies [3].

Conventional MAC layer protocol design fundamentals may need a thorough reconsideration as mm-Wave systems have severe channel attenuation, stringent hardware constraints, directional communication, vulnerability to obstacles, reduced interference footprint, and potentially high signaling overhead [4]. In the literature, up to now, PHY and propagation issues received far more attention as compared to the medium access control (MAC) layer. However, Differences between existing communication technologies and mm-Wave networks challenge conventional design approaches [5]. Several researchers proposed many energy-efficient MAC protocols for WBANs [6] - [9]. The MAC protocol presented in [7] incorporates important techniques (such as low-power listening, scheduled channel polling, and periodically turning on/off radio) for generic wireless sensor networks to attain significant throughput comparable to the load at low load.

In the literature, many researchers presented examples of contention-based and contention-free (explained in Chapter 2) MAC protocols [10]. FDMA-based MAC is not suitable for wireless sensor networks, although it provides collision-free communication. That's because of challenging front-end hardware design, especially filters [11]. Therefore, in the current scenario, FDMA-based MAC is only suitable when the channel is not shared with two or multiple nodes. This will be further explained in a later section. CSMA/CA-based MAC has a simple structure, better reliability, low latency at medium traffic, and quite high energy consumption. On the other hand, TDMA-based MAC is not scalable and requires node synchronization. Therefore the auxiliary radio channel, an extra channel in wireless systems used for purposes other than primary data transmission is used to wake

the scheduled node for transmission. This alternate method involves out-of-band communication channels to minimize idle listening and power consumption [11].

Many limitations and constraints should be taken into account while choosing suitable technologies for mm-wave on-body communication in WBANs. Low power consumption is one of the main requirements in WBANs as it maximizes the lifespan of deployed sensor nodes and the network. Typically for on-body communication, unnecessary high power may cause additional interference in communication [12]. Zigbee technology is considered the most suitable option for addressing the challenges mentioned above, which is why it is widely adopted in Wireless Body Area Networks (WBANs) [13]. This technology utilises the CSMA/CA medium access protocol.

The primary focus of this chapter is to conduct a performance analysis of the Zigbee (PHY and MAC) protocol while using the 24 GHz ISM band on-body propagation path-loss model. The analysis takes into account the channel information provided in Chapter 5 and all the simulations are performed in the NetSim network simulator. The first stage involves analysing the physical layer performance by examining the Received Signal Strength Indicator (RSSI) and Bit Error Rate (BER) of the sink to individual sensors link. In the second stage, the performance of the MAC (CSMA/CA) protocol is evaluated in on-body channel environments at 24 GHz using various types of sink and sensor node antennas (as considered during channel characterisation in Chapter 5).

A significant challenge arises from the network simulator's inability to support separate path loss channel models for the sink and sensors, as well as between the sensors. To overcome this limitation, physical layer parameters (especially distances between sensors) have been adjusted to align the measured and simulated results, creating an environment in simulation that closely mimics the actual conditions. By thoroughly examining the performance characteristics of Zigbee (PHY and MAC) in this frequency band, we aim to gain valuable insights and contribute to the understanding and improvement of WBAN systems.

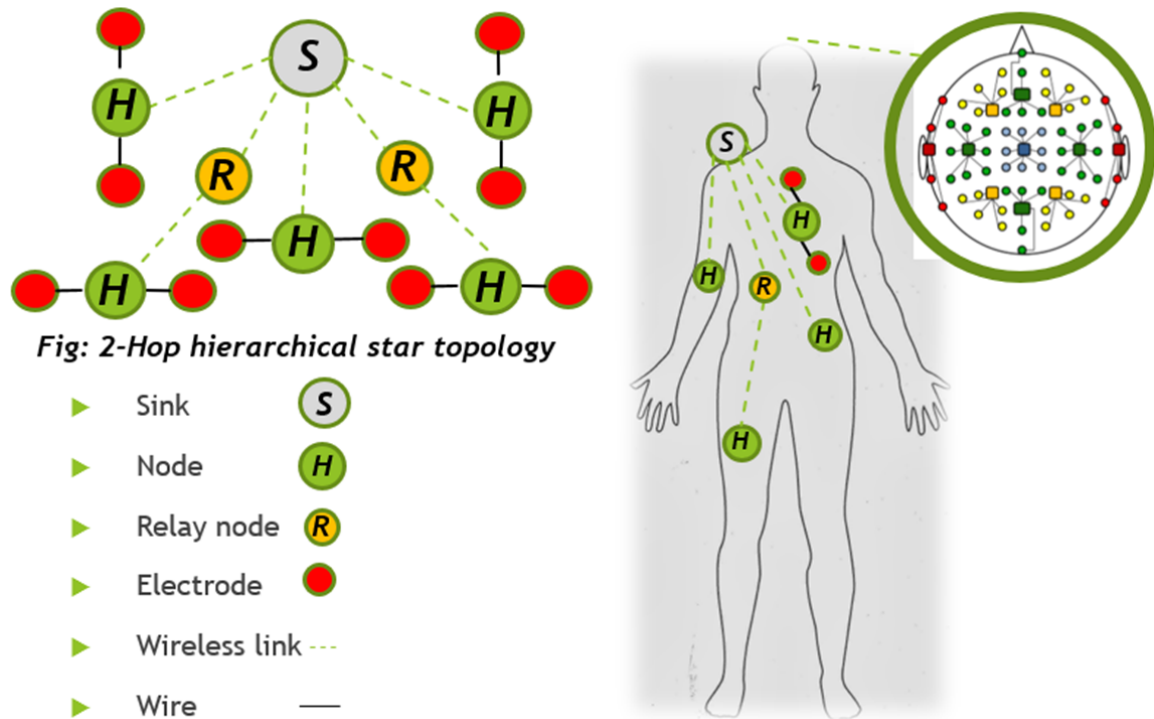


FIGURE 6.1: Typical Star topology-based WBAN network

6.2 Topology and architecture of mm-Waves WBAN

The attenuation of electromagnetic waves is considerably high in the body sensor network, due to the high path loss of the human body. Therefore, using of single-hop topology for WBAN is not suitable and multi-hop communication is recommended [14]. For multi-hop communication, relay nodes can be used to gather data from sensors and forward it toward the sinks [15], [16].

Relaying and cooperation mechanisms are introduced to affect the energy consumption in WBANs [18]. Relaying and multihop communications are key components of future mm-Wave networks for range extension and blockage alleviation [19], [20], [21]. In reference [22], it was shown that having an alternative path using relay node(s) can significantly alleviate the blockage. Current mm-Wave standards support only single- or two-hop links rather than the complete multi-hop communication capability envisioned in IEEE 802.11ay (explained in Chapter 2) [21]. Fig.6.1. shows the typical 2-hop hierarchical star topology for wireless

TABLE 6.1: STANDARD SENSORS USED IN A TYPICAL WIRELESS BODY AREA NETWORK [17]

Node	Place- ment	Parameter	O/P Form	O/P Range	Frequency Hz	Criti- cality	channels
1	Chest	ECG	Waveform Continuous	0.5-4mV	0.1-200	High	6
2-11	Head	EEG	Waveform Continuous	3uV-300uV	0.5-100	High	40
12	Chest, Arm	EMG	Waveform Continuous	10uV- 15mV	10-5000	Low	3
13	Abdomen	Respiratory rate	Discrete Time Bound	2-50 breath/min	0.01 to 10	Low	Shared 1
14	Chest	Body Tem- perature	Discrete Time Bound	32-40 C	0-0.1	Low	Shared 1
15	Arm, Chest	Blood Pres- sure	Discrete Time Bound	10-400mm Hg	0-50	Low	Shared 1
16- 17/22	Chest	Inertial measure- ment unit	Discrete Time Bound	Position	—	Low	Shared 1

E-health monitoring. Considering the significant path loss and restricted transmission power limits, a two-hop network is preferable over a single-hop network for covering non-line-of-sight node locations. Adding more hops entails additional alignment overhead per hop, which may limit the benefits of multi-hop communications [13].

In this chapter, our primary focus lies in the detailed examination and analysis of the system-level modeling for the Zigbee (PHY and MAC) protocol when applied to the mm-wave radio architecture for body-centric communications. We measure the system's performance by analysing the throughput in relation to the offered load. This study focuses on a wireless body area network utilising the 24 GHz path loss model and operating under high loads. The investigation includes analysing the proportion of the load that is effectively transmitted over the network, providing valuable insights into the successful transmission rate. For this purpose, we have utilised the typical star topology, as depicted in Fig.6.1, and selected the basic physiological sensors as presented in Table 6.1. Then assigns

them the appropriate number of channels available within the 24 GHz ISM band based on their respective requirements.

The Zigbee protocol operates within a bandwidth of 80 MHz at 2.4 GHz, accommodating a total of 16 channels. Each channel possesses a width of 2 MHz, with a 3 MHz gap separating one channel from the next. Conversely, considering the same channel separation gap and single channel bandwidth as Zigbee (IEEE 802.14.5) standards, the 24 GHz ISM band offers a broader bandwidth of 250 MHz, allowing for an increased number of channels, which now totals 50.

To allocate the appropriate number of channels to each type of physiological sensor, several factors were considered, including the sampling rate (frequency), criticality of information, and output type. For instance, ECG sensors provide critical information with a medium sampling rate, presenting continuous output waveforms. Consequently, ECG sensors have been assigned 6 channels. Table 6.1 illustrates the Wireless Body Area Network (WBAN) considered in this study, revealing that sensors like ECG, EEG, and EMG do not share channels. This separation is necessary as these sensors require the continuous transmission of critical information. In contrast, 3, 5, or 10 sensors (depending on the number of sensors used for the Inertial Measurement Unit) together utilise only one channel, as the information they generate is time-bound (not continuous) and of relatively low criticality. By carefully considering these factors, we ensure efficient channel allocation that aligns with the specific requirements of each sensor type.

The presented Zigbee MAC protocol can be described as a combination of FDMA with CSMA/CA due to the nature of sensor channel sharing. While some sensors operate on dedicated channels without sharing, others share their channels with other nodes. Sensors like ECG or EEG utilise FDMA to support multiple channels, allowing for simultaneous transmission. Conversely, sensors such as inertial measurement units and temperature sensors that share channels with other nodes employ CSMA/CA. Therefore, the analysis presented in this chapter primarily focuses on the FDMA with CSMA/CA characteristics of the Zigbee (PHY and MAC) protocol.

To ensure consistency with the measurement environment, one challenge is to have sensor nodes exhibit Line-of-Sight (LOS) behavior with each other while communicating with the sink node. Therefore, it is crucial for these nodes to be located within the same sector. For example consider the Non-Line-of-Sight (NLOS) sector, the simulation for the Sensors to Sink link runs under high path loss model parameters. However, it is still essential for the sensor nodes to be in close proximity to each other to effectively sense each other, even under the high path loss exponent, as they are supposed to lie in the same sector and exhibit LOS behavior with each other (based on chapter 5 measurements). Otherwise, improper positioning of the nodes may lead to increased hidden terminal issues, where two or more nodes are out of each other's range but within the range of a common receiver. This emphasizes the significant impact of sensor node positioning on the network's throughput performance.

The structure of the remaining part of this chapter is organized as follows. Subsequent sections provide a performance analysis of Zigbee, taking into account the channel information outlined in Chapter 5. First considering physiological sensor nodes that operate on channels without interference from other nodes. Therefore, Section 6.3 presents the performance analysis in terms of Bit Error Rate (BER) as a function of distance for individual sensors that do not share channels. Moving on to main Section 6.4, we examine the system-level performance of CSMA/CA at 24 GHz, specifically in terms of throughput in relation to the offered load. This evaluation specifically examines the performance of sensors that share the same channel, providing insights into how the protocol performs under different levels of network traffic. Finally, in Section 6.5, we draw conclusions based on the findings and observations from the previous sections.

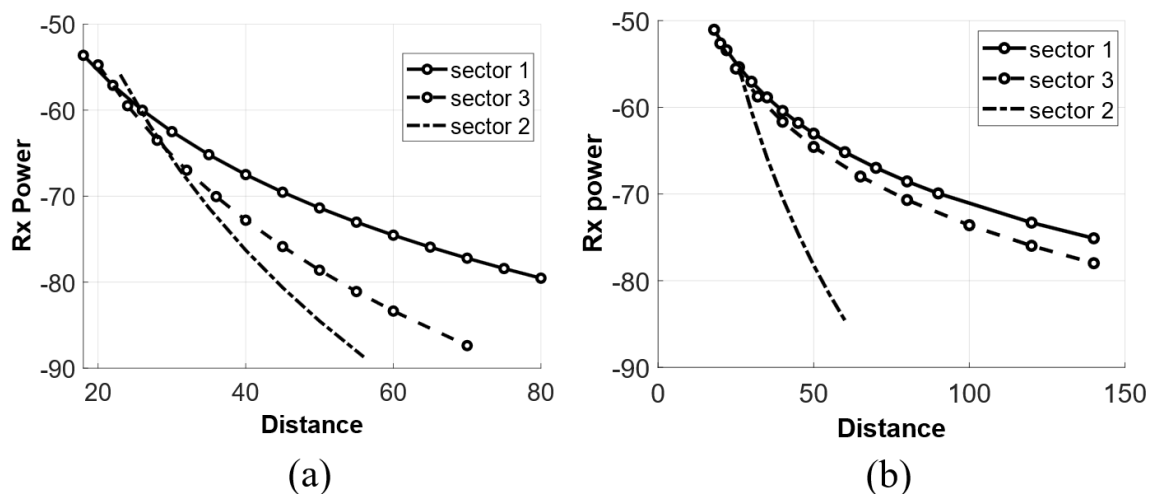


FIGURE 6.2: Simulated Received signal strength against distance (a) Case 2 (section 5.3.2) (b) Case 4 (section 5.3.4) using 24 GHz channel model

6.3 Simulation of Zigbee (Physical layer) at 24 GHz: Sink with one sensor node

In the context of the star topology with M nodes connected to a single sink, the first focus was on the scenario where there is only one node (sensor). This is done to establish the performance of the physical layer (PHY) for the 24 GHz channel, utilising the NetSim network simulator in its standard version. First, Physical layer performance is analysed by investigating RSSI (received signal strength indicator). Fig.6.2 displays the decrease in the received signal with distance across two different cases and three sectors (LOS, NLOS, PLOS) as previously described in the preceding chapter.

Figure 6.2 illustrates the simulated received signal strength plotted against the distance (cm) based on the estimated channel path loss parameters presented in sections 5.3.2 and 5.3.4. The results indicate that in case 2 (NLOS sector), the received power drops below -85 dBm (which corresponds to the noise floor level of VNA) after a distance of 50 cm. Conversely, in case 4 (NLOS sector), the received power falls below -85 dBm after a distance of 60 cm, thus demonstrating the consistency between the simulation environment and the measurement environment.

TABLE 6.2: Trends of simulated and measured data in case 2 measured in the previous chapter

Sector	Mean	Standard deviation	Variance
<u>Sector 1</u>			
Measured	62	6.519	42.5
Simulated	63.9	6.55	42.94
<u>Sector 2</u>			
Measured	78.22	6.9	47.69
Simulated	74.85	6.29	44.32
<u>Sector 3</u>			
Measured	69.35	6.28	39.49
Simulated	68.67	5.827	34.9

These simulations were conducted with the same settings outlined in Section 5.2, including the operating frequency, transmit power, receiver sensitivity (noise floor level), antenna gain, and the lognormal path loss model. For each graph in Fig.6.2, the values of the path loss exponent and shadowing factor were set according to Tables 5.4 and 5.6. The results demonstrate a similar trend between the simulated and received power data as shown in table 6.2 and 6.3.

To achieve a comprehensive understanding of the on-body radio channel, over 200 simulations were conducted, encompassing a wide range of statistical variations. this is due to several factors such as shadowing, multipath fading, environmental changes, and measurement errors: To address these statistical variations, multiple measurements are taken at corresponding locations and times to obtain a representative sample. These simulations were designed to incorporate the measured on-body radio channel parameters discussed in Section 5.3.

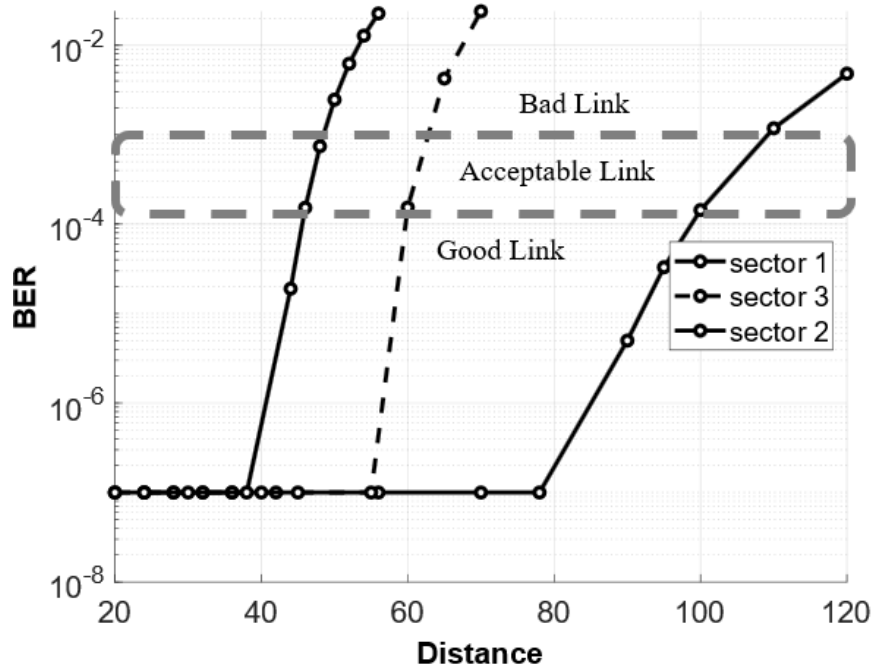


FIGURE 6.3: BER variations with the distance with reference to case 2 (section 5.3.2 explains all three sectors)

Fig.6.3 depicts the variation of Bit Error Rate (BER) for case 2 in relation to the distance of the on-body channel, as outlined in Section (5.3.1). Case 2 was selected due to the presence of a high gain transmitter antenna type and its improved link range capabilities. Based on a predefined maximum acceptable BER threshold derived in [22] from BER curves with respect to E_b/N_0 , the results illustrate the BER of on-body locations (distances from the sink) where the radio link can be classified as either good (BER less than 0.01%), acceptable (BER between 0.1% and 0.01%), or poor (BER higher than 0.1%).

The chest region of the body is divided into three sectors: line of sight (sector 1), non-line of sight (sector 2), and partial line of sight (sector 3). Fig.6.3 reveals significant variations in BER among these sectors across different distances. The results indicate that the radio link quality remains excellent, with a BER below the defined threshold of 1.0×10^{-3} , up to a distance of 35 cm in all sectors.

The bit error rates, representing poor radio links, are higher in the non-line of sight (NLOS) and partial line of sight (PLOS) sectors compared to the line of sight (LOS). This discrepancy can be attributed to the obstruction caused by the

TABLE 6.3: Trends of simulated and measured data in case 4 measured in the previous chapter

Sector	Mean	Standard deviation	Variance
<u>Sector 1</u>			
Measured	60	6.433	41.5
Simulated	61.9	6.481	41.94
<u>Sector 2</u>			
Measured	78.22	6.89	46.56
Simulated	76.72	6.38	45.13
<u>Sector 3</u>			
Measured	67.73	6.44	38.58
Simulated	66.12	6.04	36.95

body's curvilinear shape and the resulting scattering, leading to a reduction in received power.

Similarly, Fig.6.4, depict the variations in the Bit Error Rate (BER) for case 4, in relation to the distance of the on-body channel. This case is outlined in Section 5.3.4 and it was chosen specifically because it features a wide-beam medium transmitter antenna type, which offers improved link range capabilities. The results provide insights into the BER values for on-body positions, representing the distances from the sink.

The graphs reveal significant variations in the BER among different sectors across various distances, as detailed in Section 5.2. The findings demonstrate that the radio link quality remains consistently excellent, with a BER below the defined threshold of 1.0×10^{-3} , for distances up to 48 cm, and 60 cm in case 2, and case 4, respectively, encompassing all sectors, including non-line of sight (NLOS).

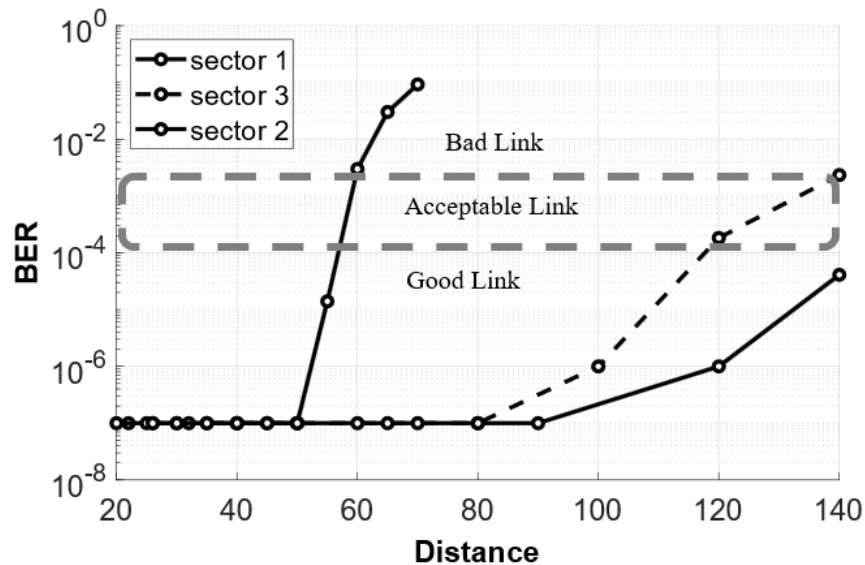


FIGURE 6.4: BER variations with the distance with reference to case 4 (section 5.3.4 explains all three sectors)

Fig.6.3 and 6.4 provide a detailed perspective and offer recommendations for selecting the optimal wireless device location (mainly depending on the sensor type) on the body with respect to distance to achieve acceptable radio link quality and, consequently, ensure good system performance.

6.4 Simulation of Zigbee at 24 GHz: Sink with multiple sensor nodes

The Netsim network simulator has been modified again for multiple sensor nodes to simulate the Zigbee (IEEE 802.15.4) protocol, allowing for an evaluation of the performance of the Carrier Sense Multiple Access (CSMA) mechanisms as a Medium Access Control (MAC) protocol for Wireless Body Area Networks (WBANs). This section aims to explore a network that employs the 24 GHz path loss model and operates under high loads. The analysis involves examining the proportion of the load that successfully transmits over the network, offering valuable insights into the rate of successful data transmission.

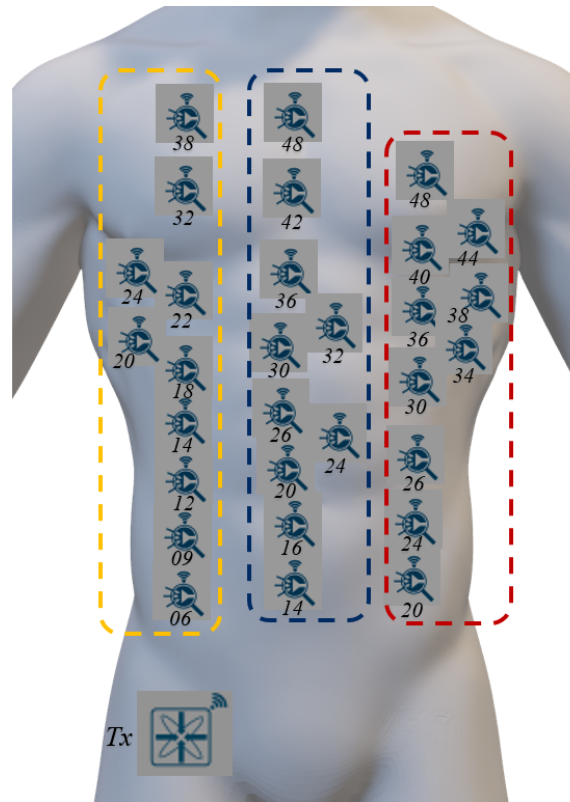


FIGURE 6.5: Sink and sensor nodes' actual location on the chest to torso link

6.4.1 Configuration of NetSim simulator to depict the actual environment

The objective of this simulation is to analyse the performance of the CSMA/CA protocol at 24 GHz in a high path loss environment, specifically when transmitting along and through the human body skin at millimeter-wave frequencies. Replicating the exact on-body channel measurement scenario in simulation poses significant challenges, primarily due to different antenna types in the link between sensor nodes and sink. As explained in section 5.3, there are different sets of channel model parameters based on the transmitter and receiving antennas. Therefore, one set of channel parameters should be used for the link between the sink and sensor nodes, and one set of channel parameters should be used between the sensors.

To address the above-mentioned challenge, the network simulator needs to incorporate two sets of path loss parameters. The first set applies to communication

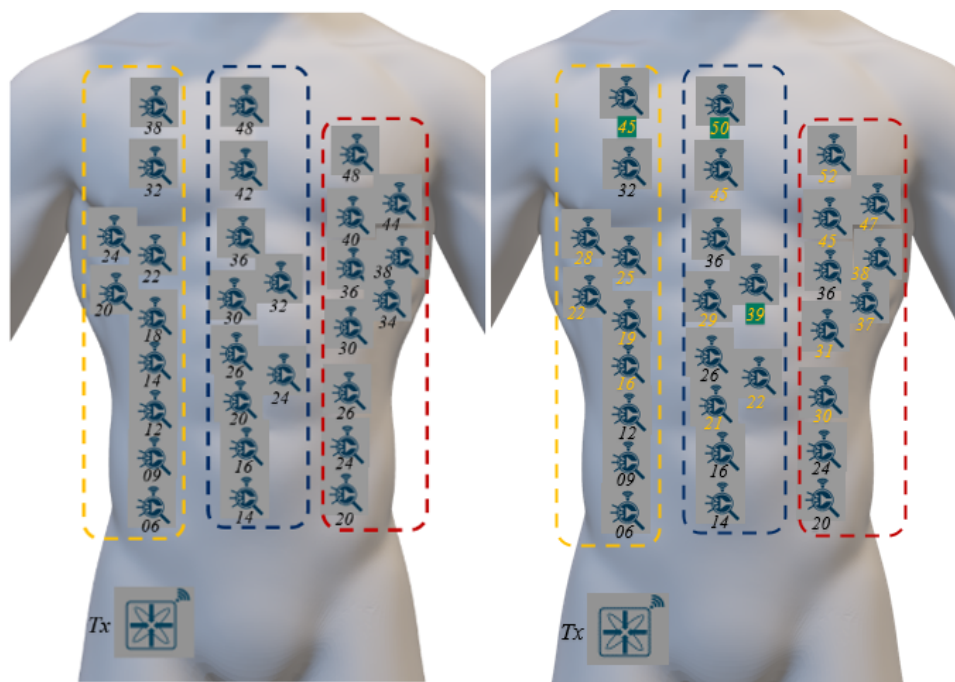


FIGURE 6.6: Sink and sensor nodes location on the chest to torso link in the case 2 environment: Left one is actual locations and right one is simulations locations which are different

links between sensor nodes, as the CSMA/CA protocol requires sensing other nodes before transmitting data on the channel. The second set of parameters is used for communication links between the sink node and sensor nodes. However, the Netsim simulator does not support this functionality. Consequently, with the same set of channel parameters various parameters at the physical layer, such as transmit power, antenna gain, and mainly the distance between the nodes have been adjusted to match the trend between measured and simulated results for each sector.

In Fig.6.5, a depiction of a typical wireless sensor network is presented, situated on the surface of the human body's chest, spanning an area of 36 cm by 50 cm. The network consists of one sink node acting as the Personal Area Network (PAN) coordinator, along with 10 identical nodes in each sector. In Fig.6.5, the distance (in centimeters) from each sensor node to the sink node is indicated beneath the respective nodes. Additionally, the dotted line blocks represent the boundaries of the Line of Sight (LOS), Non-Line of Sight (NLOS), and Partial Line of Sight (PLOS) sectors. In the subsequent sections, the performance of CSMA/CA at

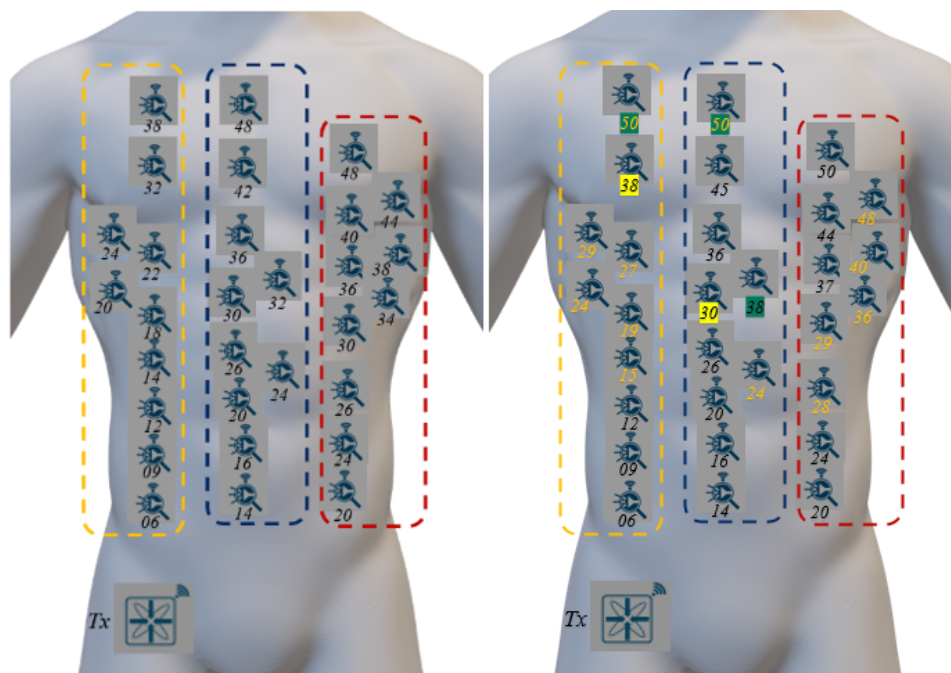


FIGURE 6.7: Sink and sensor nodes location on the chest to torso link in the case 4 environment: Left one is actual locations and right one is simulations locations which are different

24 GHz is investigated for case 2 and case 4. However, prior to that, it is necessary to establish a simulated environment that closely resembles the measured environment for accurate comparison.

In order to establish a consistent environment in the simulation, the distances between nodes were adjusted. This involved positioning nodes at specific distances from each other, ensuring that the received power closely matched the measured data (section 5.3.1). Therefore, in the simulation, the sensor nodes are placed at different locations compared to the actual positions depicted in Fig.6.5. So that the received power level between sensor nodes remains almost identical to measured data (section 5.3.1) when utilising case 2 (section 5.3.2) path loss channel parameters for the communication link between the sink and sensor nodes. Fig.6.5 provides the actual locations (distances from the sink) of the sensor nodes, while Fig.6.6 displays the distances (highlighted in green) set in the simulation to approximate the received power values in comparison to the measured data in the case 2 environment.

Table 6.4 presents the trends of both simulated and measured RSSI data between

the sensor nodes after adjusting their locations. The setup ensures that within each sector simulation, the sensor nodes are positioned in the same sector. Consequently, the communication link between the sensor nodes only requires a same single set of path loss parameters for all three sink-to-sensor sectors scenarios.

TABLE 6.4: Trends of simulated and measured RSSI data between the sensor nodes after adjustments of locations

Sector	Mean	Standard deviation	Variance
<u>Case 2</u>			
Measured	61.425	6.0791	36.5661
Simulated	64.1142	6.8352	41.8628
<u>Case 4</u>			
Measured	60.054	5.8465	34.3712
Simulated	62.9833	6.1092	40.0747

Similarly, also in case 4 consistent environments were established within the simulation, and manual adjustments were made to the distances between sensor nodes to ensure that the received power closely matched the data measured (as shown in table 6.4). The actual locations of the sensor nodes, depicted in Fig.6.5, indicate their distances from the sink. Meanwhile, Fig.6.7 showcases the distances (highlighted in yellow) set in the simulation, which were approximations intended to replicate the actual environment while using only one set of channel model parameters (case 4).

6.4.2 Network simulation under case 2 environment

In this section, we examine the influence of high propagation loss on the performance of CSMA/CA at 24 GHz in an on-body environment. The simulations are conducted with varying channel parameters, including path loss exponent and

shadowing factor, for all three sectors. To assess the impact of different loads on a single channel, we vary the inter-arrival time, while maintaining a constant packet size. The packet size is kept constant at 50 bytes, deliberately chosen to be below the maximum data size of 120 bytes. This decision is crucial because randomizing the data size could result in the generation of multiple packets simultaneously, leading to difficulties in accurately setting and calculating the load. Fig.6.7,6.8, and 6.9 present the normalized throughput against the applied load at 24 GHz taking into account the sector 1, 2, and 3 path loss parameters, as well as at 2.4 GHz. In the proposed environment, 3, 5, and 10 sensor nodes were utilised, while for 2.4 GHz, 10, 25, and 45 sensor nodes were simulated for comparison purposes. More nodes at 2.4 GHz are used for benchmarking and to gain a better understanding of the theoretical curve of normalized throughput against offered load. These plots are grayed out in Fig.6.8 - 6.13.

The results indicate that when the channel has a light load, and the throughput increases with the offered load. However, when the input traffic exceeds its maximum value, the throughput starts to decline within a moderate load range. On the other hand, if the channel is heavily loaded, the throughput remains constant regardless of the traffic rate. This congestion region represents the load range where the throughput does not increase as the offered load grows. The maximum channel throughput occurs at a "knee" point, where the offered load is a little more than the half of channel bit rate (120 kb/s) and the collision rate is between 5 to 10 %. Beyond this point, as the offered load continues to increase, the throughput decreases due to frequent collisions caused by multiple nodes having messages to send in the average packet cycle.

The decrease in throughput is influenced by the number of nodes present in the network. As the number of nodes increases, the occurrence of collisions also increases, as observed in scenarios with 10, 25, and 45 nodes (2.4 GHz) and similar at 24 GHz. Interestingly, in the non-line-of-sight (NLOS) scenario (Sector 2) at 24 GHz, the decrease in the throughput curve is significantly higher compared to the curve at 2.4 GHz. This higher decrease in throughput can be attributed to the high path loss, which further increases collisions and reduces the throughput as

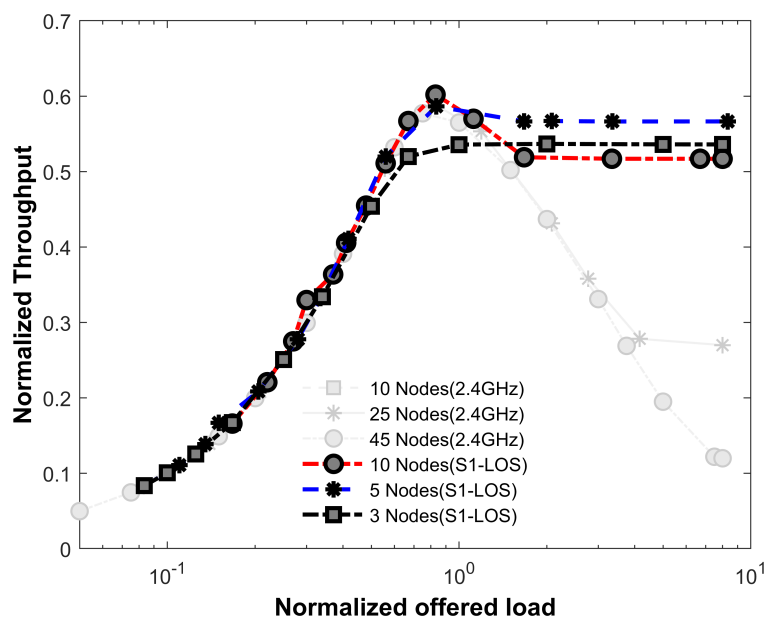


FIGURE 6.8: Normalized throughput against the normalized offered load in case 2 environment of sector 1

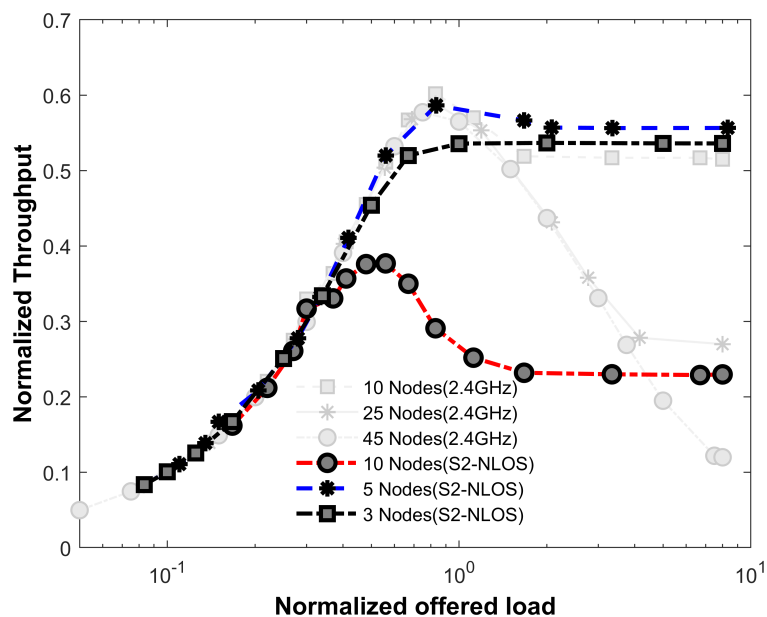


FIGURE 6.9: Normalized throughput against the normalized offered load in case 2 environment of sector 2

the applied load increases. This is due to several reasons such as very weak signal strength, increased hidden terminal issues (two or more nodes are out of range of each other but within the range of a common receiver), and longer propagation delays.

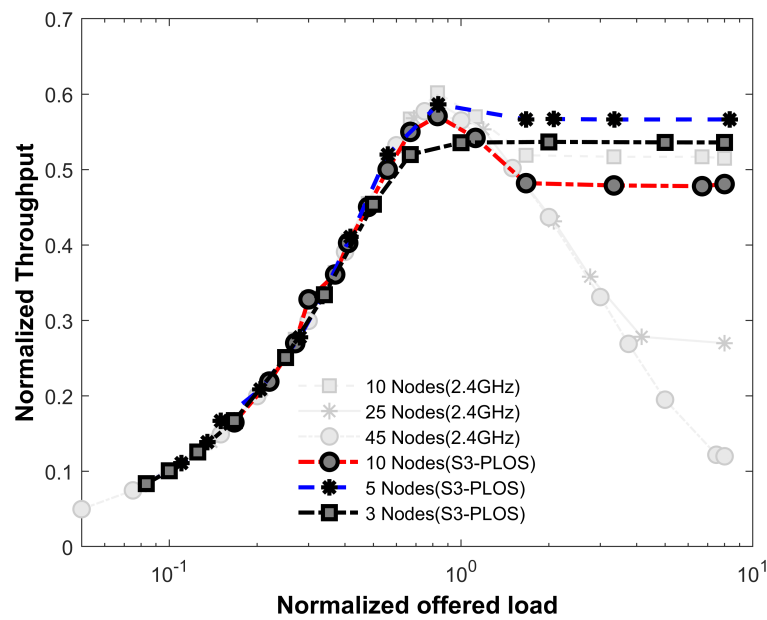


FIGURE 6.10: Normalized throughput against the normalized offered load in case 2 environment of sector 3

When the Zigbee network experiences a higher load, multiple nodes compete for transmission opportunities, resulting in increased congestion within the channel. In the presence of high path loss, nodes may encounter difficulties in reliably receiving transmitted data, leading to retransmissions and further exacerbating contention. Consequently, as the applied load increases, this heightened contention significantly decreases the overall network throughput.

Additionally, it is crucial to consider the impact of higher transmission overhead. In scenarios characterised by high path loss, the elevated error rate and packet loss necessitate additional transmission overhead. The Zigbee protocol incorporates mechanisms for error detection, retransmission, and acknowledgment, which consume additional time and resources. As the network load increases, the overhead associated with these mechanisms becomes more pronounced. This increased overhead reduces the available bandwidth dedicated to actual data transmission, ultimately diminishing the network throughput.

Notice that in the scenario of LOS and PLOS (sector 1 and sector 3), the peak and saturated throughput for 3 nodes is lower than that for 5 nodes (Fig.6.7 to 6.9). This may seem unusual. In a contention network, the throughput increases

with more nodes. However, due to higher backoff time, in the case of 3 nodes, each node goes through a backoff after every transmission. This backoff is wasteful and ultimately reduces the throughput compared to a situation where the nodes are aware that there are only 3 nodes in the network and can send packets back-to-back.

Finally, the network achieves saturation when the output queues of all nodes become full, indicating a state of heavy and steady load [13]. At this stage, the throughput reaches its minimum, and the collision rate reaches its maximum. Beyond saturation, the ratio of throughput to collision rate remains constant, but the packet queues in nodes continue to grow longer. As anticipated, a greater number of transmitting nodes increases the likelihood of collisions, consequently reducing the realized throughput.

The results indicate that with an 80% to 90% probability of successful packet transmission within the acceptable link range distance (as depicted in Fig. 6.3 and detailed in Equations 5.5-5.7), the network can effectively handle an average load of 72 kbps, 69 kbps, and 44.4 kbps, respectively, for sector 1 (LOS), sector 3 (PLOS), and sector 2 (NLOS). These calculations consider the presence of 10 sensors within the network sharing the channel as per the specified configuration setup.

6.4.3 Network simulation under case 4 environment

we analyse the impact of high propagation loss on the performance of CSMA/CA operating at 24 GHz in an on-body environment. The simulations were conducted with various channel parameters, including path loss exponent and shadowing factor, across all three sectors. To assess the impact of different loads on a single channel, we vary the inter-arrival time, while maintaining a constant packet size. Fig.6.11, 6.12, and 6.13 present the normalized throughput against the applied load at 24 GHz and 2.4 GHz in a similar manner as mentioned in the previous section.

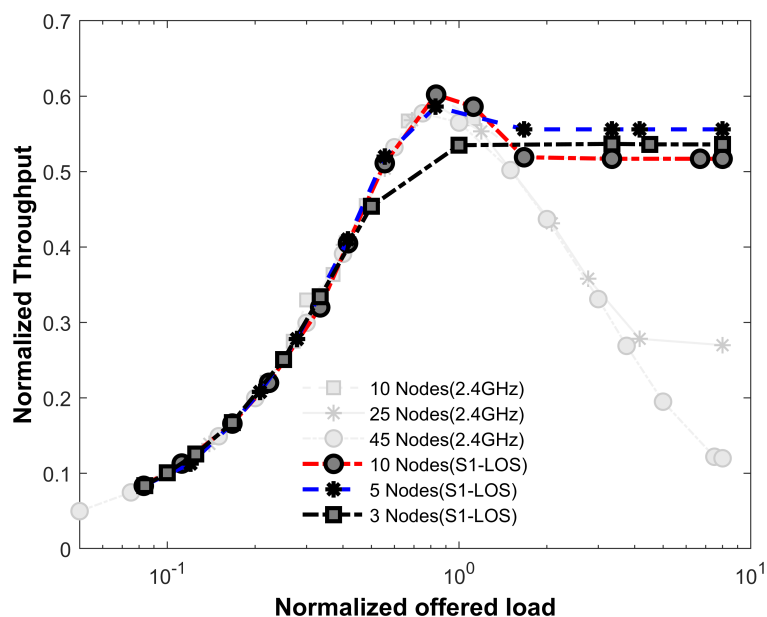


FIGURE 6.11: Normalized throughput against the normalized offered load in case 4 environment of sector 1

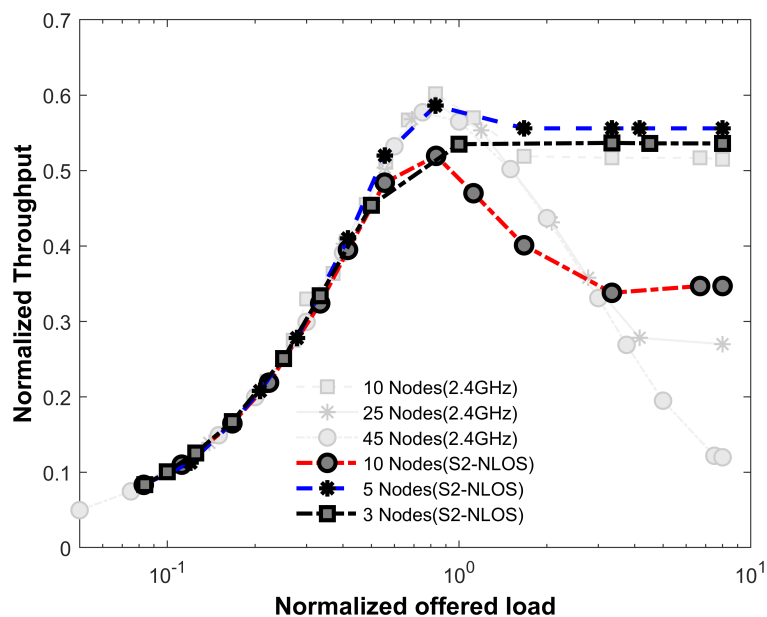


FIGURE 6.12: Normalized throughput against the normalized offered load in case 4 environment of sector 2

The results show similar behavior to the preceding section. At light load, the throughput increases with the offered load. However, in heavily loaded channels, the throughput remains constant, forming a congestion region. The maximum throughput occurs when the offered load matches the channel bit rate. Beyond

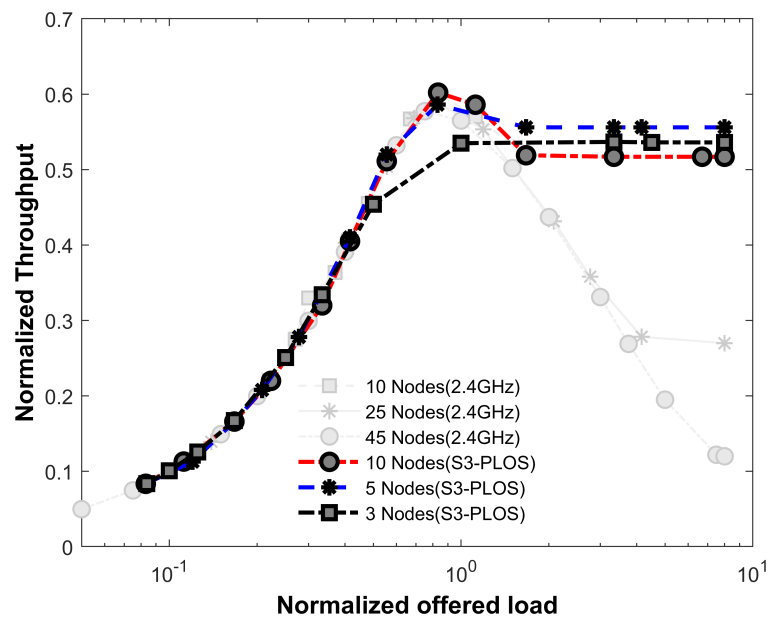


FIGURE 6.13: Normalized throughput against the normalized offered load in case 4 environment of sector 3

this point, increasing the offered load results in decreased throughput due to frequent collisions caused by multiple nodes. The number of nodes and high path loss in the NLOS scenario further amplify collisions and reduce throughput as the load increases. However, in the case 4 environment and non-line-of-sight (NLOS) scenario at 24 GHz (Sector 2), the decrease in the throughput curve is less compared to the previous scenario (case 2). This is because the lower path loss makes it easier for nodes to sense or detect other nodes while transmitting packets, resulting in reduced contention.

Similar to case 2, in case 4, which involves Line-of-Sight (LOS) and Partial Line-of-Sight (PLOS) scenarios, the throughput for configurations with 3 nodes is lower compared to configurations with 5 nodes. This discrepancy arises due to the higher backoff time in the 3-node configurations, resulting in wasteful backoffs and reduced throughput. As the network reaches saturation, characterised by full queues and a heavy load, the throughput is minimized while collisions are maximized. Once saturation is surpassed, the probability of collisions increases with a larger number of transmitting nodes, leading to a decrease in the realized throughput.

The investigation demonstrates that the network achieves a high probability (around 80% to 90%) of successfully transmitting packets within the acceptable link range distance, as illustrated in Fig. 6.4 and outlined in Equations 5.11-5.13. Based on these results, the network proves capable of efficiently handling an average load of 72 kbps, 72 kbps, and 62.4 kbps for sector 1 (LOS), sector 3 (PLOS), and sector 2 (NLOS), respectively. These load calculations consider a network configuration comprising 10 sensors sharing the channel.

The results demonstrate that for sensor nodes to exhibit Line-of-Sight (LOS) behavior and to simulate the 1 set of path loss channel models, it is essential that they are located within the same sector. Specifically, in the Non-Line-of-Sight (NLOS) sector, it is crucial for the sensor nodes to be in close proximity to each other in order to sense each other effectively amidst the high path loss encountered in sector 2. Otherwise, the positioning of the nodes may lead to increased hidden terminal issues, wherein two or more nodes are out of range of each other but within the range of a common receiver. This highlights the significant impact of sensor node positioning on the network's throughput performance.

6.5 Conclusion

This chapter has examined the performance of the Zigbee protocol (physical layer and MAC) in the context of the 24 GHz channel model discussed earlier. A typical star topology was used, incorporating basic physiological sensors and allocating them to suitable channels within the 24 GHz ISM band based on their individual requirements. In this chapter, the analysis of Zigbee (PHY and MAC) primarily emphasizes the FDMA with CSMA/CA aspects of the protocol, considering the utilisation of multiple channels for sensors like ECG or EEG (using FDMA) and the channel sharing behavior of sensors like inertial measurement units and temperature sensors (employing CSMA/CA).

Initially, the analysis primarily focused on the physical layer performance of physiological sensor nodes operating on channels without interference from other nodes,

as outlined in Table 6.1. Subsequently, the performance of the single-node radio link connected to the sink was evaluated by assessing the bit error rate (BER). The results indicated consistently excellent radio link quality, with a BER below the defined threshold of 1.0×10^{-3} , for distances up to 48 cm, and 60 cm in Case 2, and Case 4, respectively, at non-line of sight (NLOS) sector. It was observed that the system outage percentage, representing poor radio links, was higher in the NLOS and partial line of sight (PLOS) sectors compared to the line of sight (LOS), likely due to body obstruction and resulting scattering, leading to reduced received power.

Furthermore, the analysis examined the MAC protocol, specifically the Carrier Sense Multiple Access (CSMA), in the context of the communication link between the sink and multiple sensor nodes. The investigation primarily focused on evaluating the throughput performance under varying applied loads, taking into consideration the 24 GHz on-body channel model. In the LOS (Sector 1) scenario, the throughput performance at 24 GHz exhibited similarity to that of the 2.4 GHz frequency. In the case of PLOS (Sector 3), a slight decline in throughput was observed compared to 2.4 GHz. However, in the NLOS scenario, the throughput performance showed a drastic decrease with increasing applied load.

In general, the protocol's performance exhibits a peak in throughput initially, followed by a subsequent decrease and eventual saturation. However, when the network operates under high loads, only a minimal proportion of the load is effectively transmitted over the network. This proportion can be determined by dividing the throughput by the load, providing insight into the successful transmission rate. Consequently, it is not advisable or suitable to utilise the network within this region of low throughput-to-load ratio. While sudden spikes in load may be accommodated to some extent, it is not recommended for the average network behavior. Ideally, the average load in this region should be noticeably lower than the levels currently observed. In the current network setup, a 44.4 and 62.4 kbps average load is considered acceptable for sector 2 (NLOS) in case 2 and case 4 scenarios, respectively. While sectors 1 and 3 can tolerate an average load

of 72 kbps. This load level is deemed reasonable for scenarios involving 5 and 10 sensors that need to share the channel in the given application context.

The results obtained underscore the significant impact of sensor positioning on the body, particularly in relation to the sector in which they are situated, on the performance of the MAC protocol (CSMA). This emphasizes the critical importance of considering these parameters when designing the MAC layer protocol for body-centric wireless communications. By taking into account sensor positioning, it becomes possible to minimize collisions, reduce packet loss, and achieve optimal performance in such networks.

References

- [1] Lai X, Liu Q, Wei X, Wang W, Zhou G, Han G. "A survey of body sensor networks." *Sensors* 13(5):5406–5447, 2013.
- [2] Yang, X., Matthaiou, M., Yang, J., Wen, C. K., Gao, F., Jin, S. "Hardware-constrained millimeter-wave systems for 5G: Challenges, opportunities, and solutions." *IEEE Communications Magazine*, 57(1), 44-50, 2019.
- [3] Larew, S. G., Thomas, T. A., Cudak, M., Ghosh, A. "Air interface design and ray tracing study for 5G millimeter wave communications." In *IEEE Globecom Workshops (GC Wkshps)*, 2013, pp. 117-122.
- [4] Li, Y., Luo, J., Castaneda, M. H., Vucic, N., Xu, W., Caire, G. "Analysis of Broadcast Signaling for Millimeter Wave Cell Discovery." *IEEE 86th Vehicular Technology Conference (VTC-Fall)*, 2017.
- [5] T. S. Rappaport et al., "Millimeter Wave Wireless Communications," Pearson Education, 2014.
- [6] Ullah S, Shen B, Riazul Islam SM, Khan P, Saleem S, Kwak KS "A study of MAC protocols for WBANs." *Sensors* 10:128–145, 2010.
- [7] Ullah S, Mohaisen M, Alnuem MA, "A review of IEEE 802.15.6 MAC, PHY, and security specifications." *Int J Distrib Sens Netw* 2013:1–12, 2013.
- [8] Gopalan, S. A., Park, J. T. "Energy-efficient MAC protocols for wireless body area networks: Survey." In *International Congress on Ultra Modern Telecommunications and Control Systems*, October 2010, pp. 739-744.

-
- [9] Busch, C., Magdon-Ismaïl, M., Sivrikaya, F., Yener, B. "Contention-free MAC protocols for wireless sensor networks." In *International Symposium on Distributed Computing* (pp. 245-259). Springer, Berlin, Heidelberg, October 2004.
- [10] Gu, L., Stankovic, J. A. "Radio-Triggered Wake-Up Capability for Sensor Networks." In *IEEE Real-Time and Embedded Technology and Applications Symposium*, May 2004, pp. 27-37.
- [11] Kazemi, R.; Vesilo, R.; Dutkiewicz, E.; Fang, G. "Inter-network interference mitigation in Wireless Body Area Networks using power control games." In *Proceedings of the 10th International Symposium on Communications and Information Technologies*, Tokyo, Japan, 26–29 October 2010; pp. 81–86.
- [12] Arbia, D. B., Alam, M. M., Moullec, Y. L., Hamida, E. B. "Communication challenges in on-body and body-to-body wearable wireless networks—a connectivity perspective." *Technologies*, 5(3), 43, 2017.
- [13] Ullah, F., Abdullah, A. H., Kaiwartya, O., Kumar, S., Arshad, M. M. "Medium access control (MAC) for wireless body area network (WBAN): superframe structure, multiple access technique, taxonomy, and challenges." *Human-centric Computing and Information Sciences*, 7, 1-39, 2017.
- [14] Ehyaié A, Hashemi M, Khadivi P. "Using relay network to increase the lifetime in wireless body area sensor networks. World of Wireless, Mobile and Multimedia Networks Workshops," *IEEE International Symposium on a.* 2009:1–6.
- [15] Elias J. "Optimal design of energy-efficient and cost-effective Wireless Body Area Networks." *Ad Hoc Networks*, 3 Part B, pp 560-74, 2014.
- [16] Reusens E, Joseph W, Latre B, Braem B, Vermeeren G, Tanghe E, et al. "Characterization of on-body communication channel and energy efficient topology design for wireless body area networks." *IEEE Trans Inf Technol Biomed.*, 13:933–45, 2009.

-
- [17] Yaghoubi, M., Ahmed, K., Miao, Y. "Wireless body area network (WBAN): "A survey on architecture, technologies, energy consumption, and security challenges." *Journal of Sensor and Actuator Networks*, 11(4), 67, 2022.
- [18] Zhang Q, Kortermant K, Jacobsen RH, Toftegaard TS. "Reactive virtual coordinate routing protocol for body sensor networks." *IEEE International Conference on Communications (ICC)* 2012:3388–93.
- [19] J. Kim et al., "Joint Scalable Coding and Routing for 60 GHz Real-Time Live HD Video Streaming Applications," *IEEE Trans. Broadcast.*, vol. 59, no. 3, pp. 500–12, Sept. 2013.
- [20] S. Singh et al., "Blockage and Directivity in 60 GHz Wireless Personal Area Networks: From Cross-Layer Model to Multihop MAC Design," *IEEE JSAC*, vol. 27, no. 8, pp. 1400–13, Oct. 2009.
- [21] H. Shokri-Ghadikolaei et al., "Millimeter Wave Cellular Networks: A MAC Layer Perspective," *IEEE Trans. Commun.*, vol. 63, no. 10, pp. 3437–58, Oct. 2015.
- [22] Abbasi, Q. H., Sani, A., Alomainy, A., Hao, Y. "On-body radio channel characterization and system-level modelling for multiband OFDM ultra-wideband body-centric wireless network." *IEEE Transactions on Microwave Theory and Techniques*, 58(12), 3485-3492, 2010.
- [23] Miskowicz, M., Golanski, R. "LON technology in wireless sensor networking applications. *Sensors*, 6(1), 30-48, 2006.

Chapter 7

Conclusion and Future work

The development of wireless body area network technologies has been ongoing for the past ten years with the aim of establishing reliable and efficient body-centric wireless communication. However, due to the unique properties of the human body as the primary environment for wireless communication, it remains extremely challenging to understand the characteristics of wireless body channels and design compact, highly efficient antennas for wearable electronic devices.

Several issues remain unresolved in wireless communication systems for BANs. Privacy and security are considered crucial for wireless body area networks. The prevalence of wireless devices operating at 2.4 GHz ISM narrow bands poses a significant risk of interference. Furthermore, preventing interference between nearby BANs is challenging due to the mobility and uncoordinated operation characteristics of BANs. In certain unique applications, such as military use, highly secure and covert wireless communications are necessary, but the current solutions provided by standards like Bluetooth and UWB are not particularly effective. Moreover, constructing small and highly efficient antennas for body-worn devices at these frequencies is extremely difficult. Additionally, as more advanced cellular communication networks are developed, there is an increasing demand for high-speed communications.

This thesis proposes an alternative wireless option for body area networks, utilising the 24 GHz radio frequency. By operating at 24 GHz, this approach enables effective control of electromagnetic energy, minimizing interference with other devices and reducing vulnerability to jamming and observation. Furthermore, operating at this frequency allows for the use of smaller and more efficient antennas, which is particularly important for body-worn applications. Moreover, the availability of a large unlicensed frequency band at 24 GHz enables the achievement of high data speeds, offering substantial bandwidth for transmission.

this study has made significant contributions to the field of wireless communication in the 24 GHz ISM band for body-centric applications. The research has provided valuable insights into antenna design, 24 GHz on-body channel characterisation, path loss modeling, and performance evaluation of the Zigbee (PHY and MAC layer) protocol.

The antenna designs presented in this study demonstrated novel and innovative approaches to address the unique challenges of on-body communication at 24 GHz ISM band. The low-profile thin-layered split square-ring EBG structure and radial stub antennas exhibited improved gain, front-to-back ratio, and insensitivity to body proximity. The Koch fractal antennas with EBG structures showcased stability, ultra-thin, reduced size, and enhanced bandwidth. The proposed antennas offer several key features that render them suitable for on-skin mounting in 24 GHz Wireless Body Area Network (WBAN) applications. Firstly, both the 1st and 2nd iteration fractal structures demonstrate a broad bandwidth of 11.25% and 13.3%, respectively, when directly attached to the skin. Moreover, In comparison with existing K band EBG backed antennas (as illustrated in table 4.2), these antennas exhibit minimal shift in S_{11} during bending, showcasing their robustness to deformation while maintaining excellent performance. Additionally, they exhibit a significant increase in front-to-back ratio (FBR), indicating improved signal transmission and reception away from the body. Furthermore, the proposed EBG-backed Koch fractal geometry-based antennas reduce Specific Absorption Rate (SAR) by 90% and 87% when compared to direct antenna exposure, ensuring their safe usage in close proximity to the human body. These proposed antennas

are the thinnest ($0.02\lambda_0$) EBG-backed antennas reported in the K band. The Yagi Uda and Vivaldi antennas demonstrated directional radiation patterns suitable for on-body communication scenarios. These antenna designs offer promising solutions for improving wireless communication performance in wearable devices and body area networks.

The on-body channel characterisation and path loss modelling studies highlighted the influence of antenna placement and the contoured shape of the human body on signal propagation. These findings emphasized the importance of carefully selecting appropriate antennas and considering the impact of body morphology when designing communication systems for on-body applications. By understanding the propagation characteristics and path loss effects, researchers and engineers can develop more accurate models and optimise system performance.

The performance evaluation of the Zigbee protocol in the 24 GHz ISM band provided valuable insights into its suitability for body-centric wireless communication. The analysis revealed the trade-off between throughput and applied load under the very high path loss, indicating that high loads significantly reduce the successful transmission rate. It was recommended to maintain the average load well below the saturation point, with a tolerable average load of 40% for sector 2 (NLOS) and 53.89% for sectors 1 and 3. Moreover, the positioning of sensor nodes and consideration of channel-sharing behavior were identified as critical factors for achieving optimal performance in the Zigbee network.

This thesis introduces the technical aspects of utilising the 24 GHz ISM band radio for wireless body area networks. The on-body channels at 24 GHz ISM band have been thoroughly analysed using four different types of antennas. Through a comprehensive evaluation, the Zigbee (PHY and MAC) protocol's performance in the 24 GHz ISM band has been examined, providing valuable insights into its suitability for body-centric wireless communication. To aid in the understanding, a summary of a comparison between three extensively researched frequency bands for wireless body area networks is presented in Table 7.1.

TABLE 7.1: WBAN comparison at different frequencies

Frequency band	2.45GHz (ISM-band)	UWB(3.1-10.6GHz)	24GHz (ISM-band) this work
Available Spectrum	Congested	Congested	Under-utilised
Data rates	Mbps	Gbps	Gbps
Interference	High	narrowband systems experience less interference	Due to High path loss, Reduced interference
Radiation control	Very limited	limited	Good (Directional Antennas and small antenna arrays)
Frequency Reuse	Low	Low	High
Form Factor	Bulky	Bulky	Small
Antenna Efficiency	Low	Low	High

In summary, this study has contributed to advancing the field of wireless communication in the 24 GHz ISM band for body-centric applications. The proposed antenna designs, on-body channel characterisation, path loss models, and evaluation of the Zigbee protocol provide valuable insights for the design and implementation of wireless body area networks. Further research can explore additional antenna designs, refine path loss models, and investigate enhancements to the Zigbee protocol to address the specific challenges and requirements of body-centric wireless communication. By continuing to advance these areas of study, we can unlock the full potential of wireless communication technologies for wearable devices, health-care applications, and other body-centric communication systems.

7.1 Future work

The findings of this study present several promising directions for future research and development. The following areas offer potential opportunities for further exploration:

Advancements in 24 GHz wearable Antenna Designs: Future work can focus on the exploration and development of textile-based antennas for on-body communication. Additional research can be conducted to explore reconfigurable antennas for 24 GHz ISM band WBAN with the goal of achieving improved radiation control. This can involve designing reconfigurable antennas that cater to various channels and scenarios, employing different beamforming techniques for enhanced performance.

24 GHz On-body Propagation Modeling for different postures and movements: There is a need for additional research to enhance and broaden the current 24 GHz path loss models used in on-body communication. This research should encompass the examination of how various body types, postures, and movements affect signal propagation, with the aim of developing more precise and reliable propagation models.

Channel Characterisation in realistic environments: Future work should aim to delve deeper into on-body channel characterisation by incorporating additional factors such as multi-path propagation, polarisation effects, and interference from external sources. By considering these factors, a more comprehensive understanding of the communication channel in body-centric scenarios can be achieved, enabling the development of efficient communication techniques and algorithms.

FDMA-based CSMA/CA Protocol Enhancements: There is scope for further optimisation of the MAC (FDMA-based CSMA/CA) protocol in body-centric wireless communication. Subsequent research efforts should focus on developing adaptive and energy-efficient protocols that consider the unique challenges and requirements of on-body networks. This can involve incorporating mechanisms

for multi-hop networks, dynamic channel allocation, interference mitigation, and effective resource management.

Real-world Deployment and Validation: Conducting extensive field trials and real-world deployments of 24 GHz on-body communication systems is essential to gaining valuable insights into their performance, reliability, and usability.

By addressing these future research directions, we can advance the field of body-centric wireless communication at the 24 GHz ISM band and enable innovative applications that enhance human health, well-being, and overall quality of life.